ISSN: 0973-6255
Vol. 4 No. 2
July - December 2010

Indian Journal of Engineering, Science, and Technology

A Refereed Research Journal









BANNARI AMMAN INSTITUTE OF TECHNOLOGY
Stay Ahead

BANNARI AMMAN INSTITUTE OF TECHNOLOGY
(Autonomous Institution Affiliated to Anna University of Technology, Coimbatore -
Approved by AICTE - Accredited by NBA and NAAC with "A" Grade)
Sathyamangalam - 638 401 Erode District Tamil Nadu India

Indian Journal of Engineering, Science, and Technology

IJEST is a refereed research journal published half-yearly by Bannari Amman Institute of Technology. Responsibility for the contents rests upon the authors and not upon the IJEST. For copying or reprint permission, write to Copyright Department, IJEST, Bannari Amman Institute of Technology, Sathyamanagalam, Erode District - 638 401, Tamil Nadu, India.

Indian Journal of Engineering, Science, and Technology

ISSN: 0973-6255

Volume 4 Number 2 July - December 2010

CONTENTS

Precision Point Synthesis of Single Spring-Actuated Lever for Position-Energy Co-ordination

A.D. Telang[1] and K. Kurien Issac[2]
[1]College of Engineering, Farmagudi, Goa - 403 401
[2]Indian Institute of Technology, Bombay, Mumbai - 400 076
Email: arundtelang@yahoo.co.in
(Received on 03 October 2008 and accepted on 10 August 2010)

Abstract

Synthesis procedure has been developed to synthesise spring actuated lever, to coordinate, specified changes in spring energy with the given displacement of the lever. Synthesis procedure is non-iterative up to three displacements and needs iterations in one dimension for four displacements.

Keywords: *Displacement, Energy, Stiffness, Non-dimensional, Position, Spring-actuated*

Notations:

a	= Distance at which spring is attached to the ground, meter
b	= Distance at which spring is attached to the lever, meter
E	$=1/2\,k(a^2+b^2)$, Nm
k	= Stiffness of the spring, N/m
p	$=2ab/(a^2+b^2)$
q_i	= +1(spring in tension), -1(spring in compression)
S	= Free length of spring, meter
s	= Non-dimensional length of a spring $S/\sqrt{(a^2+b^2)}$
V_i	= Energy of the spring in the 'i'th position, Nm
ΔV_i	= Change of energy from reference position`0' to `i'th position, Nm
v_i	= Non-dimensional energy V_i/E
W_i	$=\sqrt{V_i}$
w_i	$=\sqrt{v_i}$
θ_i	= Angle between 'x' axis and the lever in 'i'th position
$\Delta\theta_{i0}$	= 'i'th position of the lever relative to the reference position '0'

1. INTRODUCTION

Task of synthesizing a system to generate required motion is of immense importance to Design Engineers. Usually electric motors with sophisticated controls are used to obtain the desired motion. However, when the desired motion is complex, spring actuated mechanisms, having natural motion close to the desired motion; offer an alternative, in which a motor with low torque capability can be used. These spring-actuated mechanisms can be synthesized using energy method. With this in mind the problem of synthesizing spring actuated lever, shown in fig.1, has been taken up here, so as to get specified changes in spring energy for the specified rotation of the lever.

Hain[1][2] carried out force analysis of a spring-lever mechanism [1], and proposed a graphical synthesis procedure, to balance load moment for up to four positions[2]. A non-circular pulley, with a flexible band and a spring was used [3] to obtain continuous moment balance on a lever. Genova [4], has synthesised the mechanism, being dealt with in this paper, to replace/ supplement flywheel in machinery to minimize the coefficient of fluctuation of speed by balancing moment. The net moment (summation of driving moment, load moment and inertia moment) is balanced to an adequate degree of approximation by synthesising design parameters by grapho-analytical method, which uses the catalog containing functions of spring moments for the various values of design parameters. From a survey of related literature, it appears that the problem of achieving specified energy changes for specified displacements has not been fully addressed for the single linear spring – single lever system. This problem is taken up here to propose procedures for up to four displacements - energy change pairs, the maximum possible with this system.

2. PROBLEM DEFINITION AND ENERGY EQUATION

The system shown in figure 1 consists of a lever pivoted to the ground at 'A'. A linear spring of free length 'S' and stiffness 'k' is attached to the lever at 'B' and to the ground at 'C'. The problem is to determine the parameters 'S', 'k', a(=AC) and b(=AB) such that given spring energy changes ΔV_{i0}, i=1,2,3,...m are obtained for given lever rotations $\Delta\theta_{i0}$,i=1,2,3,....m. 'm' is the number of precision points. Here is the energy change from the reference position 0 to i[th] position. In addition to the parameters mentioned above, the reference position, 'θ_0'is also a parameter to be determined. Energy, V_1 of the spring, when lever makes an angle θ_1 with the reference axis, as shown in figure 1, is give

$$V_i = \tfrac{1}{2}k\left(\sqrt{a+b-2ab\cos\theta_i} - S\right)^2 \qquad (1)$$

where,
a=distance at which spring is attached to the ground.
b=distance at which spring is attached to the lever.
k=stiffness of the spring
S=Free length of the spring
The above equation can be written as

$$V_i = E\left(\sqrt{1-p\cos\theta_i} - s\right)^2 \qquad (2)$$

where, $$E = \frac{1}{2}k\left(a^2+b^2\right)$$

$$p = \frac{2ab}{\sqrt{a^2+b^2}}$$

$$s = \frac{S}{\sqrt{a^2+b^2}}$$

The synthesis problem, for given spring energy changes and the specified lever displacements, is basically, to get the solution of the following system of non-linear equations, such that

E > 0(energy can not be negative),
s > 0 (free length can not be negative),\\
and -1 ≤ p ≤ 1. (Distances a and b have to be real.)

$$\Delta V_{i0} = V_i - V_0 \qquad i=1,2,\ldots m \qquad (3)$$

where,

$$V_i = E\left(\sqrt{1-p\cos(\theta_0+\Delta\theta_{i0})} - s\right)^2$$

and

$$V_0 = E\left(\sqrt{1-p\cos\theta_0} - s\right)^2$$

ΔV_{i0} =Spring energy differences as the lever moves from reference position '0' to 'i'.

$\Delta\theta_{i0}$ =Displacement of lever from position '0' to 'i'.

In the Equations (3) above, the unknown parameters are E, p, s and θ_0. Thus it is possible that the system can be synthesized, at the most, up to four specified energy differences, provided the solution of the equation lie within the region given by the bounds on the parameters.

Equation (2) is obtained in the non-dimensional form by dividing it by 'E',

$$v_i = \left(\sqrt{1-p\cos\theta_i} - s\right)^2 \qquad (4)$$

where, $v_i = \dfrac{V_i}{E}$. Taking square root of the Equation (4)

$$q_i w_i = \sqrt{1-p\cos\theta_i} - s \qquad (5)$$

Here, w_i is the positive square root of v_i. The variable q_i is introduced to indicate whether the spring is in tension or compression. If q_i is -1, the spring is in compression and if it is +1, the spring is in tension. Choice of q_i is made by the designer based on the requirements of the problem or in order to make the design feasible.

Transferring 's' to LHS, squaring and rearranging, the following equation is obtained, which can be used for synthesis.

$$s^2 + 2q_i w_i s + v_i + p\cos\theta_i - 1 = 0 \qquad (6)$$

The above equation is equivalent to Equation (4), provided $q_i w_i + s$ is non-negative. This condition is necessary to discard the cases in which $\sqrt{1-p\cos\theta_i}$ contains the square of negative values of ,
which indicates negative spring length, a physical impossibility. An additional parameter can be introduced into Equation (6) by multiplying it by 'E', and thereby reintroducing the dimensions. By this, we obtain another synthesis equation.

$$(s^2-1)E + 2q_i\sqrt{V_i}\sqrt{E}\,s + v_i + pE\cos\theta_i - 1$$
$$= -V_i \qquad (7)$$

Based on Equation (6), the procedures for one and two displacement synthesis are described below, along with numerical examples. A modified form of the Equation (7), with the energy in the dimensional form, is then used for two and three displacement synthesis, and illustrated using numerical examples. The above procedures are non-iterative. For four displacements synthesis, an iterative procedure is proposed and examples given. Finally it is concluded that it will always be possible to synthesize for two arbitrarily specified energy differences and displacements. The same can not be said for three and four displacements.

3. SINGLE DISPLACEMENT SYNTHESIS

Given the lever displacement $\Delta\theta_{i0}$ and the corresponding spring energy change ΔV_{i0}, the task is to synthesise spring-lever parameters. Equation (6) can be used for solving the above problem. First, values of V_0, θ_0 and the scale factor 'E' are chosen, and non-dimensionalised energies v_0 and 'v_1', and lever positions calculated. Then, q_0 and q_1 are chosen and Equation (6) written for the two positions.

$$s^2 + 2q_0 w_0 s + v_0 + p\cos\theta_0 - 1 = 0 \qquad (8)$$

$$s^2 + 2q_1 w_1 s + v_1 + p\cos\theta_1 - 1 = 0 \qquad (9)$$

From Equation (8)

$$p = \frac{1 - s^2 - 2q_0 w_0 s - v_0}{\cos\theta_0} \qquad (10)$$

Substituting for 'p' in Equation (9), quadratic equation in 's' is obtained. For physically realizable solution, 's' should be real and non-negative. Instead of displacement, if the positions θ_0, θ_1, and the corresponding energies are given, the above procedure can still be used for synthesis.

4. TWO DISPLACEMENT SYNTHESIS

Given the lever displacement $\Delta\theta_{10}$ and $\Delta\theta_{20}$ the corresponding spring energy changes $\Delta\theta_{10}$ and $\Delta\theta_{20}$ the task is to synthesise spring-lever parameters and determine the reference position of the lever i.e. θ_0 Two procedures for synthesis, one based on Equation (6) and another based on Equation (7), are described below, along with the examples.

4.1 Synthesis with 'θ_0', the Reference Position, as Unknown

The initial energy V_o, and scale factor E are chosen and w_i determined for use in the synthesis equation.

Values of 'q_i' s are also chosen. Following three equations can be written down for three positions.

$$s^2+2q_0w_0s+v_0+p\cos\theta_0 - 1 = 0 \quad (12)$$
$$s^2+2q_1w_1s+v_1+p\cos\theta_1 - 1 = 0 \quad (13)$$
$$s^2+2q_2w_2s+v_2+p\cos\theta_2 - 1 = 0 \quad (14)$$

Writing $\cos\theta_1 = \cos(\theta_0+\Delta\theta_{10})$ and $\cos\theta_2 = \cos(\theta_0+\Delta\theta_{20})$ and subtracting Equation (12) from Equations (13) and (14), we write,

$$\begin{bmatrix} \cos\theta_{10}-1 & -\sin\Delta\theta_{10} \\ \cos\Delta\theta_{20}-1 & -\sin\Delta\theta_{20} \end{bmatrix} \begin{bmatrix} p\cos\theta_0 \\ p\sin\theta_0 \end{bmatrix} =$$
$$\begin{bmatrix} (v_0-v_1) \\ (v_0-v_2) \end{bmatrix} + \begin{bmatrix} q_0w_0-q_1w_1 \\ q_0w_0-q_2w_2 \end{bmatrix} 2s \quad (15)$$

If the above equation is solvable, following can be written,

$$p\cos\theta_0 = a_1 + a_2s \quad (16)$$
$$p\sin\theta_0 = b_1 + b_2s \quad (17)$$

Where a_1, a_2, b_1, b_2 are obtained by pre-multiplying Equation (15) with the inverse of the LHS system matrix. Substituting for $p\cos\theta_0$ from Equation (16) in Equation (12) and rearranging:

$$s^2+(2q_1w_1 + a_2)\,s + (a_1-1 + v_1) = 0 \quad (18)$$

Real positive solutions for 's' are used to determine 'p' and 'θ_0' using Equations (16) and (17). For particular 'θ_0', sign of 'p' is determined, by checking, for the values of energy levels, in the required positions.

Ex.1: For the lever displacements $\Delta\theta_{10}=45^0$ and $\Delta\theta_{20}=210^0$ the corresponding spring energy changes ΔV_{10} = -2000 and ΔV_{20}= 5000 synthesis was carried out, using the procedure, given above. Parameters V_0=4000, E=10000 and $[q_0 \ q_1 \ q_2]$ = [-1 -1 -1] were assumed. The design was obtained as s=1.6955, p=-0.6721 and θ_0=-78.84^0

Figure 2 shows spring energy variation against the lever position, for the synthesised system. The design points are marked on the graph.

4.2. Synthesis with Scale Factor 'E' as Unknown

In this case, Equation (7) is used for synthesis. The unknowns are E, p and s. The initial energy V_0, and values of q_i's are chosen. Writing Equation (7) for three positions, we get,

$$\begin{bmatrix} 2q_0\sqrt{V_0} & \cos\theta_0 & 1 \\ 2q_1\sqrt{V_1} & \cos\theta_1 & 1 \\ 2q_2\sqrt{V_2} & \cos\theta_2 & 1 \end{bmatrix} \begin{Bmatrix} r_1 \\ r_2 \\ r_3 \end{Bmatrix} = \begin{Bmatrix} -V_0 \\ -V_1 \\ -V_2 \end{Bmatrix} \quad (19)$$

where,

$$r_1 = s\sqrt{E},\ r_2 = pE \ \text{ and } r_3 = (s^2-1)E.$$

If Equation (19) is solvable, r_1, r_2 and r_3 can be determined and from them E, p and s can be obtained as $E=r_1^2 - r_3$, $p=r_2/E$ and $s = r_1/\sqrt{E}$.

Ex. 2: For the lever displacements $\Delta\theta_{10}=45^0$ and $\Delta\theta_{20}=210^0$ the corresponding spring energy changes ΔV_{10} = 2000 and ΔV_{20}= 5000, synthesis was carried out, using the procedure given above. Parameters V_0= 6000, θ_{10}= -60^0 and $[q_0\ q_1\ q_2]$ = [1 1 1] were assumed. The design was obtained as E=10694, p=-0.5955 and s=0.3901.

Figure 3 shows spring energy variation against the lever position, for the synthesised system. The design points are also marked on the graph.

5. THREE DISPLACEMENT SYNTHESIS

Given the lever displacement $\Delta\theta_{10}$, $\Delta\theta_{20}$, $\Delta\theta_{30}$, $\Delta\theta_{20}$, $\Delta\theta_{30}$ and the corresponding spring energy changes, ΔV_{10}, ΔV_{20} and ΔV_{30} the task is to synthesise spring-lever parameters and determine the reference position of the lever i.e.θ_0 Assuming V_0, V_1 , V_2 and V_3 can be obtained and the Equation (7) can be written down for four positions. And if along with E, p, s, θ_0 is also treated as a variable, spring lever for four energy levels can be synthesised.

Writing equation (7) for four positions,
In the form, [A]{x}={b}
where,

$$[A] = \begin{bmatrix} 2q_0\sqrt{V_0} & 1 & 0 & 1 \\ 2q_1\sqrt{V_1} & \cos\Delta\theta_{10} & -\sin\Delta\theta_{10} & 1 \\ 2q_2\sqrt{V_2} & \cos\Delta\theta_{20} & -\sin\Delta\theta_{20} & 1 \\ 2q_3\sqrt{V_3} & \cos\Delta\theta_{30} & & 1 \end{bmatrix}$$

$$x = \begin{Bmatrix} s\sqrt{E} \\ Ep\cos\theta_0 \\ Ep\sin\theta_0 \\ (s^2-1)E \end{Bmatrix} \quad \text{and } b = \begin{Bmatrix} -V_0 \\ -V_1 \\ -V_2 \\ -V_3 \end{Bmatrix} \qquad (20)$$

Let $r_1 = s\sqrt{E}$, $r_2 = Ep\cos\theta_0$, $r_3 = Ep\sin\theta_0$ and $r_4 = (s^2 - 1)E$. If equation (5) is solvable values of r_1, r_2, r_3 and r_4 can be obtained and from them spring parameters can be obtained as below:

$$E = r_1^2 - r_4 \;, \; s = r_1 / \sqrt{E}$$

$$p = \pm\sqrt{r_2^2 + r_3^2 \big/ E^2}$$

and $\theta_0 = \tan^{-1}(r_3/r_2)$

Ex. 3: For the lever displacements $\Delta\theta_{10}=20^0$, $\Delta\theta_{20}=55^0$, and $\Delta\theta_{30}=65^0$ the corresponding spring energy changes $\Delta V_{10}=500$, $\Delta V_{20}=2250$ and $\Delta V_{30}=2900$ synthesis was carried out, using the procedure given above. Parameters $V_0 = 500$ and $[q_0\ q_1\ q_2\ q_3] = [1\ 1\ 1\ 1]$ were assumed. The design was obtained as E=7938.07, p=0.722, s=0.3215 and θ_0=21.22^0.

Figure 4 shows spring energy variation against the lever position, for the synthesized system. The design points are marked on the graph.

6. FOUR DISPLACEMENTS SYNTHESIS

Given the lever displacement, $\Delta\theta_{10}$, $\Delta\theta_{20}$, $\Delta\theta_{30}$ and $\Delta\theta_{40}$ and the corresponding spring energy change ΔV_{10}, ΔV_{20}, ΔV_{30} and ΔV_{40} and the task is to synthesise spring-lever parameters and determine the reference position of the lever i.e. θ_0. Writing Equation (7) for five positions,

$$(s^2-1)E + 2q_i\sqrt{V_i}\sqrt{E}\,s + v_i + pE\cos\theta_i - 1 = -V_i \qquad i = 0,1,..4 \qquad (7)$$

Above equations were solved iteratively for s, p, V_0 θ_0, and E.

The iterative procedure involves one dimensional search in V_0 along with three displacements synthesis. To start with, for the range of values of V_0, three displacements synthesis is carried out to obtain parameters p, s, θ_0, and E. For all these synthesised mechanisms, the error in ΔV_{40} is found out. From this error, narrow range of V_0 is found out, which will give the suitable design. The procedure is repeated, for this narrow range, to obtain V_0 and other spring-lever parameters which give least error in ΔV_{40}, within the reasonable accuracy. This is, in effect, determining the root of one equation in one variable.

Ex. 4: For the lever displacements $\Delta\theta_{10}=20^0$, $\Delta\theta_{20}=55^0$, and $\Delta\theta_{30}=145^0$ and $\Delta\theta_{40}=200^0$ and the corresponding spring energy changes $V_{10}=500$, $V_{20}=1000$ and $V_{30}=-1000$ and $V_{40}=1500$ synthesis was carried out, using the procedure, given above. The design, based on least error, was obtained as,
V_0= 4550, p=0.999, s=4.93, θ_0=-46.6^0, E=238.06.

Figure 5 shows the spring energy variation vs lever position for the synthesised system. The design points are marked on the graph.

7. PROCEDURE TO OBTAIN SPRING PARAMETERS

Synthesis procedure gives E, p, s, θ_0 and V_0. The locations of the spring ends on the lever and the ground are obtained by the following Equations, after assuming suitable stiffness of the spring 'k'.

$$a = 0.5\left(\sqrt{\frac{2E}{k}}\right)\left(\sqrt{1+p} + \sqrt{1-p}\right)$$

$$b = 0.5\left(\sqrt{\frac{2E}{k}}\right)\left(\sqrt{1+p} - \sqrt{1-p}\right)$$

The dimensionalised free length of the spring is given by

$$S = s\left(\sqrt{\frac{2E}{k}}\right)$$

Design of spring is carried out by the usual procedure. Stiffness already assumed, the spring index, the ratio of free length to the mean coil diameter, is also assumed. And for the selected material, the spring wire diameter and the number of turns are obtained. This procedure may also need some iteration to get a suitable spring design. For example for a system, in which lever has to travel through an angle of 120^0 and has parameters, E=138.33, p=0.272,s=0.635, θ_0=-60^0, the dimensions of the system for k=5000 N/m will be obtained as a=233.0 mm, b=32.3 mm, S=149.4 mm. For spring material having G=80 GPa, allowable shear stress 300 MPa, the spring details will be as mean dia. =59.7 mm, wire diameter=6 mm and the number of turns=14.

8. CONCLUSION

Spring-actuated lever synthesis for energy differences and the displacements co-ordination has been presented. The synthesis procedure, upto three displacements, is non-iterative and needs iteration in one dimension, for four displacements synthesis. Moreover, the spring used, for the synthesis, is not of zero free length. The proposed synthesis procedure does not find out the spring stiffness explicitly. It is selected at the end, from the design parameters, so that a system is scaled to the suitable dimensions. The precision point synthesis capability is maximum up-to four displacements. However, for an arbitrarily specified three/four energy differences and the corresponding displacements it will always not be possible to get a feasible design i.e. $s>0$, $E>0$, $-1 < p < 1$ and $q_i w_i + s > 0$. This is because the three parameters E, p and s are bounded. As far as two displacements synthesis is concerned, it will always be possible to synthesise a system, by a suitable choice of the free variables E and V_0. In three displacements synthesis E and in four displacements synthesis E and V_0 are not the free variables and the energy pattern can not be manipulated as is possible for two displacements synthesis. And therefore, for arbitrarily specified three/four energy differences and the corresponding displacements it can not be said with certainty that a feasible solution will be obtained. Moreover, it may not give a well-proportioned system. In that case, the synthesis will have to be carried out by the optimisation technique.

REFERENCES

[1] Kurt Hain, "Spring Mechanisms-force Analysis, Production Engineering", 1961, pp. 268-270.

[2] Kurt Hain, "Spring Mechanisms-point Balancing, Production Engineering", 1961, pp.271-273.

[3] Kurt Hain, "Spring Mechanisms-Continuous Balancing, Production Engineering", 1961, pp 274-275.

[4] P.I Genova, "Synthesis of Spring Equivalent to Flywheel for Minimal Co-efficient of Fluctuation", ASME Miscellenous Papers, 68-Mech-65, pp.1-5.

Nonlinear Free Vibrations of Rhombic Sandwich Plates

Gora Chand Chell[1], Subrata Mondal[2] and Goutam Bairagi[3]

[1]Department of Mechanical Engineering, [3]Department of Civil Engineering, Jalpaiguri Government Engineering College, Jalpaiguri - 735 102, India.

[2]Birla Institute of Technology, Kolkata - 700 050, India.

E-mail: gcchell@rediffmail.com

(Received on 06 July 2008 and accepted on 15 June 2010)

Abstract

This paper represents nonlinear free vibrations of rhombic sandwich plates using Banerjee's hypothesis where a new form of energy expression in the total potential energy of the system has been employed. As a consequence the differential equation is decoupled keeping intact its nonlinear character. Analyses of nonlinear dynamic behaviors of rhombic sandwich plates have been carried out completely. Numerical results (ratio of nonlinear frequency and linear frequency vs. $w/2h_1$*) have been computed and compared with known results for square sandwich plates only. Results for different skew angles are obtained and believed to be new.*

Keywords: *Free vibration, Frequency ratio, Nonlinear, Rhombic sandwich plates*

1. INTRODUCTION

The free vibration analysis of different elastic structures is of great importance in the field of applied mechanics, civil and aerospace engineering [1]. Particular evaluation of large amplitude free vibrations of basic structures like beams, plates and shells is essential for studying the behavior of the present day optimized and cost- effective structural members subjected to severe dynamic environment. Important papers in this field are due to Narita [2], Rao & Saheb [3], Sasajima, Kakudate & Narita [4], Wu, Liu, Chen [5].

Narita [2] analyzed the free vibration of isotropic and anisotropic rectangular thin plates using modified Ritz method. Rao & Saheb [3] gave a simple formula to predict the fundamental frequencies of initially stressed square plates. He also presented simple formula for large amplitude free vibrations of beams and plates. Sasajima, Kakudate & Narita [4] presented free vibration analysis and an optimal design approach for thick isotropic rectangular plates with varying thickness under general edge conditions. Very recently Wu, Liu, Chen [5] provides an exact solutions for free vibration analysis of rectangular plates by thin plate theory using Bessel function. All these papers are restricted to rectangular boundary only.

It is well known that a good number of structural design utilizes sandwich type construction in the fabrication of major structural components. A high strength to weight ratio is achieved by combining a relatively thick light weight core with two thin high strength faces. The problems of large deflection of sandwich plates have been investigated by several authors, among which works of Reissner [6], Wang [7], Hoff [8] and Eringen [9] need special mention. Reissner [6] presented an exact analysis of finite deflection of sandwich plates. Wang [7] gave a general theory of large deflections of sandwich plates and shells. Hoff [8] and Eringen [9] each developed a theory of bending and buckling of sandwich plates. All these investigations are, however, confined to rectangular sandwich plates under mechanical loading only. Kamiya [10] employed Berger's well known technique to solve nonlinear problems of sandwich plates using a new set of governing equation with a correction factor. This work has been restricted to a particular plate geometry.

Dutta and Banerjee [1] offered a simple approach to investigate nonlinear static as well as dynamic behaviours of sandwich plates. Nayak, Moy & Shenoi [11] determined natural frequencies of isotropic, orthotropic, layered anisotropic composite and sandwich plates using finite element formulations of Reddy's higher order theory. Yuan & Dawe [12] also predicted natural frequencies & modes of conventional rectangular sandwich plates using spline finite strip method.

Some more interesting papers on sandwich structure could be located [13-16] where analysis have been carried out elegantly and these papers are attractive to design engineers. Careful survey of the literature on nonlinear analysis of skew sandwich plates reveals that no proper attention has been given so far to this field. But the analysis of the nonlinear behavior of skew sandwich plates is gaining momentum day by day due to heavy demands in space industry. A very few papers in this field could be located [17-20] which are quite interesting. The aim of the present study is to employ a set of uncoupled differential equations in oblique coordinates to analyze nonlinear free vibrations of rhombic sandwich plates using Banerjee's hypothesis [1]. To obtain the final solution (ratio of nonlinear frequency and linear frequency vs. $\bar{w} / 2h_1$) for simply supported rhombic sandwich plates both for movable and immovable edges well known Galerkin technique has been used.

Numerical results thus obtained for different skew angles have been plotted in graph (both for movable & immovable edges). Results for square sandwich plates are compared with the known results [1, 21] using $\theta = 0$ and other results for different skew angles are believed to be completely new.

2. GOVERNING EQUATIONS

We consider a rhombic sandwich plate with an isotropic core as well as isotropic upper & lower faces of identical thickness; while the faces respond to the bending and membrane action of the plate, the core is assumed to transfer only shear deformation. Moreover the thickness of upper & lower faces is sufficiently thin in comparism with core thickness (h>>t) to ignore a variation of shear in the thickness direction of the faces. The free harmonic vibration of a sandwich plates of rectangular shape is governed by the following differential equation [1]:

$$\frac{2EtI_1^m}{(1-\nu^2)}\left\{\frac{\partial^2 w}{\partial x^2}+\nu.\frac{\partial^2 w}{\partial y^2}\right\}+hG'\nabla^2 w-G'\left(\frac{\partial r}{\partial x}+\frac{\partial s}{\partial y}\right)$$
$$+\frac{Et\lambda}{(1-\nu^2)}\left\{\left[\left(\frac{\partial w}{\partial x}\right)^2+\left(\frac{\partial w}{\partial y}\right)^2\right]\nabla^2 w+2\left(\frac{\partial w}{\partial x}\right)^2\frac{\partial^2 w}{\partial x^2}\right.$$
$$\left.+2.\left(\frac{\partial w}{\partial y}\right)^2\frac{\partial^2 w}{\partial y^2}+4.\frac{\partial^2 w}{\partial x\partial y}.\frac{\partial w}{\partial x}.\frac{\partial w}{\partial y}-\right\}$$
$$-(\phi_1 t+\phi_2 h)\frac{\partial^2 w}{\partial T^2}=0 \qquad \ldots (1)$$

$$I_1^m = cf(T)$$
$$=\frac{\partial}{\partial x}\left(u^u+u^l\right)+\nu\frac{\partial}{\partial y}\left(v^u+v^l\right)$$
$$+\frac{1}{2}\left(\frac{\partial w}{\partial x}\right)^2+\frac{\nu}{2}\left(\frac{\partial w}{\partial y}\right)^2 \qquad \ldots (2)$$

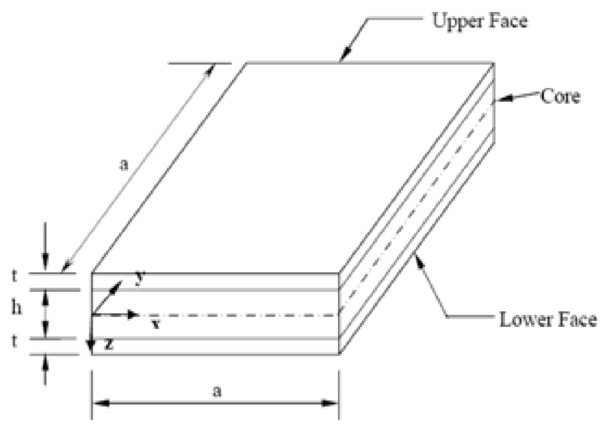

Fig.1(a)

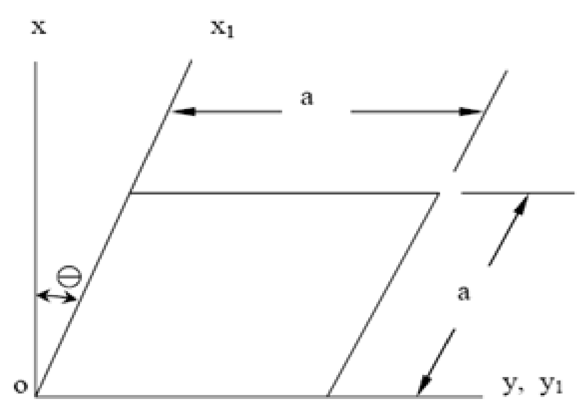

Fig. 1b (Skew sandwich plate)

For skew angle θ, (Fig. 1b) we get the following transformation :

$$\frac{\partial^2}{\partial x^2} = \sec^2\theta\left(\frac{\partial^2}{\partial x_1^2} - 2\sin\theta\frac{\partial^2}{\partial x_1\partial y_1}\right) + \tan^2\theta\frac{\partial^2}{\partial y_1^2}$$

$$\frac{\partial^2}{\partial y^2} = \frac{\partial^2}{\partial y_1^2}$$

$$\nabla^2 = \sec^2\theta\left(\frac{\partial^2}{\partial x_1^2} - 2\sin\theta.\frac{\partial^2}{\partial x_1\partial y_1} + \frac{\partial^2}{\partial y_1^2}\right)$$

$$\frac{\partial}{\partial x} = \sec\theta\left(\frac{\partial}{\partial x_1} - \sin\theta\frac{\partial}{\partial y_1}\right)$$

$$\frac{\partial}{\partial y} = \frac{\partial}{\partial y_1}$$

$$\frac{\partial^2}{\partial x\partial y} = \sec\theta\left(\frac{\partial^2}{\partial x_1\partial y_1} - \sin\theta\frac{\partial^2}{\partial y_1^2}\right)$$

Putting the above transformation in Eqs (1) and (2), we get the following set of differential equations:

$$w = \bar{w}\sin\frac{\pi x_1}{a}\sin\frac{\pi y_1}{a}F(T) \qquad \frac{2Et\,I_1^m}{(1-\nu^2)}$$

$$\left\{\sec^2\theta\left(\frac{\partial^2 w}{\partial x_1^2} - 2\sin\theta\frac{\partial^2 w}{\partial x_1\,\partial y_1}\right) + \tan^2\theta\frac{\partial^2 w}{\partial y_1^2} + \nu\frac{\partial^2 w}{\partial y_1^2}\right\}$$

$$+hG'\sec^2\theta\left(\frac{\partial^2 w}{\partial x_1^2} - 2\sin\theta.\frac{\partial^2 w}{\partial x_1\partial y_1} + \frac{\partial^2 w}{\partial y_1^2}\right) -$$

$$G'\left\{\sec\theta\left(\frac{\partial r}{\partial x_1} - \sin\theta\frac{\partial r}{\partial y_1}\right) + \frac{\partial s}{\partial y_1}\right\} +$$

$$\left[\begin{array}{l}\left\{\sec^2\theta\left(\frac{\partial w}{\partial x_1} - \sin\theta\frac{\partial w}{\partial y_1}\right)^2 + \left(\frac{\partial w}{\partial y_1}\right)^2\right\} \\ \sec^2\theta\left(\frac{\partial^2 w}{\partial x_1^2} - 2\sin\theta.\frac{\partial^2 w}{\partial x_1\partial y_1} + \frac{\partial^2 w}{\partial y_1^2}\right)\end{array}\right.$$

$$\frac{Et\lambda}{(1-\nu^2)}\left|\begin{array}{l} +2\left\{\sec\theta\left(\frac{\partial w}{\partial x_1} - \sin\theta\frac{\partial w}{\partial y_1}\right)\right\}^2 . \left\{\begin{array}{l}\sec^2\theta\left(\frac{\partial^2 w}{\partial x_1^2} - 2\sin\theta\frac{\partial^2 w}{\partial x_1\partial y_1}\right) \\ +\tan^2\theta\frac{\partial^2 w}{\partial y_1^2}\end{array}\right\} \\ +2\left(\frac{\partial w}{\partial y_1}\right)^2\frac{\partial^2 w}{\partial y_1^2} \\ +4\sec\theta\left(\frac{\partial^2 w}{\partial x_1\partial y_1} - \sin\theta\frac{\partial^2 w}{\partial y_1^2}\right)\sec\theta\left(\frac{\partial w}{\partial x_1} - \sin\theta\frac{\partial w}{\partial y_1}\right)\frac{\partial w}{\partial y_1}\end{array}\right]$$

$$-\left(\phi_1 t + \phi_2 h\right)\frac{\partial^2 w}{\partial T^2} = 0 \qquad (3)$$

$$I_1^m = cf(T)$$

$$= \frac{\partial}{\partial x}\left(u^u + u^l\right) + \nu\frac{\partial}{\partial y}\left(v^u + v^l\right) +$$

$$\frac{1}{2}\left\{\sec\theta\left(\frac{\partial w}{\partial x_1} - \sin\theta\frac{\partial w}{\partial y_1}\right)\right\}^2 + \frac{\nu}{2}\left(\frac{\partial w}{\partial y_1}\right)^2 \qquad (4)$$

3. ANALYSIS

Let us assume (5)

where, $F^2(T)=f(T)$

This form of w clearly satisfies the required simply supported edge conditions. It is to be noted that to determine the desired solution, w has been chosen in the form of double sine series ensuring convergence of the solution. Moreover putting this form of w in the given differential equation , we get the error function $\in(x, y)$

because $w = \bar{w}\sin\frac{\pi x_1}{a}\sin\frac{\pi y_1}{a}F(T)$ is not the exact solution of the differential equation. We are now required to minimize this error by using the well known Galerkin's Technique. This technique gives $\iint \in(x, y)\,dxdy = 0$

Thus the solver of the differential equation is Galerkin's Technique involving the evaluation of the above double integrals, which is simple. If we now integrate equation (4) over the entire plain area of the plate we get

$$I_1^m = \frac{\bar{w}}{8}\frac{\pi^2}{a^2}\;(1+\nu)F^2(T) \qquad (6)$$

It is to be noted that for movable edge conditions $I_1^m = 0$ Putting (5) & (6) in equation (3), we get the error function , $\in(x, y)$, Galerkin's Technique requires

$$\iint \in (x, y) dxdy = 0 \qquad (7)$$

Evaluating the integrals in (7) we get the following form of cubic equation:

$$F + AF + BF^3 = 0 \qquad (8)$$

$$\text{where,}\quad A = \frac{1}{(\phi_1 t + \phi_2 h)} . 2\pi^2 . \frac{G' h}{a^2} . \sec^2\theta$$

$$= \frac{1}{(\phi_1 t + \phi_2 h)} \frac{Et}{(1-\nu^2)} \left[\begin{array}{l} \frac{1}{4}(1+\nu)(\sec^2\theta + \tan^2\theta + \nu) + \\ \lambda \left\{ \begin{array}{l} \frac{1}{8}\sec^2\theta(3\sec^2\theta + \tan^2\theta + 3) + \\ \frac{1}{8}\sec^2\theta \begin{pmatrix} 3\sec^2\theta + 2\tan^2\theta \\ + 3\tan^2\theta\sin^2\theta \end{pmatrix} \\ + \frac{3}{8} - \frac{1}{4}\sec^2\theta(1 - 3\sin^2\theta) \end{array} \right\} \end{array} \right] (\bar{w}) \frac{\pi^4}{a^4}$$

4. NUMERICAL RESULTS

Tables and corresponding graphs show the results of the ratio of nonlinear frequency to linear frequency for different values of

$\left(\frac{\bar{w}}{2h_1}\right)$ of a rhombic sandwich plates with the following dimensions :

$E = 73472.01 \times 10^6$ N/m^2
$t = 0.635 \times 10^{-3}$ m
$\nu = 0.3$
$G = 42184.884 \times 10^3$ N/m^2
=
$a = 0.254$ m
$h = 1.7135 \times 10^{-2}$ m

Table 1 For Immovable Edge Condition for $I_1^m = 0$

$\frac{\bar{w}}{2h_1}$	$\frac{w^*_1}{w_1}$					
	$\theta=0^0$			$\theta = 30^0$	$\theta = 45^0$	$\theta = 60^0$
	(Calculated)	(Known)	(Known)			
0	1	1	1	1	1	1
0.5	1.116	1.12	1.14	1.13	1.166	1.2289
1.0	1.408	1.42	1.48	1.473	1.5621	1.7438
1.5	1.792	1.82	1.86	1.906	2.0592	2.3647
2.0	2.2209	2.24	2.38	2.3834	2.600	3.0271

Table 2 For Movable Edge Condition for $I_1^m = 0$

$\frac{\bar{w}}{2h_1}$	$\frac{w^*_1}{w_1}$				
	$\theta=0^0$ (Calculated)	$\theta=0^0$ (Known)[1]	$\theta = 30^0$	$\theta = 45^0$	$\theta = 60^0$
0	1	1	1	1	1
0.5	1.025	1.024	1.0355	1.0553	1.1125
1.0	1.0985	1.094	1.1354	1.2061	1.3967
1.5	1.2104	1.202	1.2848	1.4224	1.7719
2.0	1.3516	1.338	1.4686	1.6790	2.1918

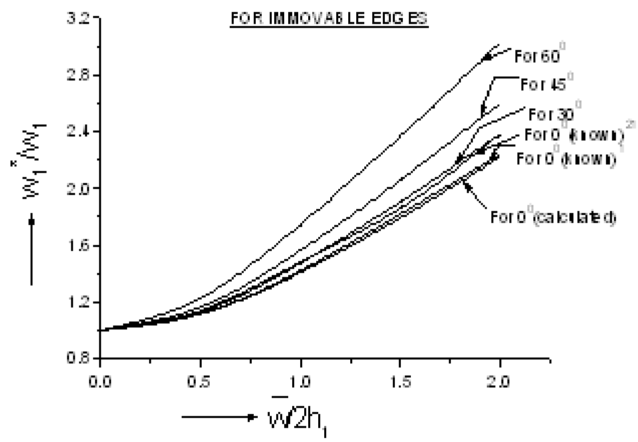

Fig.1 For Immovable edges

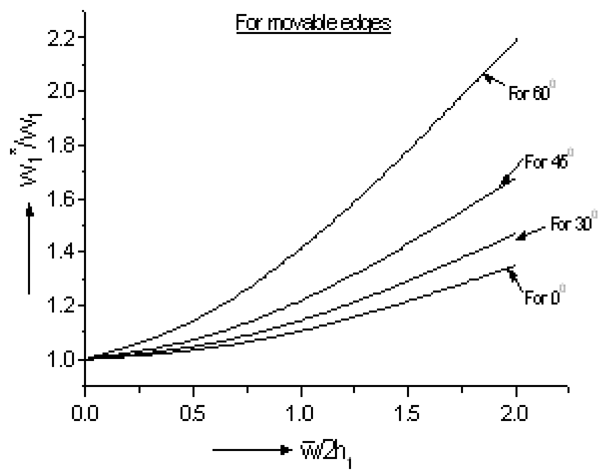

Fig.2 For movable edges

5. CONCLUSION

The proposed differential equations are uncoupled and thus simple. From the same Eq. (8), numerical results (ratio of nonlinear frequency and linear frequency vs. $\frac{\bar{w}}{2h_1}$) for immovable and movable edge conditions can be obtained. Numerical results (both for immovable and movable edge conditions) for rhombic sandwich plates are obtained for different skew angles and presented those in tables. For square sandwich plates the results are compared with those of known results[1,21] and are found in good agreement. The results for the other skew angles are believed to be completely new. The numerical results presented in different tables for different skew angles, offer an interesting observation. As θ increases i.e., as the plate tends towards rhombic shape, frequency ratio increases. This is quite expected because with the increase of skew angles, the plate offers more rigid structure, which means it is less deflected. As we know frequency is inversely proportional to the square root of deflection, so frequency ratio will be more in this case. Tables and graphs show that frequency ratio is greater for immovable edge conditions than those of movable edge conditions. It is quite natural that rigidity of the structure is more in case of immovable edge conditions compared to movable edge conditions. So the structure for immovable edge conditions is less deflected, which means frequency ratio is more. Therefore from design point of view rhombic sandwich plates are more accepted.

NOMENCLATURE

E = Young's Modulus.

w, = Amplitude parameter

ν = Poisson's Ratio.

a = Size of Plate.

t = Face Thickness.

h = Core Thickness.

= Shear Modulus.

h_1 = Thickness parameter

ϕ_1 = Surface density

ϕ_2 = Core density

F(T) = Function of time

u, v, w = Amplitude in x, y, z directions respectively.

λ = Constant depending on the poisson's ratio of the plate materials.

= First invariant of average face strain

θ = Skew Angle

REFERENCES

[1] S. Dutta and B. Banerjee, "Governing Equations for Non-linear Analysis of Sandwich Plates - A New Approach", International Journal of Nonlinear Mechanics, Vol.26, No.34, 1991, pp.313-318.

[2] Y.Narita, "Combinations for the Free-vibration Behaviors of Anisotropic Rectangular Plates Under General Edge Conditions", Journal of Applied Mechanics, ASME, Vol.67, 2000, pp. 568-573.

[3] G.Venkateswara Rao and K.Meera Saheb, "Simple Formula to Study the Large Amplitude free

Vibrations of Beams and Plates", Journal of Applied Mechanics, ASME, Vol.75, 2008, pp.1-5.

[4] M.Sasajima, T.Kakudate and Y.Narita, "Vibration Behavior and Simplified Design of Thick Rectangular Plates with Variable Thickness", Journal of Applied Mechanics, ASME, Vol.124, 2002, pp.302-309.

[5] Wu Jiu Hui, A.Q.Liu and H.L.Chen, "Exact Solutions for Free-vibration Analysis of Rectangular Plates Using Bessel Functions", Journal of Applied Mechanics, ASME, Vol.74, 2007, pp.1247-1251.

[6] E.Reissner, "Finite Deflection of Sandwich Plates", Journal Aeronautical Science, Vol.15, 1948, pp. 435-440.

[7] C.T.Wang, "Principle and Application of Complementary Energy Method for Thin Homogeneous and Sandwich Plates and Shells with Finite Deflections", NACA Technical Note 2620, 1952, pp.1-34.

[8] N.J.Hoff, "Bending and Buckling of Rectangular Sandwich Plates", NACA Technical Note 2225, 1950, pp.1-29.

[9] A.C.Eringen, "Bending and Buckling of Rectangular Sandwich Plates", Proc 1st U.S. Nat Cong Applied Mechanics, ASME New York, 1951, pp. 381-390.

[10] N.Kamiy, "Governing Equations for Large Deflections of Sandwich Plates", AIAA J, Vol.14, No.2, 1976, pp. 250-253.

[11] Nayak, Moy and Shenoi, "Free Vibration Analysis of Composite Sandwich Plates Using Assumed Strain Plate Bending Elements Based on Higher Order Theory", Composites Part B: Engineering, Vol.33, No.7, 2002, pp.505-519.

[12] W.X.Yuan and D.J.Dawe, "Free Vibration of Sandwich Plates With Laminated Faces", International Journal for Numerical Methods in Engineering, Vol.54, No.2, 2002, pp. 195-217.

[13] W.X.Yuan and D.J.Dawe, "Free Vibration and Stability Analysis of Stiffened Sandwich Plates", Compos. Struct., 63, 2004, pp.123-137.

[14] S.V.Sorokin and O.A.Ershova, "Forced and Free Vibrations of Rectangular Sandwich Plates with Parametric Stiffness Modulation", Journal of Sound and Vibration, Vol.259, No.1, 2003, pp.119-143.

[15] C.M.C.Roque, A.J.M.Ferreira and R.M.N.Jorge, "Free Vibration Analysis of Composite and Sandwich Plates By A Trigonometric Layer Wise Deformation Theory and Radial Basis Functions", Journal of Sandwich Structures and Materials, Vol.8, No.6, 2006, pp. 497-515.

[16] Kim Jun-Sik and Cho Maenghyo, "Enhanced First-order Shear Deformation Theory for Laminated and Sandwich Plates", Journal of Applied Mechanics, ASME, Vol.72, 2005, pp.809-817.

[17] A.K.Ray, B.Banerjee and B.Bhattachatjee, "Nonlinear Analysis of Skewd Sandwich Plates", Journal of Meccanica,1993, pp.211-216.

[18] S.A.Kulkarni and K.M.Bajoria, "Geometrically Nonlinear Analysis of Smart Thin and Sandwich Plates", Journal of Sandwich Structures and Materials, Vol.8, No.4, 2006, pp. 321-341.

[19] P.Vangipuram and N.Ganesan, " Buckling and Vibration of Rectangular Composite Viscoelastic Plates Under Thermal Loads", Journal of Composite Structures, Vol.77, No.4, 2007, pp. 419-429.

[20] G.C. Chell, S.Mondal and G.Bairagi, "Large Deflection Analysis of Rhombic Sandwich Plates Placed on Elastic Foundation", Indian Journal of Engineering & Materials Sciences, Vol.15, 2008, pp. 69-76.

[21] B.M.Karmaker,"Amplitude-frequency Characteristics of Large Amp. Vibrations of Sandwich Plates", J. Appl. Mech. Trans. ASME, Vol.46, No.1, 1978, pp. 230-231.

Numerical Modelling of Regenerators in Cryogenic Pulse Tube Refrigerators

B. Jayaraman[1] and P. Senthil Kumar[2]
[1]Sathyabama University, Chennai - 600 119, Tamil Nadu
[2]KSR College of Engineering, Tiruchengode - 637 215, Tamil Nadu
E-mail: tabjayaraman@yahoo.co.in
(Received on 22 December 2008 and accepted on 12 March 2010)

Abstract

Performance of regenerative Cryocoolers is a strong function of the storage type regenerator's performance. The complexities arising due to unsteady, oscillating compressible gas flow in the stacked porous media called regenerator leads to inefficiencies. A mathematical model simulating the regenerator is developed and numerically solved by finite difference technique. Performance parameters predicted by the developed computer program is analysed for single mesh regenerators. In a wire mesh type regenerator, the pressure drop term is large at the warm end and the effectiveness term is large at the cold end. An effectiveness of 0.9907 is obtained for the 400 Mesh regenerator and pressure drop during Compression calculated as 126.8 kPa. The effectiveness is primarily a function of the matrix element size. Larger mesh number regenerators have larger effectiveness, but the flow losses increase proportionately.

Keywords: *Cryocooler, Cryogenics, Orifice pulse tube refrigerator, Regenerator, Simulation*

1. INTRODUCTION

A thermal sponge absorbing energy into its solid phase, when exposed to a hot fluid medium and releasing it to the cold fluid at a later stage in a cycle periodically is called regeneration. Regenerators, based on this principle are used in Cryocoolers. The Regenerator losses become especially large at low temperature range. A reduction in the losses due to regeneration can lead to a significant increase in the net refrigeration power for the same power input. The Pulse Tube Cryocoolers needs relatively higher mass flow rates compared to the G-M or Stirling Cryocooler, which further decreases the efficiency of regenerator. An efficient regenerator must have a large thermal inertia per unit volume to support high volumetric heat transfer with the working fluid, and at the same time with small pressure drops. The complexities in simulating a Cryocooler are due to the unsteady, oscillating compressible gas flow in the stacked porous media in regenerator. The overall performance of refrigerators is a strong function of the storage type regenerator's performance. The complexities in simulating a PTR are due to the unsteady, oscillating compressible gas flow in the stacked porous media in regenerator. Willmott and others have developed numerical solution techniques for the single mesh regenerators and analysed its performance [1]. Atrey *et al.* simulated the single mesh regenerator for Stirling cycle cryocoolers [2]. Detailed analytical studies and theoretical design methodologies for the regenerator of a PTR is lacking. In the present work a Computational Fluid Dynamics (CFD) analysis of mesh type regenerator in an OPTR is simulated for evaluating its performance. The losses occurring during regenerator operation are analysed and discussed.

2. REGENERATOR SIMULATION

To develop the mathematical model describing the exchange, the energy balance for the matrix material and working fluid in a control volume of the regenerator is established by employing the 1st law of Thermodynamics, conservation of mass, momentum, and heat transfer equation of fluid with matrix.

2.1 Mathematical Model

To develop the mathematical model describing the exchange, the energy balance for the matrix material and fluid in a small element or control volume of the regenerator is established by employing the 1st law of Thermodynamics, conservation of mass, heat transfer equation and the equation of motion of fluid. The overall balance for the control volume is written in mathematical form as

$$[dQ_c+dQ_f]_z+[dQ_ç]_z=[dQ_c+dQ_f]_{z+Äz}+[Md_e]_{z+Äz/2} \qquad (1)$$

Similarly the Energy balance for the fluid in the control volume is derived as follows

$$\{dQ_f\}_z + \{[dQ_\eta - dQ_h]\} = \{dQ_f\}_{z+\Delta z} + \{(pC_p\delta V)_f dT_f\} \qquad (2)$$

Where the heat inflow and outflow consists of heat conducted dQ_c, into and out of the control volume through the matrix material and the heat transported into and out of the control volume by the fluid dQ_f. The internal sources consist of frictional heating and the change in internal energy is given by the mass and the enthalpy of the material enclosed by the control volume.

Equations (1) and (2) are complex when all the aspects are considered. To obtain solutions the equations are simplified using suitable assumptions [3] to obtain

(3)

(4)

The governing partial differential equations derived are nondimensionalized, discretised and solved to predict the temperature distribution of working fluid and matrix along the length of the regenerator.

2.2 Numerical Scheme

The Λ–Π technique in the modified form is used to solve the differential equations by converting them into algebraic equations by the explicit form of finite difference technique [3]. The solution procedure starts with the dimensionless system of equations. It is obtained by defining normalised independent variables and temperatures as follows:

Normalised length y = z / L
Normalised period q = (t - z / u) / P
Normalised temperature ě (y, q) = Tj (y, q) - T_2,in / (T_1,in - T2,in), where j = 1,2, m
After normalising, the Equations (3) and (4) becomes

$$U\frac{\partial\theta}{\partial y} + \frac{d\theta_m}{dq} = 0 \qquad (5)$$

$$\frac{\partial\theta_f}{\partial y} + \Lambda(\theta_f - \theta_w) = 0 \qquad (6)$$

The time and length derivative in normalised Eq. (5) is replaced by a central difference approximation about nodal point (n+1/2, i) to obtain the following algebraic equation [3]

$$\theta_m(n+1, i) - A_1\theta_m(n,i) - A_2(\theta_f(n+1, i) + \theta_f(n,i)) = 0 \qquad (7)$$

where $A_1 = 2 - \Lambda U.q / (2 + \Lambda U.q)$ and $A_2 = \Lambda U.q / (2 + \Lambda U.q)$. The fluid balance Eq.(6) is converted into an algebraic equation by replacing the length derivative by a central difference derivative approximation about the nodal points (n+1, i-1/2) to give [3]

$$\theta_f(n+1, i) - B_1\theta_f(n+1,i-1) - B_2(\theta_m(n+1, i) + \theta_m(n+1,i-1)) = 0 \qquad (8)$$

where $B_1 = 2 - Ë.y / (2 + Ë.y)$ and $B_2 = Ëy / (2 + Ëy)$. The matrix temperature is obtained from substituting Eq. 8 in Eq. 7 to give [3]

$$\theta_m(n+1, i) - k_1\theta_m(n+1, i-1) + k_2\theta_m(n, i) + k_3\theta_f(n+1, i-1) + k_4\theta_f(n,i) = 0 \qquad (9)$$

where $k_1 = A_1 / (1 - A_2 B_2)$; $k_2 = A_2 B_2 / (1 - A_2 B_2)$; $k_3 = A_2 B_1 / (1 - A_2 B_2)$ and $k_4 = A_2 / (1 - A_2 B_2)$. The algebraic equations are used in the simulation program of a regenerator.

2.3 Solution Procedure

The numerical solution procedure is given below.

- Dimensionless time and space coordinates z and q are represented by a system of nodal points on a mesh arrangement of size z and q. Each nodal point may be signified by the notation (n, i), where n = time step and i = length step. The number of time and length step depends on the stability criteria.
- The Pulse Tube Refrigerator system configuration, its operating conditions are specified and boundary conditions of the regenerator is assigned.
- The temperature of matrix and fluid at each node is calculated after one time step given the condition at

the beginning of that time step. At any given instant having known the temperatures at (2,1), (1,1), (1,2) the temperature at 2,2 can be found.

- The process is repeated for the cold period of the cycle. The temperature profile at the end of the hot period is taken as the profile at the beginning of the cold period. The constant for Eq. (9) is changed to account for the unbalance factor and non symmetry factor.
- The time step calculations are continued for several cycles of flow of fluid until quasi steady state is reached, when the difference in temperature at each node between 2 cycles is less than a given tolerance. Convergence to cyclic equilibrium is checked after the evaluation of a complete cycle.
- The numerical solution finds both gas and solid temperatures at each nodal point in the mesh covering the time and space domain.
- The effectiveness and losses in the regenerator is calculated. The effectiveness is given by the dimensionless fluid temperature at the exit of the matrix

$$\varepsilon = \frac{T_{g.h.out} - T_{g.h.in}}{T_{g.h.in} - T_{g.c.in}} \tag{10}$$

The temperature profile and performance parameters for given input conditions are printed for the regenerator.

Losses in the regenerator influence the performance by increasing the net power input and decreasing the refrigerating capacity of the system. The decrease in refrigeration capacity is due to regenerator ineffectiveness, irrecoverable pressure drop, and longitudinal conduction through the matrix and regenerator tube. The regenerator ineffectiveness is the loss due to imperfect heat transfer. The reheat loss of the cold gas is also associated with the ineffectiveness of the regenerator. Also, the fluid and matrix properties vary as a function of pressure and temperature. Materials at low temperature lose their specific heat. The reduced specific heat results in a reduction of the heat capacity and thereby the performance of regenerator due to increased matrix swing. Empirical relations of fluid and matrix properties as a function of temperature enables the accurate calculation of pressure drop and heat transfer coefficients at each node along the regenerator in the numerical solution.

A regenerator simulation computer program (QUICKBASIC v 4.5) using the above mathematical model is developed. Performances are calculated for a regenerator of a PTR developed by Kral *et al.* [6].

The performance parameters of the regenerator predicted by the program are given in Table 1 and the losses plotted for a particular time step in Figure 1. The figure shows the loss due to conduction, pressure drop of fluid and effectiveness of 400 mesh at a particular time step, along the length of the regenerator with the hot end at the left and the cold end at right.

Table 1 400 Mesh Regenerator Performance Predicted by the Computer Program

Input Conditions	Performance parameters
Cold End Temperature 80 K Warm end temperature 293 K Charge Pressure 16.5 bar Length of Regenerator 103 mm Mesh size 400 Mesh Diameter of Regenerator 11.7 mm Material Stainless Steel	Effectiveness 0.9907 Conduction loss in Matrix 0.0129W Conduction Loss in regenerator tube 0.478 W Conduction loss in Pulse tube 0.312 W Reheat loss in Matrix 0.0286 W Pressure drop during Compression 0.1268 bar Expansion 0.1699 bar

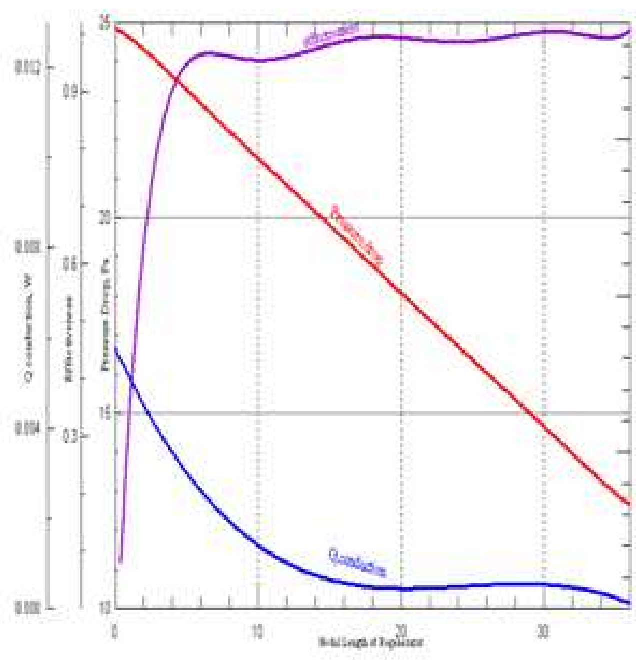

Fig.1 Effectiveness and losses along the nodal length of regenerator in Kral' s PTR system [9]

The total loss of the regenerator is the sum of losses due to flow resistance, ineffectiveness and axial conduction. The effectiveness is primarily a function of the matrix element size. The loss due to conduction, pressure drop of the flowing fluid and effectiveness at a particular time step, along the length of regenerator with the hot end entry at the left and cold end at right is plotted in Figure 1. The pressure drop term is large at the warm end and effectiveness term is high at the cold end. The effectiveness is primarily a function of the matrix element size. Larger mesh number regenerators give higher effectiveness, but the flow losses increase proportionately. The performance parameters for the same input conditions are compared with the method of analysis of Ackerman *et al.*[5]. The effectiveness obtained by this method is 0.99632, thus validating the computer program developed.

3. CONCLUSIONS

A mathematical model simulating the regenerator is developed and numerically solved by using finite difference technique. The algebraic equations derived are coded in a computer program. Performances predicted by the simulation program for a single mesh regenerator for Kral et al OPTR system under specific operating conditions are obtained. An Effectiveness of 0.9907 is obtained for the 400 Mesh regenerator with Pressure drop during Compression calculated as 0.1268 bar. In a given wire mesh type regenerator, the pressure drop term is large at the warm end and the effectiveness term is large at the cold end. The effectiveness is primarily a function of the matrix element size. Larger mesh number regenerators have larger effectiveness, but the flow losses increase proportionately.

4. NOMENCLATURE

A	Area, m2
P	Pressure
F	factor for contact resistance
m	mass flow rate
K	Thermal Conductivity, W/mK
c	specific heat
Q	Heat, W
T	Temperature, K

Subscripts

por	porosity
g	gas
U	Utilisation factor
h	hot
z	length
s,m	matrix
t	time
f	fluid
n	time step
eq	equivalent

Greek

ρ	density
ε	Regenerator ineffectiveness
β	opening area ratio of regenerator
θ	Non dimensional Temperature
γ	ratio of specific heats
η	frictional heating
Λ	Reduced length, given by the relation $h A_v L / G C_p$
Π	Reduced Period

REFERENCES

[1] S. Sarangi and H.S. Baral, “Effects of Axial Conduction in the Fluid on Cryogenic Regenerator Performance”, Cryogenics, Vol 27, 1987, pp.505-509.

[2] M.D.Atrey, S.L. Bapat and K.G.Narayankhedkar, “Theoretical Analysis and Performance Investigation of Stirling Cycle Regenerators”, Cryogenics, Vol. 31, 1991, pp.1044-1052.

[3] P.J. Heggs, “Design and Operational Flexibility of thermal Regenerators”, Heat Exchange Engineering, Vol. 1, Foumeny and Heggs, Ellis Horwood Publication, 1991.

[4] H. Miyabe, S. Takahashi and K. Hamaguchi, “An Approach to the Design of Stirling Engine Regenerator Matrix Using Packs of Wire Gauzes”, Proc. 17th IECEC, 1982, pp.1839-1844.

[5] W. Martini, “Stirling Engine Design Manual”, NASA Report, National Technical Information Services, US Department of Commerce, Spring Field, USA, 1978.

[6] S.F. Kral, Dallas Hill, Jon Restivo and Joseph Johnson, “Test Results of an Orifice Pulse Tube Refrigerator,” Advances in Cryogenic Engineering, Vol.37 (B), Plenum Press, New York, 1992, pp. 931-937.

DC-DC Soft Switched Resonant Converter for Regulated Power Supply

Y. Sukhi[1] and Y. Jeyashree[2]

[1]Department of Electrical and Electronics Engineering, RMK Engineering College, Kavaraipettai - 601 206, Tamil Nadu

[2]Department of Control and Instrumentation, SRM University, Kattankulattur - 600 119, Tamil Nadu

E-mail: sukhirmk03@yahoo.com, jeyashree_christley@yahoo.co.in

(Received on 05 February 2009 and accepted on 22 June 2010)

Abstract

In this paper a pulse width modulated series parallel resonant converter is presented. The performance of the converter for constant output voltage with variable input and variable load is analyzed. This configuration is well suited for many applications where output is fairly constant but the input is required to vary widely without serious switching losses and with significant reduction in ripple content. Experimental results obtained from a laboratory prototype are presented.

Keywords: *DC-DC converter, Resonant converter, Soft switching, Zero current switching, Zero voltage switching*

1. INTRODUCTION

Switch mode power conversion is one of the elegant ways of electric power processing in today's industrial environment, due to circuit simplicity, ease of control, and improved efficiency. The recent trend in switch mode conversion is to increase the power density and to reduce the size of energy storage components, which requires operation at high switching frequencies. There are fundamentally two different circuit schemes of electronic power processing technology. They are pulse width modulation (PWM), and resonance. In all pulse width modulated DC to DC and DC to AC converters, the controllable switches are operated in a switch mode where they are required to turn on and turn off the entire load current during each switching in this switched mode operation, the switches are subjected to high switching stresses and high switching power losses, that increase linearly with the switching frequency of PWM [1]. Another significant draw back of switch mode operation is the EMI produced by large di/dt and dv/dt caused by switched mode operation [2].

The series parallel resonant converter is a preferred topology for dc-dc power conversion.Its main attractive features are zero voltage turn on switching (ZVS), constant switching frequency and simple control similar to that of hard switched full bridge PWM converter [3]. Resonant dc-dc converters are particularly used where high switching frequency are needed to minimize reactive component size since by operating the converters above the resonant tank natural frequency, lossless switching conditions may be achieved [4]. The series parallel converter is a particularly attractive topology since it combines a wide operating range with modest component rating. Operation of resonant converter above resonance (lagging power factor mode) results in a number of advantages. They are elimination of di/dt inductors and lossy snubbers, use of slow recovery diodes internal to MOSFET's reduced size of magnetic components etc [5]. The major limitation of high peak reverse voltage developed across the devices can be overcome by incorporating anti parallel diodes across each diode. The inverse diode associated with the device is sufficient to operate the circuit at hundreds of kilohertz, which allows to a use a diode having low turn off time. The frequency of operation is chosen to obtain the desired power handling capacity [6].

2. ANALYSIS OF SERIES PARALLEL RESONANT CONVERTER

2.1 Circuit Description

The basis circuit diagram of resonant converter is shown in Figure1. S_1 - S_4 are switching devices having base turnoff capability. D_1 to D_4 are anti parallel diodes across the switching devices. This can also be the internal diode of MOSFET. If they have slow recovery characteristics, external fast recovery diodes have to be used. The MOSFET (say S_1) and its anti parallel diodes (say D_1) acts as a bidirectional switch. Ls, Cs, Cp are resonant series inductor, series resonant capacitor, and parallel resonant capacitor respectively. In this circuit to make use of leakage inductance of high frequency transformer, the parallel resonant capacitor placed on the secondary of the transformer. The output voltage V_{AB} of High Frequency Inverter Bridge is applied to the tank circuit.

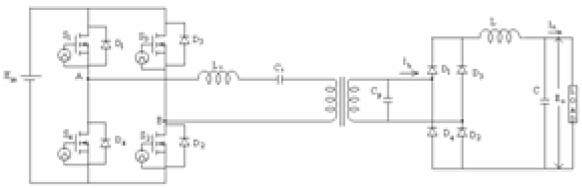

Fig.1 Basic circuit diagram of series parallel resonant converter

The diodes used in high frequency bridge rectifier should have fast recovery characteristics. LC comprises a low pass filter for smoother output voltage and current and a load is connected across the filter output.

2.2 Circuit Modeling

The load current I_0 is considered constant since a large inductor is assumed at the output circuit. Consequently the current to the input bridge rectifier I_b (t) has constant amplitude $+I_0$ or $-I_0$ depending on whether the voltage V_{cp} (t) is +ve or -ve respectively. Hence the output circuit can be represented as constant current sink qI_0, where q=+1 when V_{cp} (t) is =+ otherwise q= -1.

The switching frequency is constant and power control is obtained by phase shifting the gating signals to vary the pulse widthδ. The converter is designed to operate from maximum to minimum pulse width. When the controllable switches are switched on in its sequence, a square wave voltage is impressed across the terminal AB. The phase angleΦ between the gating signals is controlled to regulate the load voltage with variation with the load current or the input supply voltage. As the load current decreases to regulate output voltage the pulse width is decreased by phase shifting the gating signalsG_2 and G_4 respectively with respect to G_1 and G_3 as shown in Figure 2. It must be noted that gating signal G_1 and G_3 (also G_2 and G_4) are always 180° out of phase. The voltage across the terminals A and B, V_{AB} depends upon the switching status of the switches. When the gating signal G_1 is present then V_{AB} (t) = $+E_{in}$ if G_2 also present, otherwise=0.Similarly V_{AB} (t) = $-E_{in}$ or 0 depending on switching status of G_3 and G_4.

The equivalent reactance across the terminal AB may be capacitive or inductive. If it is capacitive, thyristors may be used and the converter then operates below resonant frequency. The lagging power factor mode, which occurs when the effective reactance is inductive, then the switches, is capable of gate or base turnoff may be used.

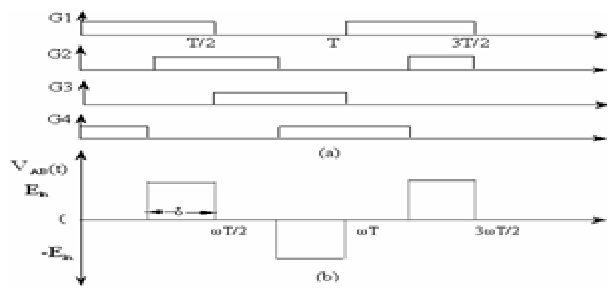

Fig.2 (a) Gatting signals (b) V_{AB} (t)

3. MODES OF SERIES-PARALLEL RESONANT CONVERTER

The principle of resonant converter can be explained with its different operating modes. The resonant converter can operate in five different modes. However the broad classification of modes can be made depending on the duty ratio. When the duty ratio is 1, the resonant converter can operate in two modes. The other modes are obtained when duty ratio is less than 1, depending upon the frequency of operation, circuit impedance across terminal AB and pulse width. When pulse width is maximum (Duty ratio D=1) the resonant converter can operate in two different modes.

3.1 Operation of Circuit in Mode 1

As explained the mode 1 results when the duty ratio is 1, with the condition that equivalent circuit impedance across AB is capacitive. The inductor current i (t) lead the voltage applied to the tank thus converter operates in leading power factor mode. Figure 3 shows typical Waveforms for this mode of operation. The switches S_1 & S_2 are turned on at t=0. The tank voltage becomes + E_{in} immediately. When the resonant current reaches zero at t = t_2, S_1 & S_2 are naturally commutated. Therefore zero current turn off is realized. As the resonant current reverses at t = t_2, with the tank connected to + E_{in}, D_1 & D_2 turn on allowing a part of the tank energy to return to the source during the time interval t_2 - t_3. At the instant $t = t_3$, switches S_3 & S_4 are turned on and V_{AB} changes from $+E_{in}$ to $-E_{in}$. At $t = t_5$ when i(t) becomes zero and begins to reverse forcing the diodes D_3 & D_4 to conduct. The interval t_2 - t_3 & t_5 & t_6 are called regenerative interval (RI) and the intervals t_0 - t_2 and t_3 -t_5 are called power intervals. Thus in this mode there are two RI & two PI.

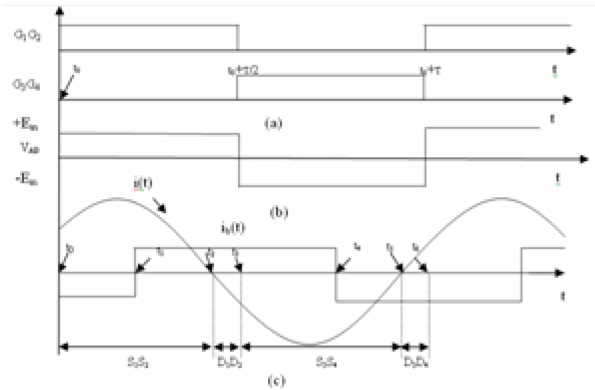

Fig.3 Typical waveform in mode-1(a) Gating Signal (b) V_{AB} (t) (c) i (t) and i_b(t)

As the switches are on at a finite current and at finite voltages, this results in turn on switching power loss. If the diodes have slow recovery characteristics, at $t = t_0$ large reverse current may flow through D_3 S_1 & D_4 S_2. In order to avoid these current and to minimize the diode turn off losses, the freewheeling diodes should have fast recovery characteristics. It is also evident that mode 1 requires lossy snubber & di/dt limiting inductors.

3.2 Operations of Circuit in Mode 2

Mode 2 also occurs at duty ratio of 1. However equivalent reactance across AB is inductive. In this mode switching frequency is more than series resonant frequency and equivalent reactance is inductive across the terminal AB. The converter operates at lagging power factor (above resonance) mode. Figure 4 shows typical waveforms for this mode of operation. It is evident from the figure that diodes D_1 & D_2 are conducting initially at $t = t_0$. When the current through the diode reaches zero at time $t = t_1$, switches S_1 & S_2 are tuned on and the currents is transferred from the anti-parallel diodes. The converter operates in the power interval till $t = t_3$. There is no voltage across the switches at turn on (since D_1 & D_2 are conducting) which eliminates turn on losses and facilitates operation of switches with loss less snubbers. At time $t = t_3$, the transition from power interval to regenerative interval takes place. At time $t = t_3$ i.e. (t_0 + T/2) when switches S_1 & S_2 are turned off, the current is transformed to D_3 & D_4 Turn off losses are present in such type of operation because during turn off, current and voltage are simultaneously present at the switch. The sequence of events repeats in the next half cycle. Interval t_0-t_1 & t_3-t_4 are called regenerative interval and t_1-t_3 & t_4-t_5 are power interval

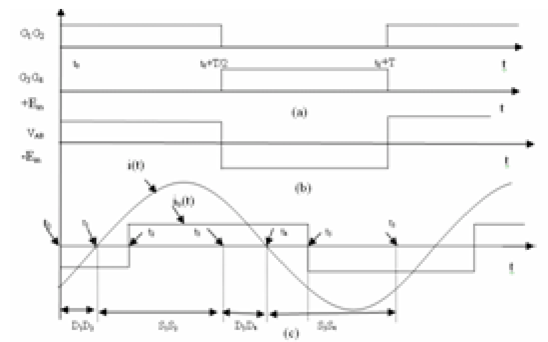

Fig. 4 Typical waveform in mode - 2(a) Gating Signal (b) V_{AB} (t) (c) i (t) and i_b(t)

4. MATHEMATICAL ANALYSIS Of CONVERTER

Figure 5 shows the A.C. equivalent circuit of series parallel resonant converter. The following assumptions are used in the mathematical analysis of the series - parallel resonant converter.

i The switches, diodes, inductors, capacitors and snubber components used are ideal.
ii The effects of snubber are neglected.
iii The filter inductance is large enough to keep the load current constant.
iv The high frequency transformer is ideal and has unity turns ratio.

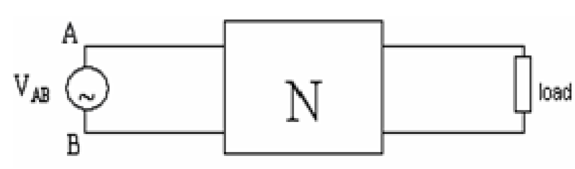

Fig.5 .A.C Equivalent circuit of resonant converter

Where N - is the resonant network
R_{ac} - AC equivalent load resistance
V_{AB} - RMS fundamental component of V_{AB}

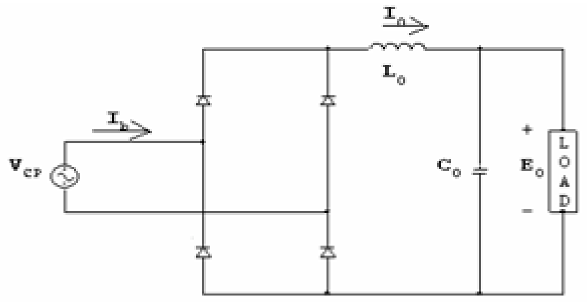

Fig.6 Output circuit of bridge rectifier and filter component to resonant converter

From the output circuit of bridge rectifier and filter component to resonant converter Figure 6, V_{cp} and I_b represent the rms fundamental component of V_{cp} (t) and I_b (t) respectively. The output circuit consists of the diode bridge rectifier and inductive filter present in the output circuit.

The D.C. output voltage is obtained as the average of A.C. input voltage, V_{cp}

(1)

$$E_0 = \frac{2\sqrt{2}}{\pi} V_{cp} \tag{2}$$

ω = 2πϕ and f is the switching frequency.

The fundamental component of Diode Bridge current is calculated using Fourier analysis as

$$I_b = \frac{1}{\pi} \int_0^{2\pi} i_b(t) \sin \omega t d(\omega t) \tag{3}$$

$$I_b = \frac{2\sqrt{2}}{\pi} I_0 \tag{4}$$

Using Equation (2) & (4) the equivalent A.C. resistance as seen at the input of the rectifier bridge is given by

$$R_{ac} = \frac{V_{cp}}{I_b} = \frac{\pi^2}{8} R_L \tag{5}$$

δ and D are related by

$$\delta = \pi D \tag{6}$$

The duty ratio D is defined as the ratio of the time duration for which the switch S_1 & S_2 or S_3 & S_4 are switched on simultaneously i.e. ton to the half of the switching period (T/2) i.e., D = t_{on}/ (T/2).When the switches S1 and S2 (S3 or S4) are switched on simultaneously, the voltage across A and B is the input voltage E_{in}.

The R.M.S. fundamental Voltage across A and B is given by

$$V_{AB} = \frac{1}{\sqrt{2}\pi} \int_0^{2\pi} V_{AB}(t) \sin \omega t d(\omega t) \tag{7}$$

$$V_{AB} = \frac{1}{\sqrt{2}\pi} \left[\int_{(\pi-\delta)/2}^{(\pi+\delta)/2} E_{in} \sin \omega t d(\omega t) - \int_{(3\pi-\delta)/2}^{(3\pi+\delta)/2} E_{in} \sin \omega t d(\omega t) \right] \tag{8}$$

$$V_{AB} = \frac{2\sqrt{2} E_{in} \sin \delta / 2}{\pi} \tag{9}$$

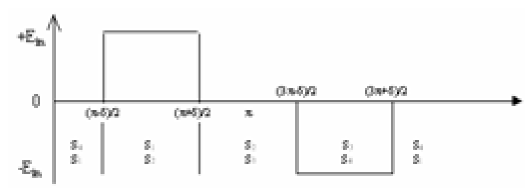

Fig.7 Quasi - square voltage waveform of resonant converter

E

The equivalent circuit of the converter across the terminal A and B shown in Figure 5 is replaced by its equivalent circuit shown in Figure 8. In order to simplify the presentation, all the equations are normalized using the following base quantities.

Base voltage = E_{in}
Base impedance = $\omega_0 L$
Base current = E_{in} / $\omega_0 L$
Base frequency ω_0 = 1/ √LC

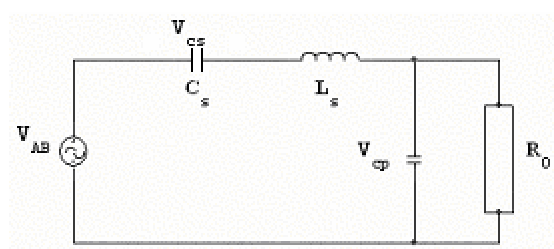

Fig.8 AC Equivalent circuit of resonant converter

The RMS fundamental voltage across the parallel capacitor C_p is given by

$$V_{cp} = \left[\frac{V_{AB}}{j(X_L - X_{cs}) + \dfrac{1}{\dfrac{1}{R_{ac}} - \dfrac{1}{jX_{cp}}}}\right] \times \left(\frac{1}{\dfrac{1}{R_{ac}} - \dfrac{1}{jX_{cp}}}\right) \quad (10)$$

Here
$X_L = \omega L$, $X_{cs} = 1/\omega C_s$, $X_{cp} = 1/\omega_{cp}$ (11)

Substituting the eqn (11) in eqn (10), the equation becomes

$$V_{cp} = \frac{V_{AB}}{1 + \dfrac{C_P}{C_S} - \omega^2 LC_P + j\dfrac{8}{\pi^2}} \times \frac{\omega L}{R_L} - \frac{1}{\omega C_S R_L} \quad (12)$$

Substituting the eqn (9) in eqn (12) and after simplification, the equation becomes

$$V_{cp} = \frac{2\sqrt{2}E_{in}\sin\delta/2}{\pi \times \left[\left(\dfrac{m+1}{m}\right)(1-y^2) + \dfrac{8}{\pi^2}jQ\left(y - \dfrac{1}{(m+1)y}\right)\right]} \quad (13)$$

where
$m = C_s / C_p$, $Q = \omega_0 L / R_L = 1/\omega_0 C R_L$, $y = \omega/\omega_0$ (14)

Substituting eqn (13) in eqn (2) and afternormalization, the equation becomes

$$\frac{E_0}{E_i} = \frac{\sin\delta/2}{\dfrac{\pi^2}{8}\left(\dfrac{m+1}{m}\right)(1-y^2) + jQ\left(y - \dfrac{1}{(m+1)y}\right)} \quad (15)$$

The equivalent impedance across the terminals A and B is given by

$$Z_{eq} = j(X_L - X_{CS}) + \frac{1}{\dfrac{1}{R_{ac}} - \dfrac{1}{jX_{CP}}} \quad (16)$$

Substituting eqn(5), eqn(11) in eqn(14), the equation becomes

$$Z_{eq} = \left[j\left(\frac{\omega L}{R_L} - \frac{1}{\omega C_S R_L}\right) + \frac{1}{\dfrac{8}{\pi^2} + j\omega C_P R_L}\right] \quad (17)$$

Using eqn(11) in eqn(17) and after simplification, the equation becomes

$$Z_{eq} = \left[jR_L Q\left(y - \frac{1}{(m+1)y}\right) + \frac{1}{\dfrac{8}{\pi^2} + j\dfrac{y(m+1)}{Qm}}\right] \quad (18)$$

After simplification and rearranging the terms we get

$$Z_{eq} = \omega_0 L \frac{B_1 + jB_2}{B_3} \quad (19)$$

Where $B_1 = \dfrac{8Q}{\pi^2}\left[\dfrac{m}{y(m+1)}\right]^2$ (20)

$$B_2 = \left[y - \frac{1}{y(m+1)}\right]B_3 - \frac{m}{y(m+1)} \quad (21)$$

$$B_3 = 1 + \left[\frac{8Qm}{\pi^2 y(m+1)}\right] \quad (22)$$

Normalizing eqn (19), the equation becomes

$$Z_{eqpu} = \frac{B_1 + jB_2}{B_3} = |Z_{eqpu}|e^{j\Psi} \quad (23)$$

$$|Z_{eqpu}| = \frac{\sqrt{B_1^2 + B_2^2}}{B_3^2} \quad (24)$$

Impedance angle $\Psi = \tan^{-1}\dfrac{B_1}{B_2}$ (25)

The resonant link current I

$$I = \frac{V_{AB}}{Z_{equ}} \quad (26)$$

$$I = |I|\angle - \psi \quad (27)$$

where

$$|I| = \frac{V_{AB}}{|Z_{equ}|} \quad (28)$$

Substituting eqn (9) in eqn (4) and after normalization, the equation becomes

$$|I|_{pu} = \frac{2\sqrt{2}\sin\frac{\delta}{2}}{\pi|Z_{equ}|} \quad (29)$$

Peak Inductor is given by

$$|I|_{ppu} = \sqrt{2}|I|_{ppu} = \frac{4\sin\frac{\delta}{2}}{\pi|Z_{equ}|} \quad (30)$$

$$|V_{cs}|_{ppu} = |I|\frac{X_{cs}}{\omega_0 L} \quad (31)$$

Using (30) Peak Voltage across C_s is calculated as

$$|V_{cs}|_{ppu} = \frac{|I|_{ppu}}{y(m+1)} \quad (32)$$

The peak Voltage across C_p is obtained using eqn (1) and rearranging the terms.

$$|V_{cp}|_{ppu} = \frac{\pi}{2}\left|\frac{E_O}{E_{in}}\right| \quad (33)$$

The load ripple voltage is given by,

$$V_{ac} = \left[V_{crms}^2 - V_c^2\right]^{1/2} \quad (34)$$

V_{crms} is the total rms load voltage
V_o is the average load voltage
The Voltage ripple factor, which is a measure of the ripple content, is given by the equation

$$RF = \frac{V_{ac}}{V_c} \quad (35)$$

Similarly the Voltage ripple factor using the filter elements is given by the equation

$$RippleFactor = \frac{V_{2rms}}{V_c} \quad (36)$$

where V_{2rms} represents the rms value of the second harmonic component.

$$V_{2rms} = \frac{V_m}{3\sqrt{2}\pi\omega^2 LC} \quad (37)$$

where V_m represents the maximum value of voltage after rectification. The efficiency of the converter is calculated using the expression

$$\%\eta = \frac{P_{out}}{P_{in}} \times 100 \quad (38)$$

5. PERFORMANCE CHARACTERISTICS

In designing the full bridge series-parallel resonant converter, the given data would be the input and output voltage, output current and possibly the desired switching frequency. All other parameters of the converter need to be determined. The variables which are most important from the design point of view are normalized converter gain (E_0/E_{in}), normalized switching frequencies (y), peak inductor current (i_{LS}), peak series capacitor voltage (V_{cs}), peak parallel capacitor voltage (V_{cp}) etc, because they provide information to determine the component ratings. Since the graphs give more useful information than equations in understanding and designing a system, the analysis is used to obtain the design curves.

5.1 Variation of Converter Gain (E_o/E_{in}) Vs Normalized Switching Frequency (y)

A set of characteristics have been plotted showing the variation of normalized switching frequency against voltage gain (E_0/E_{in}) with Q as a parameter using eqn.15. Figure 9 shows such characteristic curves in which the curves have been plotted for various values of Q from 1 to 6 for m=Cs/cp=1.The curves show that normalized converter gain for a given Q increases, reaches a maximum and then decreases as the normalized switching frequency increases from 0.3 to 1.5. At higher values of Q, the normalized gain is maximum near the series resonant frequency $\omega_o = 1 / \sqrt{L_s C_s}$, Cs = $\omega_o/(m+1)^{1/2}$ i.e. at normalized switching y = 0. 707. This leads to information that the load resistance is sufficiently small for high values of Q to shunt the parallel capacitor and nullify its effect on the performance.

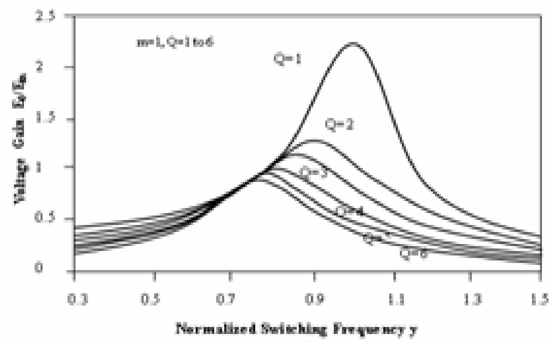

Fig.9 Variation of voltage gain versus normalized switching frequency for various values of Q with m = 1

At lower values of Q, the peak of curves occurs at the frequency more than series resonant frequency. At light load, Q decreases and the effect of Cp comes in to play and as a result resonant peak moves towards higher frequency. This is because the equivalent capacitance is given by parallel combination of C_s & C_p. At sufficient light load or no load the resonant peak occurs at $f_0=1/2\pi(LCsCp/ (Cs+Cp))^{1/2}$ i.e. at normalized switching frequency y = 1.0.

5.2 Variation of Peak Parallel Capacitor Voltage Vs Normalized Switching Frequency

The variation of peak parallel capacitor voltage with change in normalized switching frequency using eqn (13) is shown in Figure10. It is seen that peak parallel capacitor voltage increases with decrease in value of Q for a given frequency y and this increase is large in case of y is greater than 0.8. The frequency of operation increases up to y=1, then at that frequency, peak capacitor voltage decreases at full load but at light load it increases and this increase is much higher.

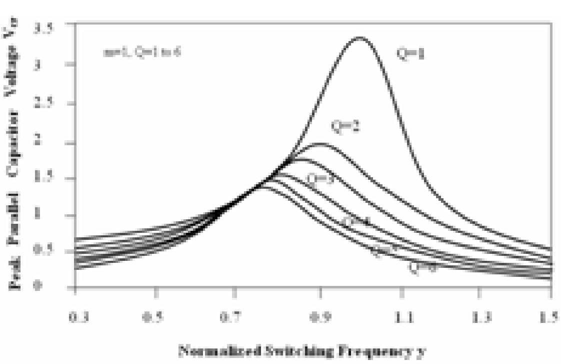

Fig.10 Variation of peak parallel capacitor voltage versus normalized switching frequency for various values of with m = 1

Therefore this point should be taken care while designing the converter. It is observed that the peak parallel capacitor voltage for all values of Q is same at about .707pu frequency giving the peak parallel capacitor voltage of 1.4pu.

5.3 Variation of Peak Series Capacitor Voltage Vs Normalized Switching Frequency

It is observed from Figure 11 which shows the variation of peak series capacitor voltage with normalized switching frequency for different values of Q, that peak series capacitor voltage increases and attains a peak and then decreases as normalized frequency increases for a given value of Q using the eqn.26.

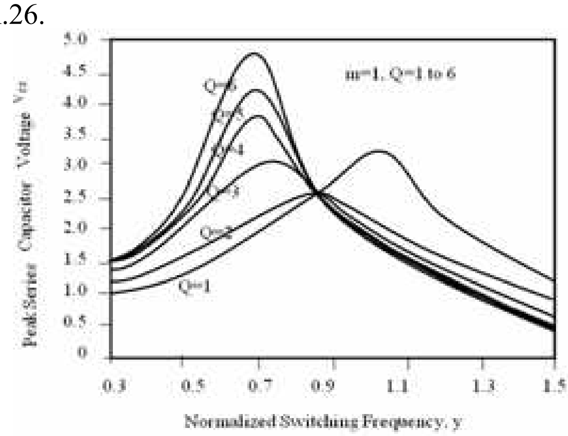

Fig.11 Variation of peak series capacitor voltage versus normalized switching frequency for various values of Q with m = 1

These peak values get shifted to relatively higher frequency as Q decreases. An important point is that except Q = 1 maximum value of peak series capacitor voltage decreases as Q decreases and its value is same for all values of Q when per unit frequency is .88pu.

5.4 Variation of Peak Inductor Current Vs Normalized Switching Frequency

Eqn.30 shows that peak inductor current is a function of Q and y. Figure 12 shows that peak inductor current increases with increase in Q, since the output voltage decreases for the same output power. But for a given value of y, it can be seen peak current decreases as load current increases with increase in value of Q.

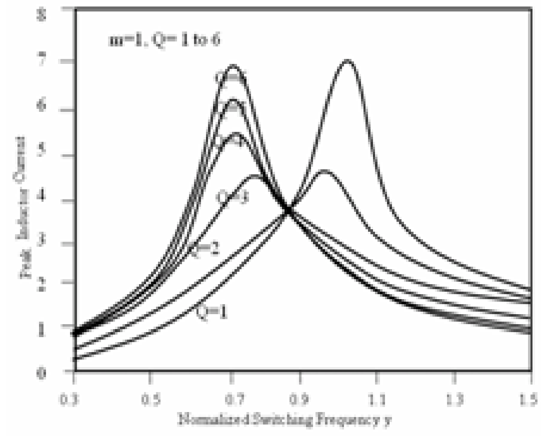

Fig.12 Variation of peak inductor current versus normalized switching frequency for various values of Q with m = 1

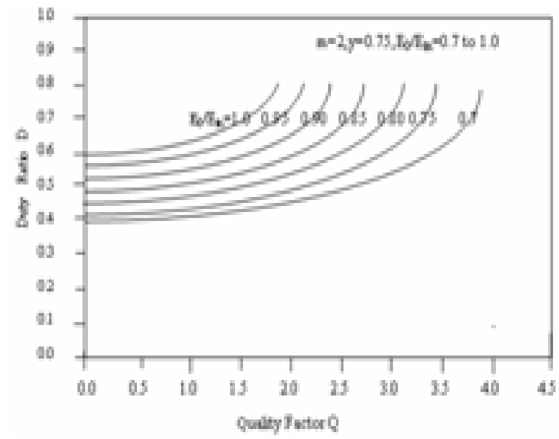

Fig.14 Variation of duty ratio versus quality factor with m = 2, y= 0.75

5.5 Variation of Duty Ratio Vs Q

In this section the qualitative analysis of the relationship between duty ratio and quality factor Q is made. Figure 13 and Figure 14 show how the duty ratio D has to be varied as Q changes, to keep output load voltage constant at particular value. These curves are obtained by solving eqn.(15) numerically for duty ratio as a function of Q for various values of converter gain E_o/E_{in} (for .7 to 1.0) and switching frequency (yield stress = 0.75 to 9). It is observed that as the E_o/E_{in} decreases, the duty ratio versus Q curves shifts downwards. The increase in value of yield stress results in shrinkage of D vs. Q curve ranges.

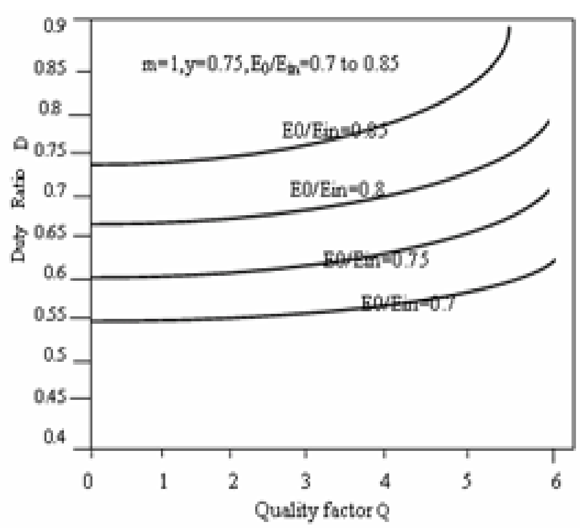

Fig.13 Variation of duty ratio versus quality factor with m = 1, y = 0.75

5.6 Variation of Converter Gain (E_o/E_{in}) Vs Normalized Switching Frequency (Y)

A set of characteristics have been plotted showing the variation of normalized switching frequency with Q as a parameter using eqn.15. Figure 14 shows one such that in which the curves have been plotted for various values of Q from 1 to 6 for m=Cs/cp=1.The curves show that normalized converter gain for a given Q increases first, reaches a maximum and then decreases as normalized switching frequency increased from .3 to 1.5.

For higher values of Q, the normalized gain is maximum near the series resonant frequency = $1 / (L_sC_s)^{½}$, Cs = $\omega_o/(m+1)^{½}$ i.e. at normalized switching y = 0. 707. At lower values of Q, the peak of curves occurs at the frequency more than series resonant frequency i.e. load resistance is sufficiently small for high values of Q to shunt the parallel capacitor and nullify its effect on the performance.

At light load, Q decreases and the effect of Cp comes in to play and as a result resonant peak moves towards higher frequency. This is because the equivalent capacitance is given by parallel combination of C_s & C_p.

At sufficient light load or no load the resonant peak occurs at f= $1/2\pi$ (CsCp/Cs+Cp)½ i.e. at normalized switching frequency y = 1.0.

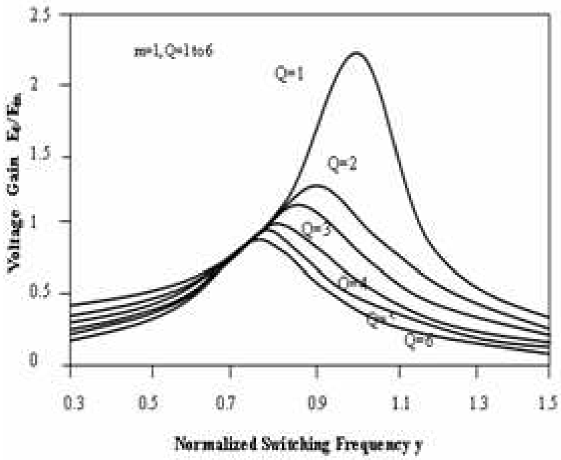

Fig.14 Variation of voltage gain versus normalized switching frequency for various values of Q

6. DESIGN OF SERIES PARALLEL RESONANT CONVERTER

6.1 Selection of Normalized Switching Frequency

The output voltage is regulated at all loads by proper selection of y. In Figure 13 for y = 0.75 the output voltage can be regulated at E_o/E_{in} = 0.8 for the variation in Q up to 6. But as y increases further, the range of Q up to which the converter can be regulated decreases. This implies that too high value of y cannot be chosen especially when wide load variations are expected. Besides y should not be of low value. Otherwise operation above resonance may not possible. Keeping these two factors in mind, y = 0.8 have been chosen.

6.2 Selection of Tank Circuit Q at Full Load

Size of tank depends upon the value of quality factor Q and it should not be large. Eqn(19),eqn (20),eqn(21) ,eqn (22) and eqn(30) shows that peak inductor current is a function of Q and y. Figure 12 shows that peak inductor current increases with increase in Q, since the output voltage decreases for the same output power. But for a given value of y, it can be seen that the peak inductor current decreases as load current increases with increase in value of Q. However this decrease is not drastic for values of Q greater than 5. A compromised value of Q = 5 is chosen in this design.

6.3 Selection of Normalized Converter Gain

It is clear from the circuit topology that output current is rectified and averaged tank current reflected to the secondary side of the transformer. Since the tank current is directly related to the output current, therefore we should choose a large conversion ratio, so that the turns ratio is minimized, resulting in the smallest possible tank current on the primary for a specified output current on the secondary. Hence the conversion ratio should be chosen close to one. Based on above consideration, the following optimum values are selected in the design of the converter.

Normalized frequency y = 0.8.
Cs/Cp ratio m = 1
Q of tank circuit at full load = 5

$$\left|\frac{E_0}{E_{in}}\right| = 0.8$$

Design

Input voltage E_{in} = 30 volts
Output voltage E_o =24 volts
Output Current = 1.5 Amps
Switching frequency = 50 kHz
$m=C_s/C_p$ = 1, Q=5, y=0.8
Load resistance $R=V_0/I_0=16\Omega$

$$R = \frac{\omega_0 L}{Q} = \frac{1}{Q} \times \sqrt{\frac{L}{C}}$$

$$\sqrt{\frac{L}{C}} = Q \times R = 5 \times 16 = 80$$

Resonant frequency f_o is given by

$$f_o = f/y = 50{,}000/0.8 = 62.5 \text{ kHz}$$

But

$$f_0 = \frac{1}{2\pi\sqrt{LC}}$$

$$\frac{1}{\sqrt{LC}} = 2\pi \times 62.5 \times 10^3$$

The values of L & C are L = 204μH and C = 0.0318 μF

Since Cs = Cp,Cs = Cp = 2C = 0.0636μF

If Cs = Cp =0.047μF is selected for the purpose of standard available capacitance then L=261mH.

7. EXPERIMENTAL RESULTS

Some testing results are presented in this section to verify the theoretical predictions of previous sections. An experimental prototype has been implemented for a resistive load as shown in Figure 15. The load rating is

24V, 36W. The resonant inductor is 0.261mH and the inductor is wound around ferrite core and the series resonant capacitor is 0.47μF and the capacitor used is of polypropylene film type.

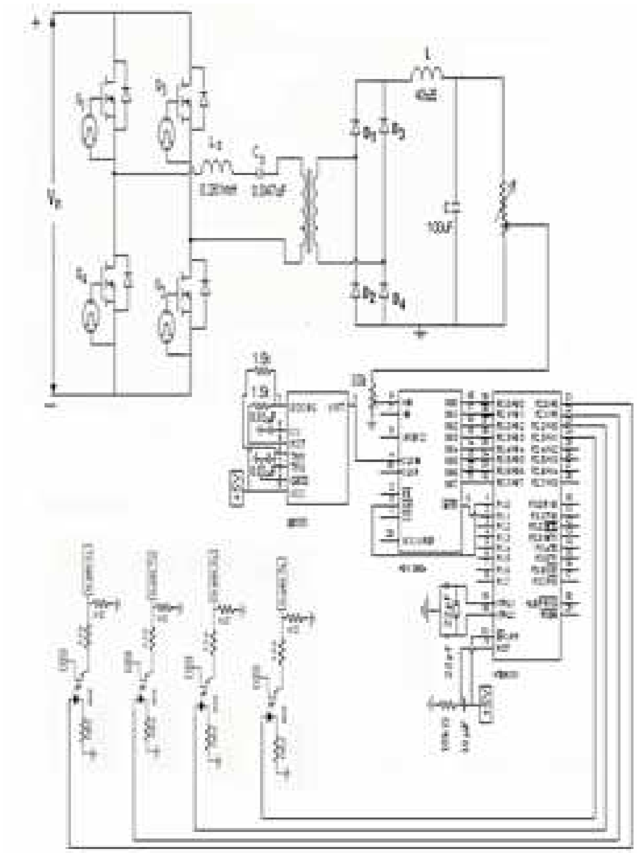

Fig.15 Experimental circuit

The switching frequency is 50KHz.All the four switches used is of IRF460 with an external fast recovery diode BYE26E connected across each switching device. In the secondary side, the diodes used for rectification are FR306.The filter inductor is 40μH and is wound around ferrite core. The filter capacitance is 100μF, 63V and the capacitor used is of electrolytic type.Figure 16 to Figure 18 shows the experimental output obtained. In each figure,(a) shows the voltage across the series capacitor and (b) shows the output voltage across the load after connecting the filter elements.

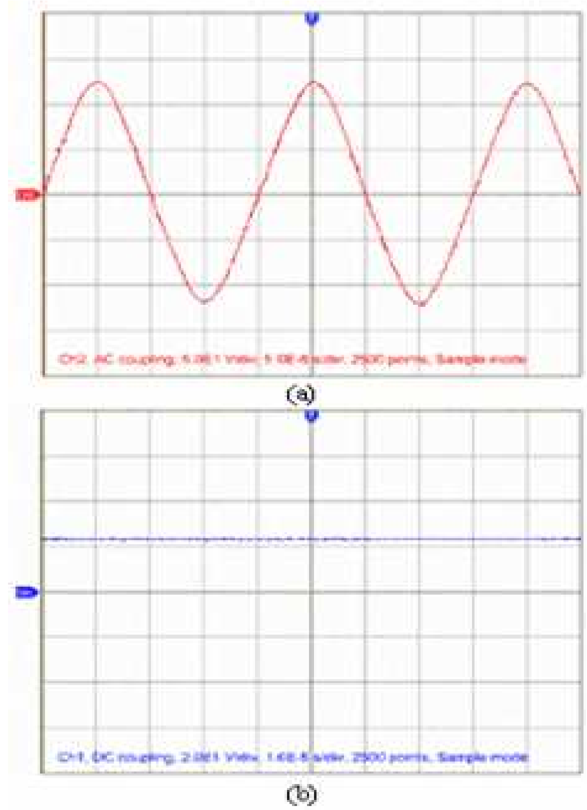

Fig.11 Experimental results for series parallel resonant converter at full load with m=1: (a) V_{cs}, (b) V_0 with filter

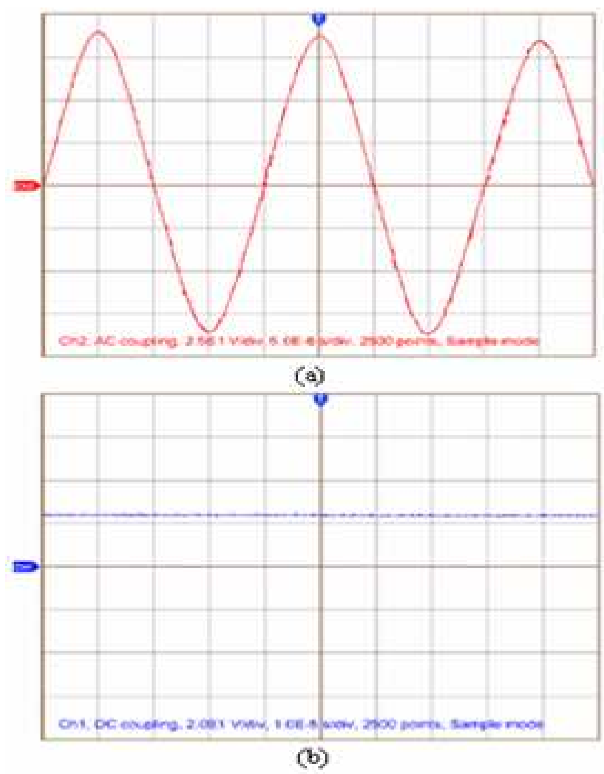

Fig.12 Experimental results for series parallel resonant converter at 70% load with m=1: (a) Vcs, (b) V0 with filter

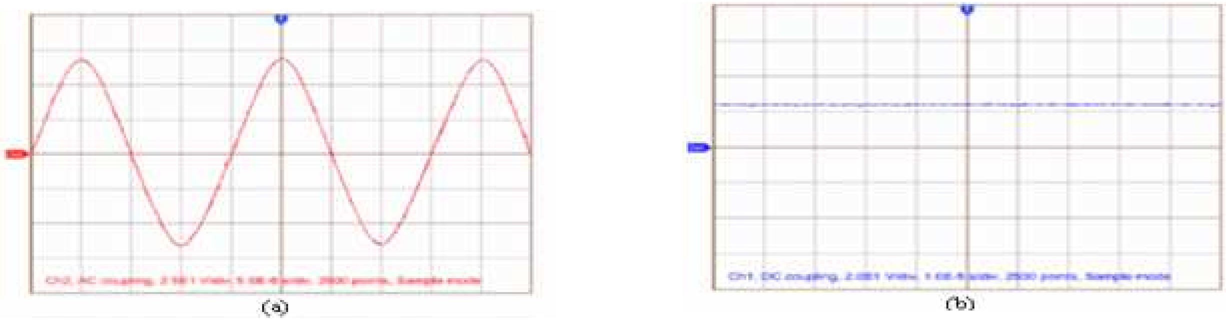

Fig.13 Experimental results for series parallel resonant converter at 40% load with m=1: (a) V_{cs}, (b) V_0 with filter

Table 1&2 gives the Comparison of Results between Calculated and experimental results respectively of Series Parallel Resonant Converter for a input D-C supply Voltage of 30V and Switching Frequency of 50 kHz.

Table 1 Calculated results

Load %	Duty Ratio D	Series Capacitor Voltage Vcp (peak) Volts	Series Inductor Voltage Vcs (peak) Volts	Output Current I_0 amps	Output Voltage V_o Volts	Ripple Factor Without Filter %	Ripple Factor With Filter %
100	0.9	116.6	149.7	1.5	24	20.2	0.0055
90	0.86	104.85	134.2	1.35	24	19.8	0.0047
80	0.79	93.2	117.5	1.2	24	18.9	0.0036
70	0.72	81.55	104.4	1.05	24	17.5	0.0024
60	0.63	69.9	89.5	0.9	24	16.9	0.0017
40	0.45	58.25	59.6	0.6	24	15.3	0.0008

Table 2 Experimental Results

Load %	Duty Ratio D	Series Capacitor Voltage Vcp (peak) Volts	Series Inductor Voltage Vcs (peak) Volts	Output Current I_0 amps	Output Voltage V_o Volts	Ripple Factor Without Filter %	Ripple Factor With Filter %
100	0.92	126.6	166.1	1.5	24	21.8	0.0065
90	0.88	115.6	145.5	1.35	24	20.9	0.0056
80	0.8	102.3	132.1	1.2	24	19.6	0.0048
70	0.73	92.9	118.1	1.05	24	18.5	0.0035
60	0.63	76.5	105.2	0.9	24	17.2	0.0025
40	0.44	64.4	84.6	0.6	24	16.4	0.0012

Table 3 Efficiency Obtained with Conventional Method for Variable I/P D-C Supply Voltage and Switching Frequency = 50 kHz

Duty Ratio	Input Current (amps)	Input Voltage (Volts)	Output Current (amps)	Output Voltage (Volts)	Efficiency %
1	1.63	30	1.5	26.94	82.65
1	1.49	30	1.35	27.28	82.29
1	1.35	30	1.2	27.53	81.76
1	1.19	30	1.05	27.86	81.53
1	1.04	30	0.9	28.17	81.14
1	0.88	30	0.75	28.34	80.67

Table 4 Efficiency obtained for Series Parallel Resonant Converter for I/P D-C supply Voltage = 30 V and Switching Frequency = 50 kHz

Duty Ratio	Input Current (amps)	Input Voltage (Volts)	Output Current (amps)	Output Voltage (Volts)	Efficiency %
1	1.81	30	1.5	33.27	91.9
1	1.65	30	1.35	33.65	91.77
1	1.49	30	1.2	33.81	90.74
1	1.33	30	1.05	34.02	89.74
1	1.17	30	0.9	34.71	89
1	1.02	30	0.75	35.64	87.42

8. CONCLUSION

A new high frequency regulation method for a DC-DC converter is presented that permits the implementation of a voltage control strategy Regulation is achieved by varying the conduction angle of the switching devices. The switches are operated under zero current conditions and therefore results in much higher efficiency and reduced voltage stresses. The regulation principle is general and can be implemented in any kind of converter without modifying its operation. Based on the converter analysis, characteristic curves have been obtained and a step by step design procedure of the converter has been given. The proposed method is having better efficiency than the conventional method. Results obtained from the prototype verifies the feasibility and the advantages of the topology.

REFERENCES

[1] A.K.S. Bhat and S.B. Dewan, “Analysis & Design of a high frequency resonant converter using LCC Type Communtation”, IEEE Trans. on Power Electronics Vol.2, Oct.1987, pp.291 - 301.

[2] A.K.S. Bhat, “Analysis & Design of Series Parallel Resonant Converter”, IEEE Transaction on PE Vol.8, No.1, Jan.1993, pp.174-182,

[3] AndrewJ.Foryth, Gillian A .Ward and StefanV Mollow” Extended Fundamental Frequency Analysis of the LCC Resonant Converter” IEEE Transactions on PE Vol.8, No.6, Nov 2003, pp.1286-1292.

[4] Fang.Z.Peng, Hui Li,Gui -Jia Su and Jack.S.Lawler “A New ZVS bidirectional DC-DC Converter for Fuelcell and Battery Applications” IEEE Transactions on PEVol9 No.1, Jan 2004, pp.54-64.

[5] Nikhil Jain, Praveen K.Jain and Geza Joos”A Zero Voltage Transtition Boost Converter Employing a Soft Switching Auxiliary Circuit with Reduced Conduction Losses” IEEE Transactions on PE Vol.9, No.1, Jan 2004, pp.130-139.

[6] Brendan Peter McGrath, Donald Grahame Holmes, Patrick John McGoldrick and Andrew Douglas McIver, “Design of a Soft-Switched 6kW Battery Charger for Traction Applications”, IEEE Transactions on PE Vol.22, No.4, July 2007, pp.1136-1144.

Modeling and Analysis of Low-Cost Four-Switch Three-Phase Inverter-Fed Induction Motor Drive

K. Srinivasan[1] and S.S. Dash[2]
[1]Sathyabama University, Chennai - 600 119, Tamil Nadu
[2]Department of Electrical and Electronics Engineering, S.R.M. University, Chennai - 603 203, Tamil Nadu
E-mail: omsrivas@yahoo.co.in,munu_dash_2k@yahoo.com
(Received on 06 June 2009 and accepted on 05 June 2010)

Abstract

In this paper a novel low-cost four-switch three-phase inverter-fed induction motor drive is presented. The proposed inverter employs only four switches and has the capability of delivering sinusoidal input current with unity power factor. This paper describes the feasibility and the operational limitations of the proposed structure. A mathematical model of the system is derived using generalized modulation theory and experimental results for steady state and dynamic behavior are presented to verify the developed model.

Keywords: *Generalized modulation theory, Induction motor drive*

1. INTRODUCTION

With the invention of high speed power semi conductor devices, three phase inverters play the key role for variable speed ac motor drives. In the past, researchers mainly concentrated on the development of efficient control algorithms for high performance variable speed drives. Conventional six switch three phase inverters involve the losses of the six switches as well as the complexity of the control algorithms and interface circuits to generate six PWM logic signals. However the cost, simplicity and flexibility of the overall drive system which become some of the most important factors did not get that much attention to the researchers. That‘s why, despite tremendous research in this area most of the developed control system failed to attract the industry.

Thus the main issue of this paper is to develop a simple and efficient high performance inverter for low power applications. Figure 1 shows a standard three-phase voltage source inverter utilizing three legs [Six-Switch Three-Phase voltage source Inverter (SSTPI)], with a pair of complementary power switches per phase. A reduced switch count voltage source inverter [Four Switch Three-Phase voltage source Inverter (FSTPI)] uses only two legs, with four switches. Several articles report on FSTPI structure [1&3], regarding inverter performance and switch control. The FSTPI structure generates four active vectors in the plane, instead of six, as generated by the SSTPI topology. Figure 2 shows a PWM inverter with four switches feeding two phases of an induction motor. The third phase of the machine is connected with the center tap of the dc voltage source. It is well known that a VSI-PWM inverter with capacitor DC link Figure 2 is regarded as one of the most important structure for a three phase to three phase power converter. The leakage inductance of the Induction motor is shown to emphasis the symmetric structure of the converter. This type of converter normally requires twelve switches for a rectifier and inverter composed of a self turn off switch such as a power transistor or IGBT with an anti parallel diode. Compared to a conventional thyrister converter, the distinguishing advantages of these structures are: (1). Capability of unity or even leading power factor, (2). Sinusoidal input current wave forms reducing harmonics pollution, (3).bidirectional power flow [4].

A number of low cost topologies have been suggested for fixed and variable speed drives in the low power range. A four switch inverter with the spilt capacitor in the dc link provides balanced three phase output to ac motor at adjustable voltage and frequency. An ac input is then connected to the PWM voltage of rectifier and the centre point of two split capacitor. A three phase ac motor is also connected to the output of the inverter and the same centre point.

In this proposed approach instead of conventional six switch three phase inverter, a Four switch three phase inverter is utilized. It reduces the cost of the inverter, switching loss and complexity of the control algorithm and interface circuit to generate 6 PWM logic signals [8]. A performance comparison of the proposed Four switch three phase inverter fed drive is also made in terms of Total Harmonic Distortion of the stator current and speed response [7]. In the literature survey [1] to [7] the harmonic analysis of four-switch three-phase voltage inverter fed induction motor is not presented. In this paper the simulation of a performance comparison of the Four Switch three phase inverter fed drive with a conventional six switch three phase inverter fed drive is made in terms of total harmonic distortion (THD) of the stator current and speed response.

This paper describes the feasibility and the operational limitations of the proposed converter. A mathematical model of the system has been derived using generalized modulation theory and the typical experimental results for steady state and dynamic responses are presented to illustrate important performances characteristics to verify the developed model.

2. CONFIGURATION OF PROPOSED SYSTEM

The proposed inverter consist of four switches and a capacitor dc link Figure 2. The centre point of split capacitor link forms the third phase both for the rectifier and inverter. The output inverter can be operated by voltage control. In case of voltage control the output line to line voltage,

$$V_{13} = V_{01} - V_{03} \qquad (1)$$

that is voltage of the output phase 1 with reference to of centre point of the split capacitor can be defined by controlling S01 and S02 in a PWM fashion . In order to balance three phase output voltage , the voltage V23should be shifted by +60or -60 according to the output phase sequences. One can see that the line to line voltage V 12 is a three level PWM between +V c1 , 0and –Vc2 . on the other hand the voltages V13and V23 are two level between +Vc1 and –Vc2 over the fundamental component in the three phase output voltage.

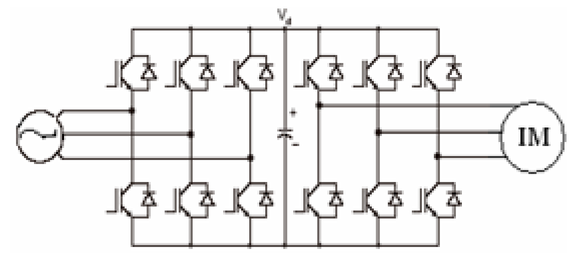

Fig.1. Conventional VSI- PWM Inverter system

The inverter operates in one of four non zero voltage vectors as shown in Figure 2 the voltage vector is defined by the following complex vector expression :

$$V = 2 / 3 \, (V_1 + aV_2 + a2V_3) \qquad (2)$$

Where $a = e^{-j2\pi/3}$

If balanced three phase sinusoidal waveforms are required, the voltage vector should be controlled in a circular manner. Therefore the maximum circular locus results in 0.866 compared to that of the conventional six switch inverter. A dc bus centre point is assumed to the ground reference. Each location corresponds to one switching state of the converter. The line to ground voltages are uniquely determines the PWM inverter switching according to the voltage controller. There is no zero voltage vector and one can expect that switching frequency of the proposed circuit will be somewhat higher then that of the six switch inverter , in which six non zero vector and two zero vector are available. Both of the dc link capacitor voltage must be higher than the peak value input and output line to line voltages for current controllability, respectively. Thus the overall dc link voltage of the proposed circuit must be twice as high as that of the six inverter.

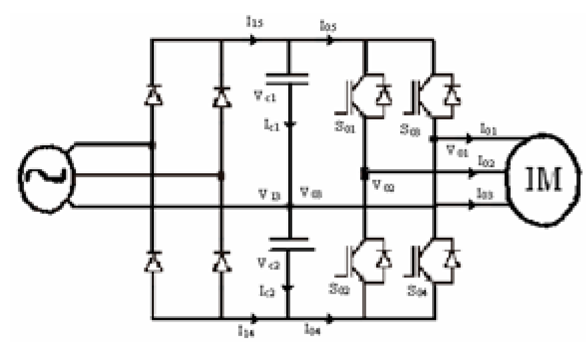

Fig.2 Proposed component minimized inverter system

3. MODELING OF THE DRIVE SYSTEM

The complete drive system modeling involves the modeling of the IM, inverter and the controller which are discussed in the following subsections:

3.1 Inverter Model

Such a reduced structure inverter is fed by a battery pack which is divided into two equal parts so that two phases of the motor are fed by the legs of the inverter while the third one is connected to the middle voltage point of the battery pack [6].

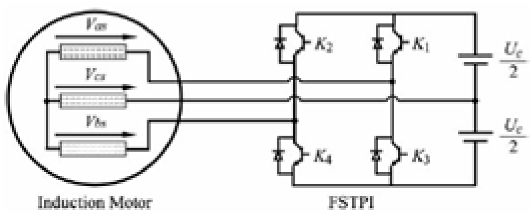

Fig.3 Four switch three phase inverter -fed induction motor drive

Let us assume that the states of the four power switches are denoted by the binary variables K1 to K4, where the binary "1" corresponds to an ON state and the binary "0" indicates an OFF state. The states of the upper and lower switches of a leg are complementary, which yields

$$K_3=1–K_1 \qquad (3)$$

$$K_4=1–K_2 \qquad (4)$$

Let us consider a Y-connection of phases of the induction motor, therefore, their terminal voltages Vas, Vbs and Vcs can be expressed as a function of the states of the upper switches as follows[4][1].

$$V_a=U_c(4K_1-2K_2-1)/6 \qquad (5)$$

$$V_b=U_c(-2K_1+4K_2-1)/6 \qquad (6)$$

$$V_c=U_c(K_1+K_2-1)/3 \qquad (7)$$

Four combinations of the states of the power switches could be distinguished. These are presented in Table 1.

Table 1 The Four Combinations of the States of the Power Switches and the Corresponding Terminal Voltages V_{as}, V_{bs} and V_{cs}

K_1	K_2	V_a	V_b	V_c
0	0	$-U_c/6$	$-U_c/6$	$-U_c/3$
1	0	$U_c/2$	$-U_c/2$	0
1	1	$U_c/6$	$U_c/6$	$-U_c/3$
0	1	$-U_c/2$	$U_c/2$	0

3.2 Induction Motor Model

The mathematical model of a three phase y connected induction motor and the load is given by the following equations in the d-q synchronously rotating reference frames as [1]

$$\begin{pmatrix} V_{qs} \\ V_{ds} \\ 0 \\ 0 \end{pmatrix} = \begin{pmatrix} R_s+pL_s & \omega_e L_s & pL_m & \omega_e L_m \\ -\omega_e L_s & R_s+pL_s & -\omega_e L_m & pL_m \\ pL_m & (\omega_e-\omega_r)L_m & R_r+pL_r & (\omega_e-\omega_r)L_r \\ -(\omega_e-\omega_r)\ L_m & pL_m & (\omega_e-\omega_r)L_r & R_r+pL_r \end{pmatrix} \begin{pmatrix} i_{qs} \\ i_{ds} \\ i_{qr} \\ i_{dr} \end{pmatrix}$$

$$T_e=(3P/4)L_m i_{qs} i_{dr}– i_{ds} i_{qr} \qquad (8)$$

$$T_e=Jm(d\omega_r/dt)+B_m\omega_r+T_L \qquad (9)$$

$$d\theta_r/dt=\omega_r \qquad (10)$$

where, V_{qs}, V_{ds} are q,d-axis stator voltages, i'_{qs}, i_{ds} are q,& d axis stator current, I_{qs}, I_{ds}, are q,d axis rotor current R_s, R_r, are the stator and rotor resistances per phase, L_s, L_r are the self inductances of the stator respectively; L_m is the mutual inductance, ω_r is the rotor speed, P is the number of poles. p is the differential operator, T_e is the electromagnetic developed torque, T_L is the load torque, J_m is the rotor inertia, B_m is the rotor damping co-efficient and θ is the rotor position.

3.3 Voltage Controller

From the above analysis it can be observed that in case of zero or very low output frequency operation the voltage fluctuations of capacitance are too high to satisfy the requirements that each capacitor voltage must be greater than the peak line to line voltage even if the overall dc link voltage can be maintained constant. Thus the lower limit of output frequency must be bounded and the transient duration must be kept as short as possible during starting. Figure shows the output voltage controller using single triangle PWM. The wanted set of three phase balanced output voltage is transformed to the set of two line –to-ground voltage and then the effect of fluctuating dc link voltage due to the ac component of dc link current is compensated .

$$V^*_{01n} = (V^*_{01}-V^*_{03})-(V^*_{c1}-V^*_{c2}) / 2 \qquad (11)$$

$$V^*_{02n} = (V^*_{02}-V^*_{03})-(V^*_{c1}-V^*_{c2}) / 2 \qquad (12)$$

These voltage references are compared by a triangular modulation signal to generate the gating signals for two leg inverter.

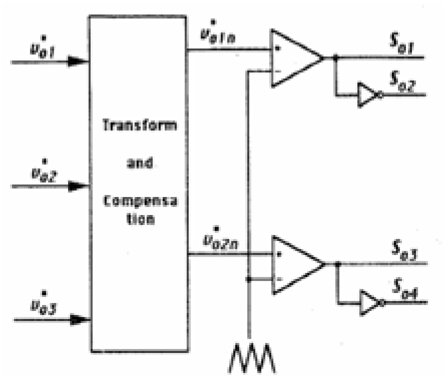

Fig .4 The dc link voltage controller of inverter

4. ANALYSIS OF SYSTEM

4.1 Analysis of the Four Switch Three Phase Inverter

For the proposed component minimized inverter, the switching requirement can be stated as follows. Given a desired set of three phase voltages and set of three phase currents for the output inverter:

$$\begin{aligned}
V_{01} &= V_0 \sin(\omega_{0t}) \\
V_{02} &= V_0 \sin(\omega_{0t} - 2\pi/3) \\
V_{02} &= V_0 \sin(\omega_{0t} + 2\pi/3) \\
I_{01} &= I_0 \sin(\omega_{0t} - \theta_0) \\
I_{02} &= I_0 \sin(\omega_{0t} - \theta_0 - 2\pi/3) \\
I_{03} &= I_0 \sin(\omega_{0t} - \theta_0 + 2\pi/3)
\end{aligned} \qquad (13)$$

Where, V_0 and I_0 are the magnitudes of the output voltages and currents ,respectively. Determine the switching function [S] that will produce a desired set of line to ground voltages

$$\begin{bmatrix} V_{01n} \\ V_{02n} \end{bmatrix} = \begin{bmatrix} S_{01} & S_{02} \\ S_{03} & S_{04} \end{bmatrix} \begin{bmatrix} V_{dc} \\ -V_{ds} \end{bmatrix}$$

$$S_{01+}S_{02=1,} \qquad S_{03+}S_{04=1}$$

$$0 < S_{0n} < 1 \ , \qquad n = 1\ldots4$$

Where

$$\begin{aligned}
V_{01n} &= V_{01} - V_{03} = \sqrt{3}\, V_{dc} \sin(\omega_{0t} - \pi/6) \\
V_{02n} &= V_{02} - V_{03} = \sqrt{3}\, V_{dc} \sin(\omega_{0t} - \pi/2)
\end{aligned} \qquad (14)$$

Where, n is the dc bus centre point assumed to be ground. Here ,the dc capacitor voltages V_{c1}, and V_{c2} are assumed to be the V_{dc}, .One can conform that the phase difference is 60. The above equations can be solved as follows

$$S_{01} = 0.5\,[\,1+a_0 \sin(\omega_0 t - \pi/6)\,]$$

$$S_{02} = 0.5\,[\,1+a_0 \sin(\omega_0 t - \pi/6)\,]$$

$$S_{03} = 0.5\,[\,1+a_0 \sin(\omega_0 t - \pi/2)\,]$$

$$S_{04} = 0.5\,[\,1+a_0 \sin(\omega_0 t - \pi/2)\,] \qquad (15)$$

Where

$$a_0 = \sqrt{3}, \frac{V_o}{V_{dc}} \qquad |\,a_0\,| < 1$$

The dc link currents will be

$$\begin{bmatrix} i_{04} \\ i_{05} \end{bmatrix} = \begin{bmatrix} S_{01} & S_{02} \\ S_{03} & S_{04} \end{bmatrix}^T \begin{bmatrix} i_{01} \\ i_{02} \end{bmatrix}$$

$$i_{04} = \frac{I_0}{2} \sin(\omega_0 t - \theta - \pi/3) + \frac{\sqrt{3}}{4} a_0 I_0 \cos\theta_0$$

$$= \frac{1}{2} i_{03} + \frac{1}{2} I_{0P}$$

$$i_{05} = \frac{I_0}{3} \sin(\omega_0 t - \theta - \pi/3) + \frac{\sqrt{3}}{4} a_0 I_0 \cos\theta_0$$

$$= \frac{1}{2} i_{03} + \frac{1}{2} I_{0P} \quad (16)$$

Where

$$I_{0P} = \frac{\sqrt{3}}{2} a_0 I_0 \cos\theta_0$$

Here, I_{ip} and I_{op} are the power components of the input and output current respectively. The power calculated on the ac side matches that on the dc side ,i.e. for the inverter side

$$P_{ac} = 3/2\,(V_0 I_0 \cos\theta_0) \quad (17)$$

$$P_{dc} = V_0(I_{04} - I_{05}) = V_0 I_{0p} = 3/2\,(V_0 I_0 \cos\theta_0) \quad (18)$$

and then capacitor charging currents will be

$$I_{c1} = i_{i4} - i_{04} = -\frac{1}{2}(i_{13} - i_{03}) + \frac{1}{2}(I_{ip} - I_{op})$$

$$I_{c2} = i_{i5} - i_{05} = +\frac{1}{2}(i_{13} - i_{03}) + \frac{1}{2}(I_{ip} - I_{op})$$

$$i_{c1} + i_{c2} = I_{ip} - I_{op} \quad (19)$$

Capacitor voltage will be

$$v_{c1} = i_{cl} \int dt, \qquad v_{c2} = i_{cl} \int dt, \quad (20)$$

The voltage fluctuations of two capacitor have two components of two frequencies with the following magnitudes, respectively

$$v_{ci} = \frac{I_i}{2\omega_i C}, \quad v_{co} = \frac{I_o}{2\omega_o C} \quad (21)$$

the overall dc link voltage will be

$$v = v_{c1} + v_{c2} = \int (i_{cl} + i_{c2})\, dt = \int (I_{ip} - I_{op})dt \quad (22)$$

The overall dc link voltage can be maintained constant by the dc link voltage controller which makes the sum of the two charging currents zero by controlling magnitude of input current Iip, to equal to Iop, but individual capacitor voltage fluctuations and depend on the operating frequency , capacitance and magnitude of current.

4.2 Harmonic Analysis

We shall calculate the Fourier series of the periodic variation of the stator voltage space vector,

$$V(n, \varepsilon) = \sum_{k=-\infty}^{\infty} [C_k \exp(jk\omega_1(n+\varepsilon)T)] \quad (23)$$

where ω_1 is the angular frequency of the fundamental harmonic. From (23), the phase voltages can be expressed as:

$$v_A(n, \varepsilon) = \mathrm{Re}\left\{ \sum_{v=-\infty}^{\infty} (C_v e^{jv\omega_1(n+\varepsilon)T}) \right\}$$

$$v_B(n, \varepsilon) = \mathrm{Re}\left\{ e^{j4\pi/3} \sum_{v=-\infty}^{\infty} (C_v e^{jv\omega_1(n+\varepsilon)T}) \right\} \quad (24)$$

$$v_C(n, \varepsilon) = \mathrm{Re}\left\{ e^{j2\pi/3} \sum_{v=-\infty}^{\infty} (C_v e^{jv\omega_1(n+\varepsilon)T}) \right\}$$

To derive the coefficients of the Fourier series, we can use the relationship between the Laplace transform of the periodic waveform and Fourier coefficients

$$C_k = \left[\frac{1}{T_1}(1-(\exp(-pT_1))V(p)\right]_{p=jk\omega 1} \quad (25)$$

V(p) is given by
$V(p)=V_1(p)+V_3(p)$ =

$$\frac{1}{p}\frac{2.V_{dc}}{3\sqrt{3}}\left[\frac{e^{pT}e^{-j\pi/6}}{e^{pT}-e^{j\pi/3}} \sum_{k=1}^{M} e^{j\pi\omega(k)/3}(e^{-pTt_{kA}} - e^{-pTt_{kB}})\right] + \quad (26)$$

$$\frac{1}{p}\frac{V_{dc}}{3\sqrt{3}}\left[\frac{e^{pT}e^{-j\pi/2}}{e^{pT}-e^{j\pi}} \sum_{k=1}^{M} e^{j\pi\omega(k)}(e^{-pTt_{kA}} - e^{-pTt_{kB}})\right]$$

and it has two parts. By substituting (25) into (26) we obtain the Fourier coefficients:

$$C_v = C_{1+6v} + C_{3+6v} = \frac{2V_{dc}e^{-j\pi/6}}{\sqrt{3}\pi j(1+6v)}\left[\sum_{k=1}^{M}\exp(j\pi o(k)/3)\left[\exp\left(-j(1+6v)\frac{\pi}{3}\varepsilon_{kA}\right) - \exp\left(-j(1+6v)\frac{\pi}{3}\varepsilon_{kB}\right)\right]\right] +$$

$$\frac{V_{dc}e^{-j\pi/2}}{\sqrt{3}\pi j(3+6v)}\left[\sum_{k=1}^{M}\exp(j\pi o(k))\left[\exp\left(-j(3+6v)\frac{\pi}{3}\varepsilon_{kA}\right) - \exp\left(-j(3+6v)\frac{\pi}{3}\varepsilon_{kB}\right)\right]\right]$$

Where V=0,+1,+2,…

From (22) we can derive analytical equations for the Fourier series of the phase voltages as follows:

PHASE A

$$\sum_{v=-\infty}^{\infty}\left[\frac{-4V_{dc}}{\pi\sqrt{3}(1+6v)}\sum_{k=1}^{M}\left[\sin\frac{\pi}{6}(1+6u)\Delta\varepsilon_k\right]\sin\left[(1+6v)\left[\omega_1(n+\varepsilon)T - \frac{\pi}{6}(\varepsilon_{kA}+\varepsilon_{kB})\right] + \frac{\pi o(k)}{3} - 2\pi/3\right]\right] +$$

$$\sum_{v=-\infty}^{\infty}\left[\frac{-2V_{dc}}{\pi\sqrt{3}(3+6v)}\sum_{k=1}^{M}\left[\sin\frac{\pi}{6}(3+6u)\Delta\varepsilon_k\right]\sin\left[(3+6v)\left[\omega_1(n+\varepsilon)T - \frac{\pi}{6}(\varepsilon_{kA}+\varepsilon_{kB})\right] + \pi o(k)\right]\right] \quad (28)$$

PHASE B

$$u_B = \sum_{v=-\infty}^{\infty}\left[\frac{-4V_{dc}}{\pi\sqrt{3}(1+6v)}\sum_{k=1}^{M}\left[\sin\frac{\pi}{6}(1+6u)\Delta\varepsilon_k\right]\sin\left[(1+6v)\left[\omega_1(n+\varepsilon)T - \frac{\pi}{6}(\varepsilon_{kA}+\varepsilon_{kB})\right] + \frac{\pi o(k)}{3}\right]\right] +$$

$$\sum_{v=-\infty}^{\infty}\left[\frac{-2V_{dc}}{\pi\sqrt{3}(3+6v)}\sum_{k=1}^{M}\left[\sin\frac{\pi}{6}(3+6u)\Delta\varepsilon_k\right]\sin\left[(3+6v)\left[\omega_1(n+\varepsilon)T - \frac{\pi}{6}(\varepsilon_{kA}+\varepsilon_{kB})\right] + \pi o(k) + 2\pi/3\right]\right]$$

Similar equation can be obtained for the phase C from (28) and (29), it may be seen that the fundamental armonics is lowered by 1.73, as compared with the fundamental harmonics in the conventional inverter.

6. SIMULATION RESULTS

Simulation circuit of four switch inverter is shown in Figure 5. Figure 5.(b). shows a component minimized three phase inverter fed Induction motor current waveforms, comparison between the traditional six switch three phase inverter and the component minimized three phase inverter are identical one. It is evident from Figure 5(b) that starting phase current is in the acceptable range, which is also verified by traditional six switch three phase inverter. The harmonic spectrum of a phase current ia ,for the proposed inverter is shown in Figure 5(d).The Total harmonic distortion (THD) of ia is found 4.79% where as the THD of ia for traditional six switch three phase inverter is found 24.69% as shown in Figure 6(b).

It is found that the performance of the proposed Four Switch three phase inverter based drive is much close to that of the traditional six switch three phase inverter. The analysis and simulation results show that this inverter can dramatically reduce the complexity of the control algorithms and cost.

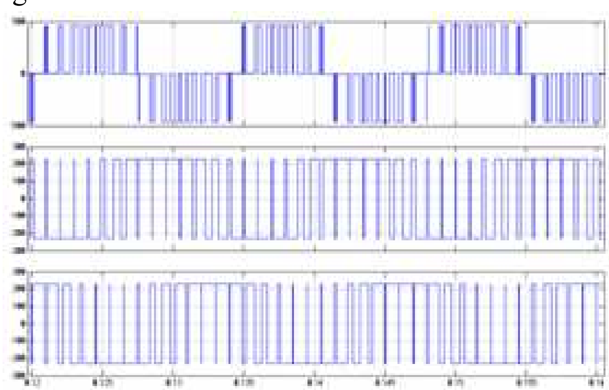

Fig. 5(b) Output voltages

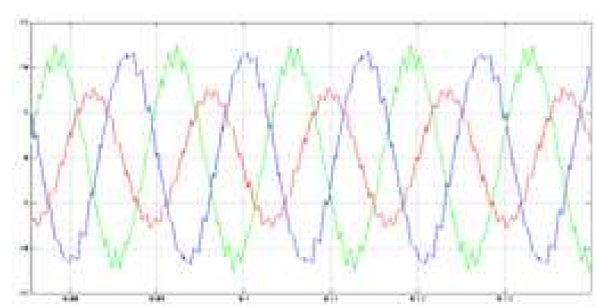

Fig. 5(a) Phase currents

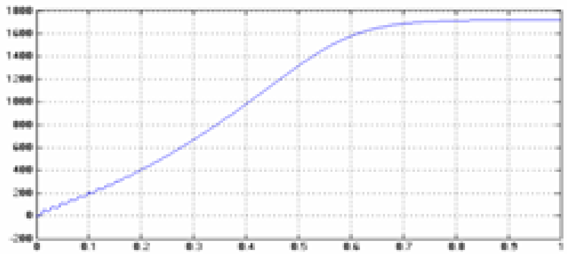

Fig. 5(c) Response curve for speed

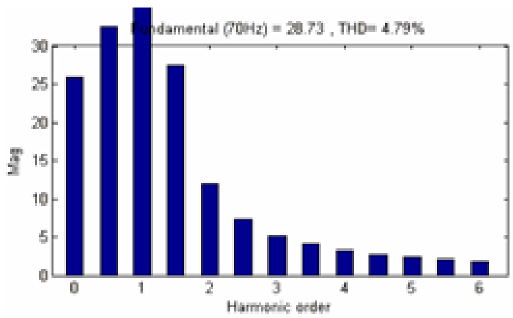

Fig. 5(d) Harmonic spectrum

Figure 5 Simulation response of the Four Switch three phase inverter (a) steady state three phase currents (b) PWM Output voltages (c) speed response, (d) Harmonic spectrum.

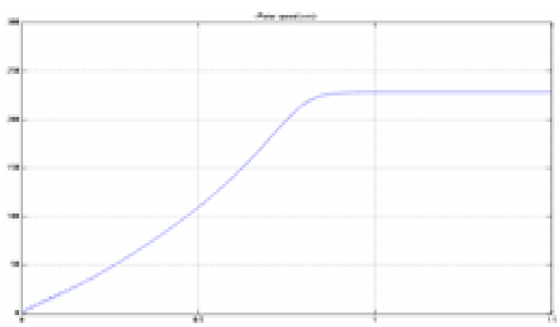

Fig. 6(a) Response curve for speed

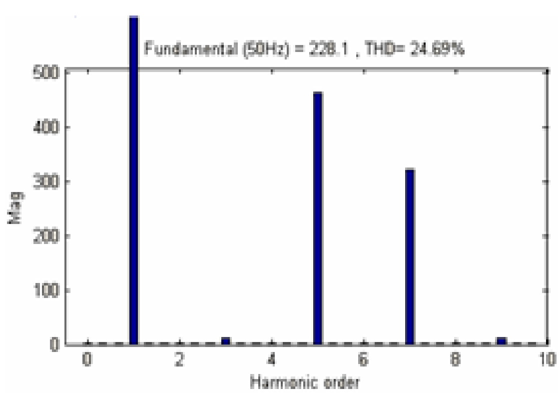

Fig. 6 (b) Harmonic spectrum

Figure 6 Simulation response of the conventional six switch three phase inverter (a) speed response and (b) Harmonic spectrum

7. EXPERIMENTAL RESULTS

A laboratory model has been built to verify the Operation. The PWM control of the FSTP Inverter was tested using AT89C2051 Micro Controller and a three phase induction motor. In the experimental tests the load is a three phase induction motor (wound rotor, 0.5H.P)

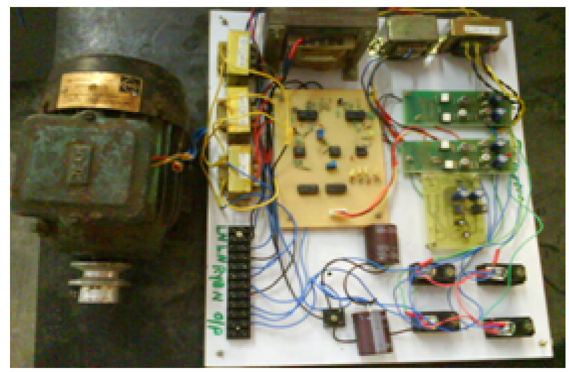

Fig 7. Laboratory model of the FSTP Inverters

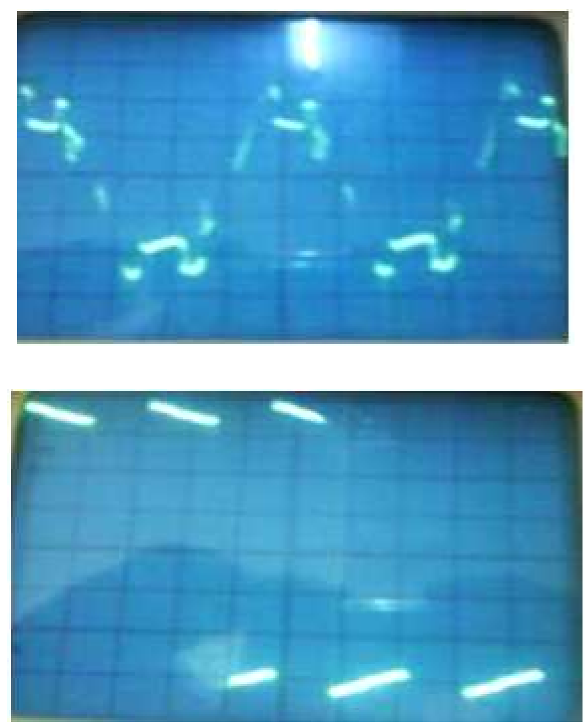

Fig 8. Experimental voltage waveforms of the FSTP inverters

Figure 8 shows experimental waveform, although the wave shape is different from the simulation. This is because the line voltage is distorted in the lab, which was not considered in the simulation. Figure 7 & 8 shows the Laboratory model and experimental voltage waveform obtained with the FSTP Inverter.

7. CONCLUSION

In this paper, a modified cost effective component minimized three phase induction motor drive is presented. The proposed structure requires only four switches and two split capacitors in the dc link inverter and has the capability of requiring only sinusoidal input currents with unity power factor. A mathematical model of the system has been derived using generalized modulation theory and verified by the experimental results. Under some limitations the proposed structure appears to be a promising and far more economical topology than the conventional VSI-PWM system with six switch inverters.

Also a performance comparison of the proposed Four Switch three phase inverter fed drive with a conventional six switch three phase inverter fed drive is also made in terms of total harmonic distortion (THD) of the stator current and speed response. The Four Switch three phase inverter is found acceptable for high performance

REFERENCES

[1] C.B. Jacobina, E.R.C. Silva, A.M.N.Lima and R.L.A. Ribeiro, "Vector and Scalar Control of a Four Switch Three Phase Inverter", Proceedings of the IEEE Industry Applications Society Annual Meeting, Orlando, FL,Vol. 3, 1995, pp. 2422-30.

[2] F. Blaschke, "The Principle of Field Orientation as Applied to the New Transvector Closed Loop Control System for Rotating Field Machines", Siemens Review, Vol. 34, 1972, pp. 217-20.

[3] I. Boldea and S.A.Nasar, "Vector Control of AC Drives", CRC Press, Boca Raton, FL, 1992.

[4] F. Blaabjerg, S. Freysson, H. H. Hansen, and S. Hansen, "Comparison of a Space-Vector Modulation Strategy for a Three Phase Standard and a Component Minimized Voltage Source Inverter," in Proc., EPE Conf., 1995, pp. 1806-1813.

[5] B. Elbadsi, A. Guermazi, and A. Masmoudi, "New Space Vector PWM Strategy Intended for a Low-Cost Four-Switch Three-Phase Inverter-Fed Induction Motor Drive", Paper Presented at CD-ROM of the Third IEEE International Conference on Systems, Signals and Devices, Sousse, 2005.

[6] M.Nasir Uddin,T.S.Radwan and M.A.Rahman "Performance Analysis of Four Switch 3-phase Inverter Fed IM drives" Paper Presented in Third IEEE International Conference.

[7] H.W. Van Der Broeck and J.D. Van Wyh, "A Comparative Investigation of a Three-Phase Induction Machine Drive with a Component Minimized Voltage-fed Inverter Under Different Control Options", IEEE Transactions on Industry Applications, Vol. 20 No. 2, 1984, pp. 309-20.

[8] G. Kim and T. A. Lipo, "VSI-PWM Rectifier/ Inverter System with a Reduced Switch Count," in Proc. IEEE-IAS Annu. Meeting, 1995, pp.2327-2332.

[9] B.K.Bose, "Power Electronics and AC Drives", EnglewoodCliff NJ Prentice Hall,1986.

Bending Behaviour of Polyester Air-Jet-Textured and Cotton-Yarn Fabrics

B. R. Das[1], R. S. Rengasamy[2] and Y. B. Patil[3]

Department of Textile Technology, Indian Institute of Technology, New Delhi - 110 016, India

(Received on 10 June 2009 and accepted on 12 July 2010)

Abstract

Air-jet-textured polyester yarns were produced using two feed yarns differing in filament fineness and number of filaments. By varying the overfed rates of feed yarns, filament fineness and air pressure, four textured yarns were produced. Woven fabrics were prepared using these textured yarns as weft and cotton yarns in warp. To study the effect of air-jet-texturing parameters on the bending properties, the woven fabrics were tested for thickness, bending rigidity & hysteresis of bending moment. Statistical significant test was carried out at 99% confidence level to trace out the specific trend followed by the fabrics. Statistical analysis is based on the assumption of normal distribution of dataset. Axial orientation of filaments and disposition of loops influences the bending properties. Frictional resistance mostly influences the hysteresis of bending moment. Increase in air pressure during texturing creates turbulence to disturb the axial orientation of the filaments; results in changes in fabric thickness & bending properties. Fabrics with coarser filament have higher bending rigidity due to higher moment of inertia.

Keywords: *Air pressure, Air-jet textured fabric, Bending, Core & sheath over feed, Filament denier*

1. INTRODUCTION

The comfort characteristics like fabric aesthetic property, thermal comfort and physical comfort like handle of clothing material are getting more priority in the quality evaluation of fabric. The fabric handle mainly depends on its low-stress mechanical properties. The low stress mechanical property of fabric such as shear, bending and tensile together with compression and surface friction have, therefore become essential facets of fabric and clothing objective measurement technology [1]. Fabric properties, especially bending properties exert a major influence on the handle and draping behaviour of apparel fabrics [2]. The bending behaviour of the material is expressed in terms of bending rigidity. Bending rigidity is a measure of ease with which the fabric bends. The fabrics bending rigidity basically depends on the constituent fibres & yarns from which the fabric is manufactured, the fabric construction and most importantly, the nature of the chemical treatment given to the fabric. Inter-yarn and intra-yarn friction plays important role in deciding the bending behaviour and the type of chemical treatment given to the material, mainly controls this frictional restraint. Bending at low stress is more important, because it has a direct relationship and greater association with fabric handle. The higher the rigidity, the lower the fabric handle value [3]. The bending rigidity of a woven fabric is slightly greater than the sum of the bending resistance of the component yarns [4]. More recent work done by Thierron has shown a high correlation between the flexural rigidities of ring, rotor, air-jet spun yarns and the bending lengths of their corresponding knitted fabrics. Thierron and later, Subramaniam et al. concluded that yarn structure as it relates to fibre arrangement within the yarn has an important influence on the bending behaviour of yarns and fabrics [5, 6].

Most of the synthetic fibres have few moisture absorbing groups and lack inherent bulkiness due to their chemical nature and physical structure. These limitations seriously hinder their application in apparels. Furthermore, they are deficient in providing adequate bulk, cover, warmth and soft feel. Synthetic fibres have high strength, abrasion resistance, durability and dimensional stability coupled with their thermoplastic character; this has motivated textile manufacturers to bulk them in order to improve their comfort characteristics. Improvement in the bulk of continuous-filament yarns is generally achieved by ‘texturing’, a process that introduces crimps, coils, loops and wrinkles to modify the geometry of the constituent filaments to make the yarn more voluminous [7]. Apart from the improvements in the bulk characteristics of fabrics made from textured yarns, there are other added advantages like improved pill resistance, crease resistance, dimensional stability, durability, flexibility, cover and appearance. The textured-yarn fabrics are easy to wash and dry. They also retain strength, abrasion resistance and toughness of the continuous-filament yarn [8]. Air-jet-textured yarns partially simulate the spun yarns, because of their surface loops. The structure of an air-jet-textured yarn depends on the texturing parameters: air pressure, overfeeds of core and effect components, filament denier, number of filaments and positioning of coarse and fine filaments in core or sheath and vice versa. Fabrics produced from these yarns are affected by their structures and fabric construction parameters. In this article, we discuss on the effect of air pressure, differential change in core & sheath overfeed and filament fineness on the bending properties of fabrics.

2. MATERIALS AND METHODS

Polyester yarns of 50 denier (5.5 tex)/48 filaments and 75 denier (8.33 tex)/36 filaments were used as feed yarns for air-jet texturing. The details of feeder yarns are given in Table 1.

Table 1 Details of Feeder Yarns Used for Air-Jet Texturing

Yarn Code	Yarn Tex	No. of Filaments	Filament Fineness (DTEX)
A1	5.55	48	1.156
A2	8.33	36	2.313

2.1 Air-jet Texturing

Texturing was done on Eltex AT-HS air-jet texturing machine at a speed of 400 m/min and air pressure of 9 kgf/cm^2, using a nozzle 'HemaJet Core S325'. After texturing, yarns were stretched by 4.7%, heat set at 200^{0}C and wound with a stretch of 0.9%. During heat setting, yarns were overfed by 2.9% to the heater. The core and sheath overfeeds were varied to get textured yarns of different structures. Core yarns were wetted using water jet, at a pressure of 2 kgf/cm^2 and flow rate of 0.5 L/jet/h, before feeding them into air nozzle. Textured yarns were produced using the combination of feeder yarns A1 and A2. The count of the textured yarns was kept constant to 20 tex .Textured yarns with codes and details of process parameters are given in Table 2.

Table 2 Yarns Textured with Various Process Parameters

Sample Code	Air Pressure Kgf/cm^2	Overfeed of Components%		Feed Yarn Used		Wetting of End
		Core or Normal*	Effect	Core or Normal*	Effect	
S1	9	11	21.5	A1	2 × A1	core
S2	8	11	21.5	A1	2 × A1	core
S3	9	15	20	A2	A2	core
S4	9	15	19.5	A1	2 × A1	core

2.2 Preparation and Wet Processing of Woven Fabrics

Fabrics were woven using the textured yarns as weft and 15-tex cotton yarn as warp on a Saurer automatic loom at 200 picks/min. Ends and pick density (per inch) were kept at 68 and 50, respectively. The fabric codes made from yarns S1–S4 are F1–F4 respectively. Fabrics were desized, scoured and bleached in an industry.

2.3 Evaluation of Bending Properties

The bending properties of fabric were evaluated using KES (FB2) pure bending tester. The tester is used for pure bending tests of thin films materials such as fabrics, leather etc. A fixed chuck holds one edge of the sample, while moving chuck holds the other. The moving chuck follows a fixed orbit turning its head at an angle, so that a uniform curvature is maintained on the sample to find the relationship between the curvatures and bending moment. Clamp interval is 1 cm. and rate of bending is 0.5/cm.sec. Maximum curvature is +/- 2.5/cm. The bending parameters; bending rigidity-B (gf.cm^2/cm) and Hysteresis of bending moment-2HB (gf.cm/cm) were measured.

3. RESULTS AND DISCUSSIONS

Fabric thickness, bending properties; bending rigidity and hysteresis of bending moment of fabrics are shown in Table 3 and Statistical analysis was carried out on the thickness & bending properties at 99% confidence level and the inference drawn is presented in Table 4.

Table 3 Bending Properties of Fabrics

Sample Code		B	2HB	T (mm)
F1	Warp	0.094	0.050	0.31
	Weft	0.018	0.016	
F2	Warp	0.094	0.052	0.28
	Weft	0.022	0.016	
F3	Warp	0.091	0.051	0.27
	Weft	0.039	0.017	
F4	Warp	0.092	0.053	0.30
	Weft	0.021	0.016	

B-Bending rigidity (gf.cm^2/cm), 2HB- Hysterisis of bending moment (gf.cm/cm), T-Fabric thickness (mm)

Table 4 Statistical Significance Test

Sets	Bwp	Bwt	2BHwp	2BHwt	T
S1, S2	NS	S	NS	NS	S
S1, S4	NS	S	NS	NS	NS
S3, S4	NS	S	NS	NS	S

Bwp- Bending rigidity in warp direction, Bwt-Bending rigidity in weft direction, 2BHwp-Bending hysteresis in warp direction, 2BHwt-Bending hysteresis in weft direction, S-Significant, NS-Not significant

3.1 Effect of Air Pressure

Yarns S1 & S2 are textured at 9 & 8 bar of air pressure respectively, while keeping the same core & sheath overfeed of filaments. The higher air pressure used during air-jet texturing of yarn S1 create more air turbulence and form more number of core & sheath loops, compared to yarn S2. Higher air turbulence also leads to disorientation of filament's core & loops, hence the yarn S1 is loose and bulky compared to yarn S2. Fabric F1 carrying loose & bulky textured yarn S1 display statistically higher thickness than fabric F2. The same cotton yarn is used in the warp direction of both the fabric F1 & F2, hence display almost similar value of bending rigidity (Bwp) in warp direction. The difference between the bending rigidity (Bwp) in warp direction is statistically insignificant, as shown in Table 4. The value of bending rigidity (Bwt) in weft direction increases with decrease in air pressure from 9 bar to 8 bar. Higher air pressure during texturing creates turbulence to disturb the axial orientation of the filaments; hence the filament yarn S2 textured with lower air pressure carries filaments, which are comparatively flat & aligned to the yarn axis than the filaments of yarn S1. As the parallel filaments work together to resist bending moment, the fabric F2 carrying yarn S2 displays higher value of bending rigidity (Bwt) than fabric F1. It is observed that, there is statistically no difference between the value of hysteresis of bending moment (2HBwp & 2HBwt) in warp & weft direction of fabrics F1 & F2. Bending of fabric occurs with initial resistance offered by the yarn-yarn friction at the cross-over points, then inter-filament friction depending on the cohesiveness of filaments and finally, by bending of the yarns. The contribution of the yarn-yarn and inter-filament friction cannot recover, after the removal of bending moment. The hysteresis of the bending moment is mostly constituted of frictional resistance offered during bending. The yarn S1 carrying disorientated filaments with higher number of loops are less compacted than yarn S2, hence will offer higher yarn-yarn friction, because of shearing of more contacting areas. Yarn S2 carrying flat and orientated filaments than are more compacted and behave cohesively, hence offer higher inter-filament friction than yarn S1. The no difference between the hysteresis of bending moment values of fabrics could be ascribed to the similar resultant frictional resistance of yarn-yarn friction at cross-over points and inter-filament friction.

3.2 Effect of Differential Change in Core & Sheath Overfeed

The effect of differential changes in core & sheath overfeeds on fabric thickness & bending properties are shown in Table 3. It is observed that, there is statistically no difference between the thickness values of fabrics F1 & F4. The yarn S4 carries higher core loops and lower sheath loops, where as yarn S1 carries higher sheath loops and lower core loops. Though there is difference in the total density of core & sheath loops, due to differential change in core & sheath overfeed, but it is insufficient to cause any difference in the textured yarn thickness. The fabrics F1 & F4 constituted of yarns S1 & S2 don't reflect any difference in their values of thickness. It is statistically observed that, there is no difference between the values of bending rigidity (Bwp) in warp direction of fabric F1 & F4, which is due to similar cotton yarns used in the warp direction. Fabric F4 displays higher bending rigidity (Bwt) in weft direction than fabric F1, irrespective of no difference in the thickness values. The bending rigidity is mostly influenced by the axial orientation of the filaments in yarn; though the frictional resistance has some contributions. Yarn S4 carries filaments with lower loop density than yarn S1, due to differential change in overfeed rates, hence the axial orientation of filaments is higher in yarn S4 than S1; which could be the possible reason behind the higher bending rigidity (Bwt) of fabric F4 than F1. It is observed that, there is statistically no difference in the values of hysteresis of bending moments (2HBwp & 2HBwt) in warp & weft direction of fabrics F1 & F4, which could be due to the similar explanation, as mentioned in section 3.1.

3.3 Effect of Filament Fineness

The effect of changes in feed yarns on thickness & bending properties are shown in Table 3. It is statistically observed that, fabric F4 indicates higher value of thickness than fabric F3. The relationship between bending rigidity values of yarn and diameter of single filament is as shown in Eq.1 [9];

$$G_y = (nEIIr^4)/4 \tag{1}$$

Where, G_y is the yarn bending rigidity; n is number of single filaments; E is initial tensile modulus of filament; r is filament radius. According to the equation, the coarser filament of yarn S3 will have higher bending rigidity than yarn S4. The size of loops formed during texturing, is influenced by the bending rigidity of filaments. Higher bending rigidity will lead to higher bending curvature, results in larger size loops and vice-versa. Yarn S3 carrying coarser filament will lead to formation of larger loops, where as yarn S3 will form smaller loops. The smaller loops are resilient and show higher stability to deformation than larger loops; hence fabric F4 indicates higher thickness than fabric F3. It is statistically observed that, there is no difference between the bending rigidity (Bwp) values of fabrics F3 & F4, which is due to the similar cotton yarns used in warp direction. Fabric F3 made from coarser filament textured yarn has higher values of bending rigidity (Bwt) than fabric F4 made from finer filaments. This is due to higher bending rigidity of yarn S3 than S4. There is statistically no difference between the values of hysteresis of bending moments (2BHwp & 2Hbwt) in warp & weft direction of fabrics F3 & F4; which could be due to the similar explanation, as mentioned in section 3.1.

4. CONCLUSION

The bending rigidity (Bwp) of fabric in warp direction is mostly dependent on the type of warp yarns used and independent on the texturing process parameters employed to produce the textured weft yarns. There is statistically no effect of change in air-pressure, differential changes in core & sheath overfeeds and changes in feed yarns on the bending rigidity of fabrics in warp direction. The hysteresis of bending moment is constituted of yarn-yarn friction at the cross-over points and inter-filament friction. The hysteresis in bending moments in both the warp and weft direction is statistically found to be independent of the texturing process parameters; change in air-pressure, differential changes in core & sheath overfeeds and changes in feed yarns. Increase in turbulence with increase in the air pressure decreases the axial orientation of the filaments, resulting in increase in fabric thickness and decrease in bending rigidity in weft direction. Differential change in core & sheath overfeed (higher increase in core overfeed than decrease in sheath overfeed) causes no change in fabric thickness, but increases bending rigidity in weft direction. Increase in filament fineness increases bending rigidity in weft direction & decreases the fabric thickness.

REFERENCES

[1] B. K. Behera and D. B. Shakyawar, "Structure-Property Relationship of Fibre, Yarn and Fabric with Special Reference to Low-Stress Mechanical Properties and Hand Value of Fabric", Indian Journal of Fibre Textile Research, Vol.25, No.9, 2000, pp. 232-237.

[2] P. Radhakrishnaiah, "Low Stress Mechanical Behaviour of Cotton/Polyester Yarns and Fabrics in Relation to Fiber Distribution within the Yarn", Textile Research Journal, Vol.66, No.2, 1996, pp. 99-103.

[3] B. K. Behera, "Comfort and Handle Behaviour of Linen Blended Fabrics", Autex Research Journal, Vol.7, No.1, 2007, pp.33-47.

[4] P. Grosberg, "The Mechanical Properties of Woven Fabrics, Part II: The Bending of Woven Fabrics", Textile Research Journal, Vol.36, No.3, 1966, pp. 205- 211.

[5] W. Thierron, "The Flexural Rigidity of Polyester Fibre-Cotton Yarns Produced on the Ring, Rotor and Friction Spinning Systems", Journal of Textile Institute, Vol.76, No.6, 1985, pp. 454-458.

[6] V. Subramaniam, G. Nalankilli, V. Mathivanan and K. Jagannathan, "Abrasion Resistance of Ring and Rotor Spun Yams in Relation to their Coefficient of Friction", Textile Research Journal, Vol.57, No.6, 1987, pp.369-370.

[7] N. Eskin, "Analysis of a High Temperature Heater in a False Twist Texturing Process", Energy Conversion and Management, Vol.44, No.9, 2003, pp. 2531-2547.

[8] I.C. Sharma and V. Bhargava, "Influence of Number of Filaments of Textured Yarn on Fabric Characteristics", Indian Textile Journal, Vol.94, No.10, 1983, pp.99-103.

[9] V. K. Kothari, "Quality Control", Development Commissioner for Handlooms, Ministry of Textiles, Government of India, 2000.

What the Nonwovens and Technical Textiles Sectors in India Need?

Seshadri Ramkumar
Nonwovens & Advanced Materials Laboratory, Texas Tech University, Lubbock, TX 79409
E-mail: s.ramkumar@ttu.edu
(Received on 08 November 2010 and accepted on 15 January 2011)

1. INDIAN ECONOMY AND GROWTH SCENARIO

According to the recent Global Economics Prospects report by the World Bank, Indian economy is expected to grow at a rate of 7.5-8% during 2010-12. In addition, according to this report, FDI inflows are expected to grow due to India's efforts to relax investment limits in some sectors and the simplification of foreign direct investment procedures. India's rising middle income population will fuel the domestic consumption of products such as hygiene and feminine care which will be the drivers for growth for the nonwovens and technical textiles (NWTT) industry. The Asian Development Bank (ADB) in its latest report, "The Asian Development Outlook 2010", has stated that the strong domestic consumption and the growing investments will put India's economy in the growth trajectory. ADB emphasizes the importance of domestic consumption and infrastructural investments on the growth of Indian economy, meaning more opportunities for the technical textiles industry.

2. STATUS OF THE INDIAN TEXTILES INDUSTRY

India's textile industry is a conventional industry dominated by cotton. According to a recent report by the Ministry of Textiles, India, there are 1834 textile mills with an installed capacity of 37 million ring spindles, 489,718 rotors and 56,526 looms. Compared to the capacity of the conventional textile industry, the nonwoven roll good production is between 80,000 and 100,000 metric tons. Textiles industry, which includes the nascent technical textiles sector, contributes 4% to the GDP and 14% to the industrial production. The two main reasons which make the Indian textiles industry strong are: 1) export earnings and 2) employment opportunities. India's textiles industry employs some 35 million people directly and contributes 17% to the total export earnings of the country.

3. NEED FOR TECHNICAL TEXTILES SECTOR IN INDIA

The economic strength of the Indian textiles industry comes from its export earnings. The competitive advantage that India had in terms of its labor cost has been eroding slowly and smaller nations such as Bangladesh and Vietnam due to cheaper labor and trade agreements with the US and Europe are gaining advantageous positions with regard to foreign trade. More recently, the decrease in the consumer spending and the global economic recession have forced the Indian textile industry to start thinking seriously about technical textiles. The government and the industry are looking for diversification opportunities to enlarge the overall market size of the Indian textiles industry. India textiles industry wants to reach the size of US $ 115 billion by 2012. The expectation is that the technical textiles sector will contribute at least 10% to the overall market size, which will be US $ 11.5 billion. The current value of the Indian technical textiles sector is around US $8 billion. This means, India's technical textiles sector has to nearly double in size in years ahead. All stake holders, i.e., industry and trade associations, Government, industry related trade associations and textile academia and working seriously to build a viable technical textiles sector in India. In this connection, Government of India is playing a significant role in creating awareness and developing a knowledge base for the NWTT sector.

4. MARKET SIZE OF INDIA'S TECHNICAL TEXTILES SECTOR

In India, the value-added textiles industry is collectively grouped into to a single sector commonly referred to as technical textiles. This sector encompasses fiber to converted products industry. Indian technical textiles industry is nascent and highly fragmented. Government of India sponsored a nation-wide market survey to estimate the size, need and the growth potential of this industry. ICRA, a management consultancy undertook the government sponsored study and has estimated the current market size to be 398,760 million Indian rupees (~US $8.86 billion). It is expected to grow at 11% to reach a size of 664,050 million Indian rupees (~US $14.76 billion) by 2012-13. The consumption will be slightly under the market size. The report divides the technical textiles sector into 12 segments as categorized by the TechTextil years ago. The largest segments are Packtech, Clothtech, Indutech and Meditech. In my opinion, the categorization of the nascent Indian technical textiles into 12 segments is premature and will cause confusions. There are several products that can fit well in many segments and such a categorization for an emerging market may not be suitable. In order to have an easier and useful segmentation from the point of view of marketing, we have proposed a three way classification of the technical textiles sector: 1) Consumer Products; 2) Institutional Products and 3) Government Procurement Products. Consumer products include personal care, baby care and hygiene products. In this category, global brands such as Huggies and Pampers have penetrated into the market. Major players are P&G, Kimberly-Clark, SCA-Godrej and Johnson and Johnson. Products from these major international companies are predominantly sold in pharmacies and retails stores such as Birla's More and Big Bazaars. The consumers that use these products are predominantly middle-income, upper middle class and those from the upper strata of the society. The cost and the lack of awareness prohibit the penetration of these products into the rural and low income areas. There will be growth in the consumption of institutional products such as geotextiles, automotive textiles and hospital products. India has a plan to build 20 kilometers of national highway per day which will lead to more consumption of technical textiles products. Government procurement category also offers scope as the Ministry of Defence, Government of India has recently streamlined its procurement policies. Those countries that have quality defense textiles products and liaison bodies in India will have advantages over the others.

5. WHAT THE INDIAN NWTT SECTOR NEEDS?

i. There is an immediate need for the converting sector in India. Due to the growing domestic consumption and increase in wages, the need for consumer products at affordable rates will rise. International NWTT industry, machinery makers and trade bodies should look for win-win opportunities in the creation of converting clusters.
ii. India has adequate roll good manufacturers although not of high quality. The needs of the domestic market as of today can be met with the existing capacity. There are approximately 50 spunbond manufacturers with predominantly Chinese, Korean and Taiwanese machinery.
iii. The industry at present is reluctant to invest in high-end machinery as the market is not established and well built for marketing the products.
iv. Technical schools to educate and train skilled workers who can be employed in the growing NWTT sector are needed.
v. Knowledge on converting roll goods to end-user products is needed. This also includes knowledge on chemical finishing and formulation developments.
vi. Marketing know-how and coordinated approach towards marketing are needed.

All stake holders have realized the need for a coordinated body to represent the interests of the growing technical textiles industry. The NWTT sector in India has just formed the Indian Technical Textiles Association (ITAA) with its current headquarters in Mumbai.

To sum up, in 2008, we predicted based on the available GDP growth numbers for India from the World Bank, India's NWTT sector will grow at a rate of 13% in the following years. The government of India sponsored market survey by the ICRA consultancy is forecasting a growth of 11% per annum. In a general sense, the growth will be in double digits. As elaborated above, there is an emergent need to grow the converting sector, which will spearhead the growth of other segments of the NWTT sector. Machinery makers, fabric producers, fiber manufacturers and industry trade bodies should take note of the above immediate needs of the Indian NWTT industry and the Indian market and engage in relevant trade talks and promotional activities.

Effect of Transverse Steel on the Performance of RC T-beams Strengthened in Shear with GFRP Composites

K.C. Panda[1], S.K. Bhattacharyya[2] and S.V. Barai[3]

[1,2&3]Department of Civil Engineering , Indian Institute of Technology, Kharagpur, Kharagpur - 721 302, India

E-mail: kishorbiet@yahoo.co.in, pandakishor@civil.iitkgp.ernet.in, bsri@civil.iitkgp.ernet.in

(R)

Abstract

The need for structural rehabilitation of concrete structures all over the world is well established and a large amount of research is devoted in this area. Though a large volume of research is directed towards the flexural behaviour of beams, works on the effect of fiber reinforced polymer (FRP) strengthened on shear are relatively sparse. The focus of the present paper is on the study of the effect of transverse steel on the performance against shear and modes of failure of simply supported reinforced concrete (RC) T-beams strengthened in shear with glass fiber reinforced polymer (GFRP) composites. RC T-beams of 2.5 m span are cast at the structural laboratory of IIT, Kharagpur, and are tested with shear reinforcement and GFRP composites in U-shape around the web with one, two, and three layers. All the beams are tested on a 300 Ton hydraulic testing machine. The experimental results clearly indicate the advantage of using externally applied epoxy bonded GFRP system to restore or increase the shear capacity of RC T-beams. It is also observed that the combination of GFRP layers and transverse steel is an important factor to gain the shear capacity and the ductility.

Keywords: *Shear strengthening, Glass fiber-reinforced polymer (GFRP), Reinforced concrete (RC), T- beams*

1. INTRODUCTION

There is a large need for strengthening and retrofitting of concrete structures all over the world and is essential due to several reasons such as aggressive environment, industrial pollution, corrosion, use of deicing salt, aging of concrete structures, faulty design or construction and due to different natural disasters. Fiber-reinforced polymers (FRPs) are becoming very promising material for reinforced concrete structures, due to their advantageous properties such as high strength-to-weight ratio, high stiffness-to-weight ratio, high corrosion resistance, high durability, non magnetic, non conductive, high resistance to chemical attack as well as ease of its installation. FRP composites have been used in automobile, electronics, and aerospace engineering for several decades, but the application in civil engineering structure as a reinforcing material is relatively recent in origin. Nowadays the FRP composite have been applied to many structural elements including beams, columns, slabs, joints, walls, domes, tanks, chimneys, and pipes etc.

Though a large volume of research is directed towards the flexural behaviour of beams, works on the effect of FRP strengthened on shear are relatively sparse. Shear failure of an RCC beam is a type of failure mode which has a catastrophic effect. If an RCC beam deficient in shear strength is over loaded, shear failure may occur suddenly without advance warning of distress, because it is brittle in nature. Shear deficiency of the beam may occur due to many reasons such as insufficient shear reinforcement or reduction in steel area due to corrosion, increased service load and construction errors. In addition, there is an urgent need to upgrade the shear resistance of older RC structures to meet the current seismic design standards in high seismic regions. In this situation, externally bonded FRP reinforcement may be used efficiently in strengthening the concrete beams weak in shear.

Most of the experimental works have been conducted by using Carbon Fiber Reinforced Polymer (CFRP) as external shear reinforcement both for rectangular (Triantafillou 1998; Khalifa et al. 1998, 2002) and T-beams (Khalifa et al. 2000); as compared with GFRP as external shear reinforcement. The works by using GFRP as strengthening material are very limited both for rectangular (Al Sulaimani *et al.* 1994; Cao *et al.* 2005) and T-beams (Chajes *et al.* 1995; Deniaud *et al.* 2003). However, based on literature, (Chaallal *et al.* 2002; Bousselham *et al.* 2006) have been studied the effect of transverse steel on the performance against shear of RC T beams strengthened in shear with CFRP composites, whereas Pelligrino *et al.* (2002) studied the effect of transverse steel using RCC rectangular beam strengthened in shear with CFRP composites. The objective of the present study is to investigate the effect of transverse steel on the performance against shear and modes of failure of simply supported RC T-beams strengthened in shear with GFRP composites.

2. EXPERIMENTAL PROGRAM

2.1 Test Specimens

The experimental program consists of nine (9) simply supported RC T-beams of 2.5 m long. Six beams are tested as control beam; three beams are tested without shear reinforcement, only the stirrups are provided at the support and loading points to avoid the local shear failure and the rest three beams are tested with shear reinforcement, the stirrups are provided @ 300 mm c/c. Another three beams are with shear reinforcements, the stirrups are provided @ 300 mm c/c and strengthened in U-shape around the web with one layer, two layers, and three layers of GFRP composites.

The control specimen not strengthened with GFRP are labeled 0L, whereas specimens strengthened with one, two, and three layers of GFRP are labeled as 1L, 2L, and 3L. The series S0 refers to specimens with no transverse steel reinforcement. Series S300 corresponds to specimens with steel stirrup spacing 300 mm. Thus, for example, specimen S0-0L-1 is a beam without steel stirrups (S0), without GFRP layer (0L), and sample number one whereas the strengthened specimen designated as S300-1L-CT-U-90, with steel stirrups @ 300 mm c/c (S300), strengthened with one layer of GFRP (1L), continuous wrapping (CT), in U-shape around the web of the T-beams (U), and orientation of the fiber angle (90º) to the longitudinal axis of the beam.

2.2 Design of Concrete Beam

All the T-beams are 2.5 m long and designed to fail in shear. Two Nos. 20 mm diameter Tor steel bars are used as flexural reinforcement (area 628.31 mm^2) at the bottom, and four Nos. 8 mm diameter Tor steel bars are used in one layer at the top. The internal steel stirrups are 6 mm diameter and are spaced 300 mm c/c in S300 specimen, whereas in S0 specimen total six number of stirrups are provided, 2 Nos. at the support and 1 No. at the loading points to prevent local failure. The control specimen details and dimensions are shown in Figure 1.

2.3 Materials

A concrete mix with Ordinary Portland Cement (OPC- 43 grade) and 12.5 mm down graded coarse aggregates are used for casting. The mix design is carried out for M30 grade of concrete. The mix design proportions of cement, fine aggregate, and coarse aggregate are (1:0.946:2.03). The water cement ratio by weight is 0.375. The slump tests are conducted in each batch of mixing, the value varying between the range 30 mm to 50 mm. Compression tests on control and strengthened specimen on cubes and cylinders are performed at 7 days and 28 days. The compressive strength of cubes and cylinders are presented in Table 1.

The steel reinforcement bars are also tested in the laboratory according to Indian standards. Tata Tiscon steels are used as reinforcement. Fe 415 for longitudinal steel reinforcement and Fe 250 for transverse steel reinforcement are used in the experiment. The summary of testing results is presented in Table 2.

The resin treated fiber glass fabric 0.32 ×100 cm used for GFRP composite. Epoxy adhesive is used to attach the glass fabric to the beam; the resin used is a 9:1 mixture of Araldite CY-230 and hardener HY-951. The coupons of 1 layer, 2 layers and 3 layers of glass fiber composites are prepared and tested using 60 Ton UTM (Tinius Olsen). The one layer GFRP thickness is 0.36 mm and the ultimate tensile strength measured 160 MPa and the elastic modulus is 13.18 GPa.

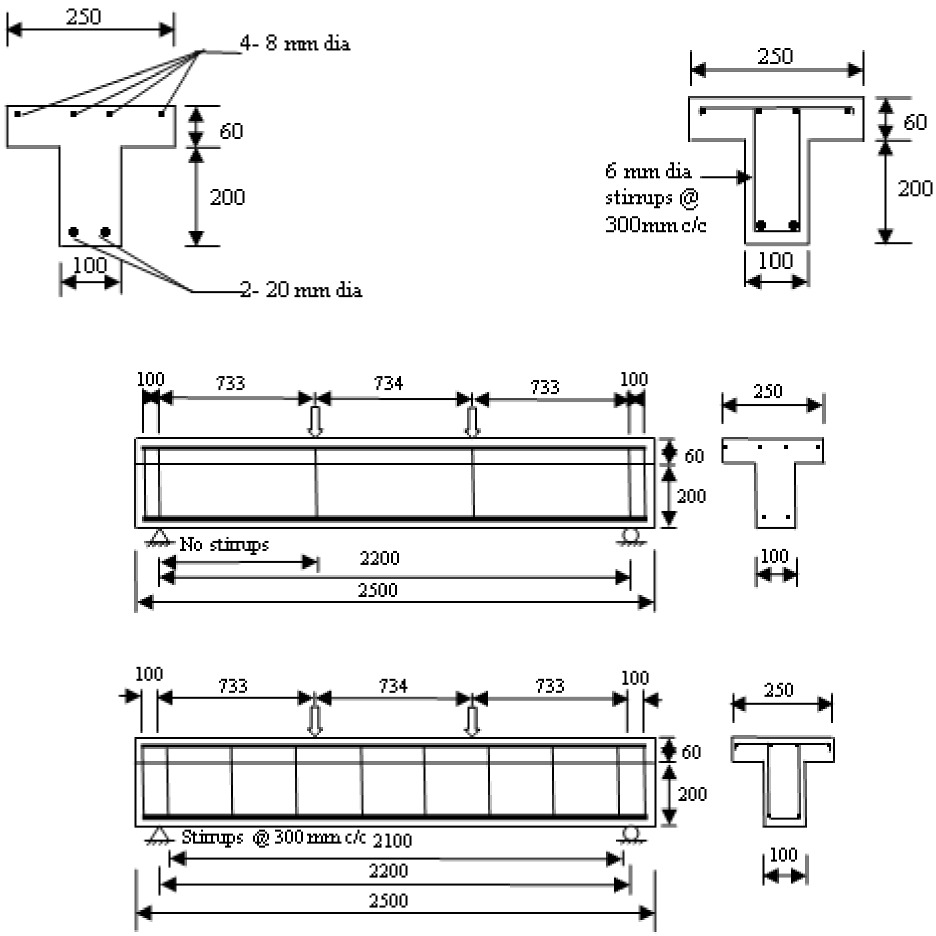

Fig.1 Details of control specimen

Table 1 Test Results of Cubes and Cylinders after 28 Days

Specimen Designation	No. of Beam	Mean Cube Compressive Strength (MPa)	Mean Cylinder Compressive Strength (MPa)	Modulus of Elasticity as Per IS: 456-2000 (MPa)	Modulus of Elasticity as Per Test Results (MPa)
S0-0L	3	49.61	42.16	35217.18	34645.97
S300-0L	3	57.62	39.53	37953.92	36236.18
S300-1L-CT-U-90	1	52.06	39.35	36076.30	36565.40
S300-2L-CT-U-90	1	52.06	39.35	36076.30	36565.40
S300-3L-CT-U-90	1	52.06	39.35	36076.30	36565.40

Table 2 Mechanical Properties of Steel Reinforcement Used

Diameter (mm)	Yield Stress (MPa)	Ultimate Stress (MPa)	Modulus of Elasticity (GPa)	Yield Strain (μ strains)
20 (Tor steel)	500	590	200	2500
8 (Tor steel)	503	646	180	2794
6 (Mild steel)	252	461	200	-

2.4 Strengthening Schemes

All the T-beams are provided with the same flexural reinforcement and the transverse steel reinforcement are varied and provided without stirrups in S0 series, whereas in S300 series, the stirrups are @ 300 mm c/c. The T-beams are strengthened with one layer, two layers, and three layers of GFRP composite in the form of continuous U-shape around the web, the main fiber direction oriented perpendicular to the longitudinal axis of the beam in S300-series. The details of the specimens are listed in Table 3.

Table 3 Details of Test Specimens

Specimen	Strengthening Schemes
S0-0L	Control beam without transverse steel
S300-0L	Control beam with transverse steel @ 300 mm c/c
S300-1L-CT-U-90	With transverse steel @ 300 mm c/c + one layer of GFRP continuous sheet + U-jacket + 90° to the longitudinal axis of the beam
S300-2L-CT-U-90	With transverse steel @ 300 mm c/c + two layers of GFRP continuous sheet + U-jacket + 90° to the longitudinal axis of the beam
S300-3L-CT-U-90	With transverse steel @ 300 mm c/c + three layers of GFRP continuous sheet + U-jacket + 90° to the longitudinal axis of the beam

2.5 Test Set Up

All specimens are tested as simple T-beams using two points loading with shear span to effective depth ratio (a/d) equal to 3.26. The tests have been carried out at the structural laboratory of Civil Engineering Department, IIT Kharagpur using 300 Ton capacity Mohr and Federhoff machine. Figure 2 shows the details of the test set-up.

Fig. 2 Test setup of specimen S300-3L-CT-U-90

Five dial gauges are used for each test to monitor vertical displacements. One dial gauge is located at mid span of the beam. Two are located below the loading points and the other two are located at the center of the shear zone on either side as shown in Figure 2.

Two types of electrical strain gauges are used in the test; gauges BKNIC-10 are used on the surface of the longitudinal steel reinforcement and transverse steel, and for surface application gauges BKCT-30 are used. BKNIC-10 is attached on the longitudinal steel and transverse steel to measure deformation during the different stages of loading and to monitor yielding. In S300-1L-CT-U-90 and S300-2L-CT-U-90 three strain gauges are attached; one in the longitudinal steel surface at 150 mm distance and the two other strain gauges are attached in two stirrups at coordinates (350,90), and (650,145) from the support, whereas in S300-3L-CT-U-90 four strain gauges are attached. Figure 3 shows the details of the internal strain gauge fixing photo.

Fig. 3 Internal strain gauge fixing photo of specimen S300 series

BKCT-30 strain gauges are attached on the concrete surface side of the web of the T-beams and to the GFRP surface on the side of the strengthened T-beams and oriented in the fiber direction. Six strain gauges are used on concrete surface, three strain gauges used at the middle of each side of the shear zone as a strain rosette. Eight strain gauges are mounted to the GFRP surface on the expected plane of the shear cracks on both sides of the strengthened T-beams; four strain gauges attached each side as per the cracking pattern of the control beam. The details of strain gauge positions are given in Figure 4.

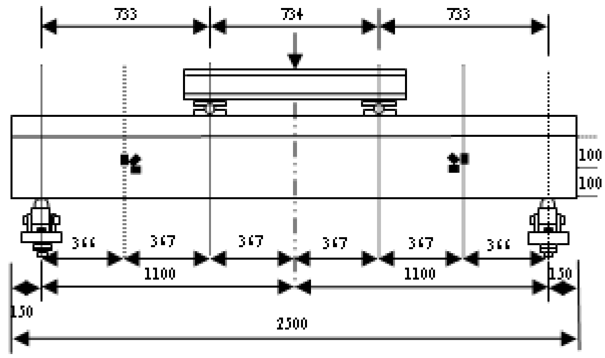

Fig. 4a. Location of strain gauge on control beam

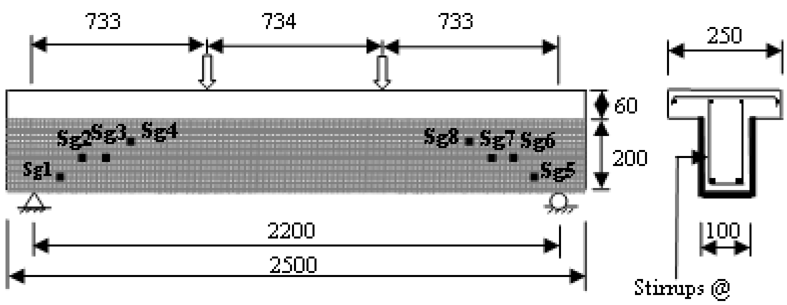

Figure 4b. Location of strain gauge on strengthened beam

3. ANALYSIS OF TEST RESULTS AND DISCUSSIONS

The experimental results in terms of total load versus mid span deflection for the tested beams of S300 series, having zero, one, two, and three layers of GFRP sheets are shown in Figure 5, while the cracking pattern and modes of failure of the corresponding beams are shown in Figure 6.

Table 4 shows the comparison between the experimental GFRP sheet contribution and ACI predicted shear resistance results of S300 series and also provides the failure modes observed in the experiments.

3.1 Strength

From Figure 5 and Table 4, it may be observed that for specimen S300-1L-CT-U-90, the load at ultimate failure attained 156 kN, compared to 141 kN for S300-0L specimen; that is a gain of 10.64 %. As for the influence of the GFRP thickness on the gain in strength, the addition of second and third layer of GFRP; that is for S300-2L-CT-U-90 and S300-3L-CT-U-90 the load at ultimate failure are 160 kN and 184 kN respectively. The percentage gain is 13.47 % and 30.5 % respectively as compared with control specimen S300-0L. It is observed that the percentage of gain in strength is not so much difference between single and double layer specimen, but as compared with control specimen S300-0L, very less. Whereas in three layers specimen the gain in strength is more, as compared with the control specimen S300-0L.

3.2 Ductility

As observed from Figure 5, the deflection of control specimen and strengthened specimen is almost same up to 60 kN load. Thereafter, as load increased, the deflection in beam strengthened with GFRP is less in comparison to the control specimen for the same amount of load. However, the deflection of the strengthened beam is almost same up to 120 kN load. As expected beam strengthened with three layers of GFRP carry more load and deflection than the other two and also shows more ductile behaviour.

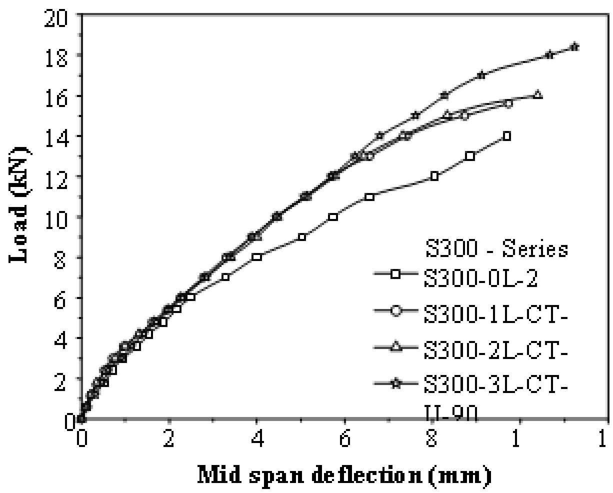

Fig. 5 Load versus mid span deflection - Series S300

3.3 Cracking Pattern and Modes of Failure

3.3.1 Control T-beams

In Figure 6a, when beam S0-0L-1 is loaded, it exhibited diagonal shear cracks at a load of 70 kN on either side of shear spans; the cracks started at the center of both shear spans. As the load increased, the cracks widen and propagated towards the support and loading points through the flange of the T-beams and leading to failure at a load of 104 kN. At the same time a horizontal crack appeared at the flange and it covers a distance of 275 mm approximately, thereafter, the horizontal crack inclined in approximately 15º angle for a distance of 280 mm .

In Figure 6b, when beam S300-0L-2 is loaded, the number of inclined shear crack appeared after 70 kN load. However, the diagonal critical shear crack exhibited at a load of 90 kN on both sides of shear span. The critical shear crack started approximately at 300 mm distance from the support. As load increased, this crack started to widen and propagated towards the support and loading points through the flange, and leading to ultimate failure at a load of 146 kN. It is observed that a hair crack appeared at top of the flange and it propagated in longitudinal direction from the loading position for a distance of 185 mm then it bends approximately in 90º angles.

3.3.2 Strengthened T-beams

In Figures 6c, 6d, and 6e, when specimen is loaded, the initiation of the GFRP strain started at a load of about 90 kN. As load increased, the GFRP strain increased more and more at the expected plane of critical shear failure zone, but in specimen S300-1L-CT-U-90 the GFRP ruptured along the direction of critical shear failure at the ultimate load of 156 kN. Whereas in specimen S300-2L-CT-U-90, and S300-3L-CT-U-90 the GFRP debonded from the concrete surface at the ultimate load of 160 kN and 184 kN respectively. At the same time, inclined cracks appeared in the side faces of the flange and it covers approximately 300 mm distance from the loading position. Also some hair crack observed at top surface of the flange.

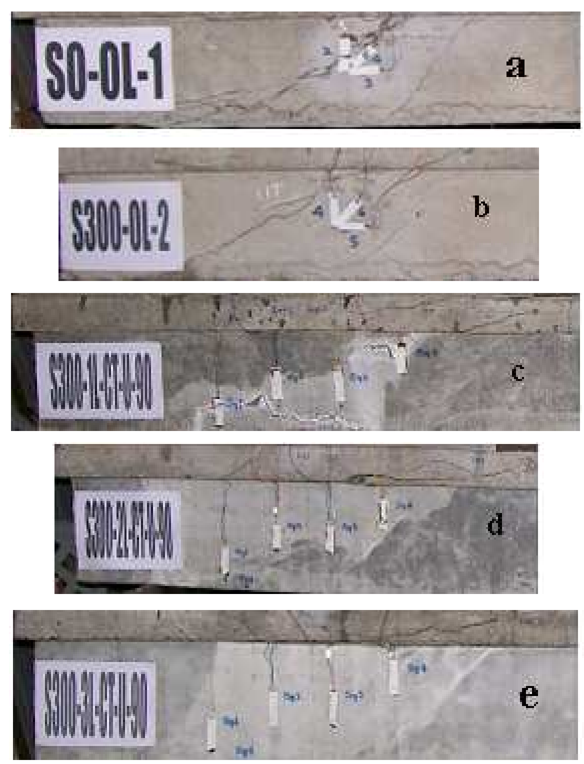

Fig. 6 Failure modes of tested beams

3.4 Strains

3.4.1 GFRP Vertical Strain

Figure 7, 8, and 9 presents the load versus vertical GFRP strains of specimen S300-1L-CT-U-90, S300-2L-CT-U-90, and S300-3L-CT-U-90 respectively. The strain in the GFRP in all the strain gauges did not contribute to the load carrying capacity up to 90 kN loads approximately. After 90 kN load, the strain in the strain gauge Sg3, in specimen S300-1L-CT-U-90 started to increase steadily and reached the maximum value of 7739 μstrains at 130 kN load. Whereas in S300-2L-CT-U-90, and S300-3L-CT-U-90 specimen the maximum strain observed 5348, and 7018 in Sg1 and Sg3 strain gauges respectively.

In series S300, the GFRP strain is higher in the specimens strengthened with one layer of GFRP, as compared to two layers, and three layers. It is also observed that in S300-1L-CT-U-90, and S300-3L-CT-U-90 specimens, the GFRP strains are higher at 350 mm distance from support, whereas in S300-2L-CT-U-90 specimen, it is 150 mm distance from support.

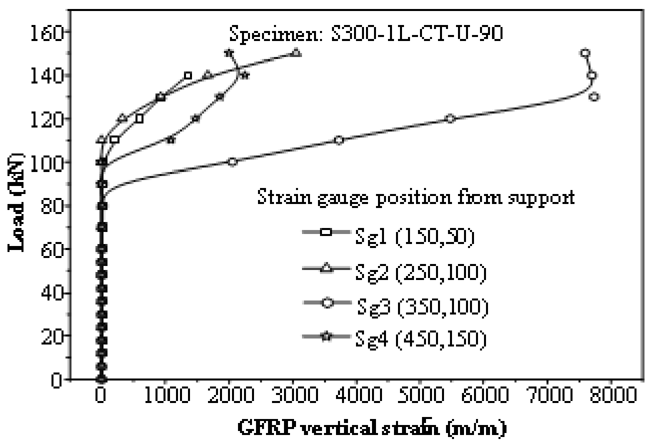

Fig.7 Load versus GFRP vertical strains of specimen S300-1L-CT-U-90

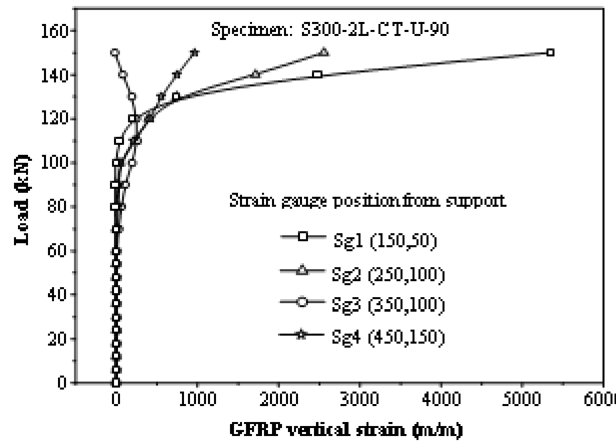

Fig.8 Load versus GFRP vertical strains of specimen S300-2L-CT-U-90

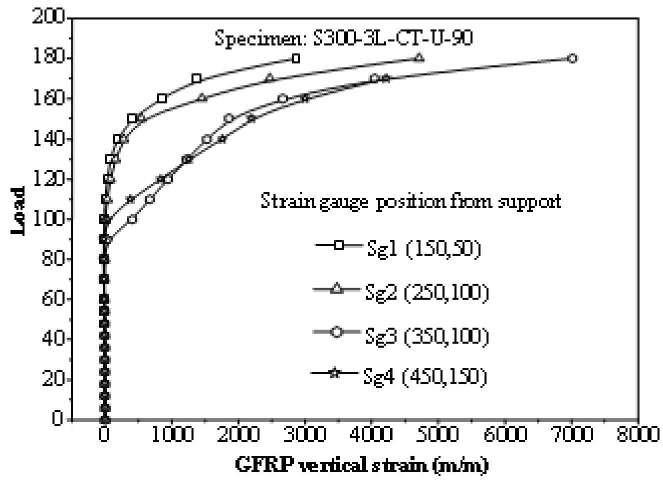

Fig. 9 Load versus GFRP vertical strains of specimen S300-3L-CT-U-90

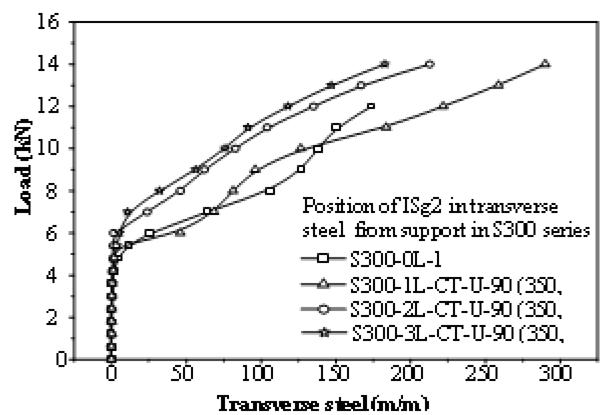

Fig. 10 Load versus transverse steel strains - S300 series

3.4.2 Transverse Steel Strain

The curve representing the load versus the strains in the transverse steel reinforcement in terms of number of layers of GFRP presented in Figure 10 for series S300. It is observed that like-wise the GFRP, the transverse steel reinforcement did not contribute to the load carrying capacity in the initial stage of loading. This contribution is more effective after diagonal cracking. In the control unstrengthened specimen S300-0L, this occurred at an applied load of approximately 54 kN, whereas for the strengthened specimen S300-1L-CT-U-90, S300-2L-CT-U-90, and S300-3L-CT-U-90 it occurred at an applied load of approximately 54 kN, 60 kN, and 70 kN respectively.

It is observed from Figure 10, the addition of the GFRP delayed the contribution of the transverse steel to the load carrying capacity of the T-beams. However, beam strengthened with second and third layer of GFRP resulted in an additional decrease of the strains in the transverse steel (Bousselham *et al.* 2006).

4. VALIDITY OF PROPOSED DESIGN APPROACH

The comparison between the test results and calculated shear strength using the ACI 440.2R-02 design approach are listed in Table 4. It may be observed that the $V_{f,test}$ results are almost equal with the $V_{f,theor}$ results in all the specimens. The $V_{f,test}$ results in S300-1L-CT-U-90 and S300-3L-CT-U-90 specimens are more as compared with $V_{f,theor}$ results, whereas in S300-2L-CT-U-90 specimen the $V_{f,test}$ result is less as compared with $V_{f,theor}$ result.

5. CONCLUSIONS

The test results clearly indicate that for strengthened RC T-beams in shear with U-shaped GFRP wrap; increase the effectiveness by 10.64 % to 30.5 %.

Based on the observation, the following conclusions are emerging from the present research:

The gain in shear capacity is significant in all the GFRP strengthened RC T-beams. But so far as the number of layers is concerned, three layers are more effective than one and two layers.

Table 4 Comparison of Experimental and ACI Predicted Shear Resistance Results

Specimen	Experimental Results						Theoretical Results Predicted by ACI 440.2R-02 Design Approach				Modes of Failure
	Load at Failure (kN)	Total Shear Resistance $V_{n,test}$ (kN)	Resistance Due to Concrete $V_{c,test}$ (kN)	Resistance Due to Steel $V_{s,test}$ (kN)	Shear Resistance Due to GFRP $V_{f,test}$ (kN)	$\frac{V_{f,test}}{V_{n,test,ref}}$ X100 (%)	$V_{f,theor}$ (kN)	$V_{c,theor}$ (kN)	$V_{s,theor}$ (kN)	$\phi V_{n,theor}$ (kN)	
S0-0L	100	50	50	-	-	-	-	26.68	-	22.68	Shear Compression
S300-0L	141	70.5	50	20.5	-	-	-	25.95	10.60	31.07	Shear Compression
S300-1L-CT-U-90	156	78	50	20.5	7.5	10.64	6.26	25.90	10.60	35.54	Rupture Failure
S300-2L-CT-U-90	160	80	50	20.5	9.5	13.47	12.05	25.90	10.60	39.73	GFRP Debonding
S300-3L-CT-U-90	184	92	50	20.5	21.5	30.5	18.79	25.90	10.60	44.60	GFRP Debonding

The modes of failure of strengthened RC T-beams in shear with U-shaped GFRP wrap clearly indicates that, in single layer wrapping, the failure is due to GFRP rupture, whereas for two and three layers, the failure is due to GFRP debonding.

The load-strain curves clearly indicate that, for S300 series, the combination of transverse steel and layer both results the more utilization of GFRP strain, and attained the maximum strain in strengthened RC T-beams.

The addition of internal transverse steel resulted in a significant decrease of the gain in shear capacity due to GFRP.

But the combination of layer and transverse steel is an important factor to gain the shear capacity. The combination of three layers with internal transverse steel in S300 series resulted good effectiveness as compared with one and two layers.

The load-transverse steel strain curve clearly indicates that the strain in transverse steel is more in control specimen, as compared with strengthened specimens for the same amount of load. This means that the addition of GFRP eased the transverse steel. But as layer concerned, the addition of second and third layer of GFRP sheets resulted in an additional decrease of strains in the transverse steel.

The load-deflection graph clearly indicates that the RC T-beams strengthened in shear with GFRP sheets have a significant effect on beams ductility. The RC T-beams, become more flexible and more deformable, after strengthened with GFRP sheets.

REFERENCES

[1] ACI Committee 440, "Guide for the Design and Construction of Externally Bonded FRP Systems for Strengthening Concrete Structures (ACI 440.2R-02)", American Concrete Institute, Farmington Hills Mich., 2002, pp.45.

[2] G. J. Al-Sulaimani, A. Sharif, I. A. Basunbul, M. H. Baluch and B.N. Ghaleb, "Shear Repair for Reinforced Concrete by Fiberglass Plate Bonding", ACI Structural Journal, Vol.91, No.3, 1994, pp. 458-464.

[3] A. Bousselham and O. Chaallal, "Effect of Transverse Steel and Shear Span of the Performance of RC Beams Strengthened in Shear with CFRP", Composites: Part B, Vol. 37, 2006, pp. 37-46.

[4] S. Y. Cao, J. F. Chen, J. G. Teng, Z.Hao and J. Chen, "Debonding in RC Beams Shear Strengthened with Complete FRP Wraps", Journal of Composites for Construction, Vol. 9, 2005, pp. 417-428.

[5] O.Chaallal, M.Shahawy and M.Hussan, "Performance of Reinforced Concrete T-Girders Strengthened in Shear with Carbon Fiber-Reinforced Polymer Fabric", ACI Structural Journal, Vol.99, No.3, 2002, pp.335-343.

[6] M. J. Chajes, T. F. Januszka, D. R. Mertz, T. A. Jr. Thomson and W. W., Jr. Finch, "Shear Strengthening of Reinforced Concrete Beams Using Externally Applied Composite Fabrics", ACI structural Journal, Vol.92, No. 3, 1995, pp.295-303.

[7] C. Deniaud and J. J. R. Cheng, "Reinforced Concrete T-beams Strengthened in Shear with Fiber Reinforced Polymer Sheets", Journal of Composites for Constructions, Vol. 7, No.4, 2003, pp.302-310.

[8] A.Khalifa and A.Nanni, "Rehabilitation of Rectangular Simply Supported RC Beams with Shear Deficiencies Using CFRP Composites", Construction and Building Materials, 2002, pp.135-146.

[9] A.Khalifa and A.Nanni, "Improving Shear Capacity of Existing RC T-section beams using CFRP Composites", Cement and Concrete Composites, Vol. 22, 2000, pp.165-174.

[10] A.Khalifa, W.Gold, A. Nanni and A. Aziz, "Contribution of Externally bonded FRP to Shear Capacity of RC Flexural Members", Journal of Composites for Construction, Vol. 2, No.4, 1998, pp.195-201.

[11] C. Pellegrino and C. Modena, "Fiber Reinforced Polymer Shear Strengthening of Reinforced Concrete Beams with Transverse Steel Reinforcement", Journal of Composites for Construction, Vol. 6, No.2, 2002, pp.104-111.

[12] T. C. Triantafillou, "Shear Strengthening of Reinforced Concrete Beams Using Epoxy Bonded FRP Composites", ACI Structural Journal, Vol.95, No.2, 1998, pp.107-115.

Advanced Steganography for Lossy Compression Images

C.P. Shantala[1] and K.V. Vishwanatha[2]
[1]Channabasaveshwara Institute of Technology, Bangalore - 572 216, Karnataka
[2]Department of Computer Science and Engineering, R.V.College of Engineering, Bangalore - 560 059, Karnataka
E-mail: shantala_cp@yahoo.co.in
(Received on 04 July 2009 and accepted on 10 April 2010)

Abstract

Applying steganography for the images like JPEG is not straight forward process due to its lossy compression. The objective of this paper is to carry out a brief research on steganography. Based on the research findings, develop and implement a steganographic application to hide data in a computer image file, as well as retrieve the hidden data from the image containing the hidden data and improving the hiding capacity by encrypting and compressing the data.

Keywords: *Cryptography, Data Compression,JPEG Compression, Steganography.*

1. INTRODUCTION

The purpose of steganography is to hide messages in innocent looking carriers. The purpose is to achieve security and privacy by masking the very presence of communication. Historically, the first steganographic techniques included invisible writing using special inks or chemicals. It was also fairly common to hide messages in text. By recovering the first letters from words or sentences of some innocent looking text, a secret message was communicated. Today, it seems natural to use binary files with certain degree of irrelevancy and redundancy to hide data. Digital images, videos, and audio tracks are ideal for this purpose.

The subject of steganography has been brought into limelight by several intelligence agencies and the news media in recent times following some terrorist attack all around the globe. It has been alleged that these terrorists, apart from using state of the art communication technologies and media, are using cryptography as well as steganography to aid themselves with their objectives.

Despite the sins steganography carries due to some cynical comments by some people, it can be put to good use. We all need privacy, that is the reason most of us prefer sending a letter in an envelop instead of a postcard. Cryptography has aided us to turn intelligible data into gibberish data to disappoint the prying eyes of nosy people. However, some countries disallow use of cryptography. Cryptographic text can quite easily be identified. A message, either encrypted or unencrypted, can be hidden in a computer image file and transmitted over the Internet, a CD or DVD, or any other medium. The image file, on receipt, can be used to extract the hidden message. Hiding the message in the image file enables the deniability of the existence of any message at all.

2. OBJECTIVES

The objective of this paper is to carry out a brief research on steganography. Based on the research findings, develop and implement a steganographic application to hide data (other files containing images, text, etc.) in a computer image file. There are lots of steganographic programs available. A few of them are excellent in every respect, especially the non-freeware programs. Unfortunately, most of them lack usable interfaces, or contain too many bugs, or unavailability of a program for other operating systems.

3. IMAGE FORMATS

3.1. Graphics Interchange Format (GIF)

GIF was developed by CompuServe back in 1987 to display color images. Although present day computers can display millions of colors, graphics hardware back then could only display this amount of colors. Although GIF is not suitable for displaying color real world photographs for modern day video cards and monitors capable of displaying millions of colors, it is still excellent for graphics.

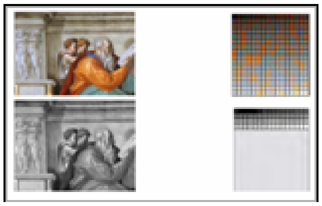

Fig. 3.1 GIF images with color palettes of 256 and 64 colors

GIF uses a lossless compression scheme called LZW which accounts for its small size. It has a color table (palette) which can contain up to a maximum of 256 colors. Each pixel of the image maps to the color entries in this table. If the exact color is not in the table, the pixel points to the color with the closest match. Due to the color limitation, GIF can be very poor for displaying photographs; JPEG performs really well for photographs, and on most occasions, the ideal choice. Alongside JPEG, GIF is the most popular image formats on the Internet.

3.2 Joint Photographic Experts Group (JPEG)

The Joint Photographic Experts Group released the JPEG standard in the early 1990s to meet the needs for high quality image compression standards for the storage and transmission of real world photographic images.

The image standard makes use of human visual characteristics and advanced mathematics to deliver high quality photographic images. JPEG was developed with photographs in mind, hence the word photographic in its name. It can achieve very high levels of compression. It uses a lossy compression scheme, meaning some data of the image is lost due to the compression. Compression is achieved not using a single algorithm, like LZW in GIF, but a number of different compression schemes. JPEG is not suitable for graphics, only real world photographs. JPEG images have become one of the two most popular image formats on the Internet.

3.2.1 JPEG Image Compression

Appling the steganography for the images like JPEG is not straight forward process due to its lossy compression. That's why JPEG steganography software is very rare. There is plenty of software around that can hide data in BMP images. Unfortunately, BMP pictures are not widely used or exchanged, unlike JPEG. So, why programmers don't do steganography programs for JPEG. There are two main reasons. The first one is technical. JPEG format is very complex. An order of magnitude is more complex than a flat, uncompressed format like BMP. There are many variations you must take in account. Although you have a few libraries to deal with this format, and although for steganography with quantized DCT coefficients, you can stop between steps 3 or 4 (i.e. run length encoding-RLE and then recompress everything); few programmers will have the patience to tear apart the guts of a JPEG image. That's why someone who just wants to play around not very seriously with steganography will use BMP format. And that's why even serious programs which claim to do JPEG steganography actually fake it (Invisible Secrets hides the data in the comment field of the header; Secure Engine adds the hidden data at the end of the file; nevertheless, both are not bad for BMP steganography, and are certainly coded by people who understand cryptography and steganography). The second reason is more conceptual. The concept of lossy compression like the one used in JPEG (or MP3 for audio) is to remove most of the unimportant or redundant information. The concept of most steganography algorithms is to hide bits by replacing this very same unimportant or redundant information (like the Least Significant Bits). So both techniques are going in opposite directions. The more you compress, the more difficult it is to find room to hide data.

The JPEG image compression standard has become an important tool in the creation and manipulation of digital images. The primary algorithm underlying this standard is executed in several stages. In the first stage, the image is converted from RGB format to a video-based encoding format in which the grayscale (luminance) and color (chrominance) information are separated. Such a distribution is desirable because grayscale information contributes more to perceptual image quality than does color information, due to the fact that the human eye uses grayscale information to detect boundaries. Color information can be dispersed across boundaries without noticeable loss of image quality. Thus, from a visual standpoint, it is acceptable to discard more of the color information than grayscale information, allowing for a greater compression of digital images.

In the second stage, the luminance and chrominance information are each transformed from the spatial domain into the frequency domain. This process consists of dividing the luminance and chrominance information into square (typically 8 x 8) blocks and applying a two-dimensional Discrete Cosine Transform (DCT) to each block. The ideal Discrete Cosine Transform is of the form.

$$F(u,v) = (1/4)[C(u)C(v)\sum_{x=0}^{7}\sum_{y=0}^{7} f(x,y) \cos\left(\frac{(2x+1)u\pi}{16}\right)\cos\left(\frac{(2y+1)v\pi}{16}\right)],$$

$$\text{where} \quad C(u),C(v) = \begin{cases} 1/\sqrt{2} & \text{for } u,v=0, \\ 1 & \text{for all other values of } u,v. \end{cases}$$

Equation 3.1 DCT

The cosine-transform converts each block of spatial information into an efficient frequency space representation that is better suited for compression. Specifically, the transform produces an array of coefficients for real-valued basis functions that represent each block of data in frequency space. The magnitude of the DCT coefficients exhibits a distinct pattern within the array, where transform coefficients corresponding to the lowest frequency basis functions usually have the highest magnitude and are the most perceptually significant. Similarly, cosine transform coefficients corresponding to the highest frequency basis functions usually have the lowest magnitude and are the least perceptually significant.

In the third stage, each block of DCT coefficients is subjected to a process of quantization, wherein grayscale and color information are discarded. Each cosine transform coefficient is divided by its corresponding element in a scaled quantization matrix, and the resulting numerical value is rounded. Basically the process is.

$$\text{Round}\left(\frac{\text{DCT } 8\times 8 \text{ block}}{\text{Quantization Table}}\right) = \textit{Sparse Matrix}$$

Equation 3.2 Quantization

The default quantization matrices for luminance and chrominance are specified in the JPEG standard, and were designed in accordance with a model of human perception.

The scale factor of the quantization matrix directly affects the amount of image compression, and the lossy quality of JPEG compression arises as a direct result of this quantization process. Quantizing the array of cosine transform coefficients is designed to eliminate the influence of less perceptually significant basis functions. The transform coefficients corresponding to these less significant basis functions are typically very small to begin with, and the quantization process reduces them to zeros in the resulting quantized coefficient array. As a result, the array of quantized DCT coefficients will contain a large number of zeros, a factor that is employed in the next stage to deliver significant data compression.

In the fourth stage, a process of run-length encoding is applied to each block of quantized cosine transform coefficients. A zigzag pattern is employed in the run-length encoding scheme to exploit the number of consecutive zeros that occur in each block. The zigzag pattern is as follows.

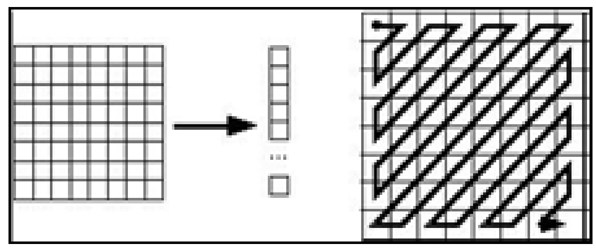

Fig. 3.4 zigzag pattern

The zigzag pattern progresses from low-frequency to high-frequency terms. Because the high-frequency terms are the ones most likely to be eliminated in the quantization stage, any run-length encoded block will typically contain at least one large run of zeros at the end. Thus, the amount of space required to represent each block can be substantially reduced by representing a run of zeros as (0, n), where n is the number of zeros occurring in the run. In the fifth and final stage, the resulting data may be further compressed through a loss-less process of Huffman coding. The resulting compressed data may then be written to the computer hard drive in a file for efficient storage and transfer.

4. DESIGN

Hiding the data in the images merely hides the data. Anyone can use the program to retrieve the hidden data from the image. The message would be encrypted using a secure cryptographic algorithm before hiding it in the image. The user would be able to choose whether to encrypt the hidden data using a passphrase.

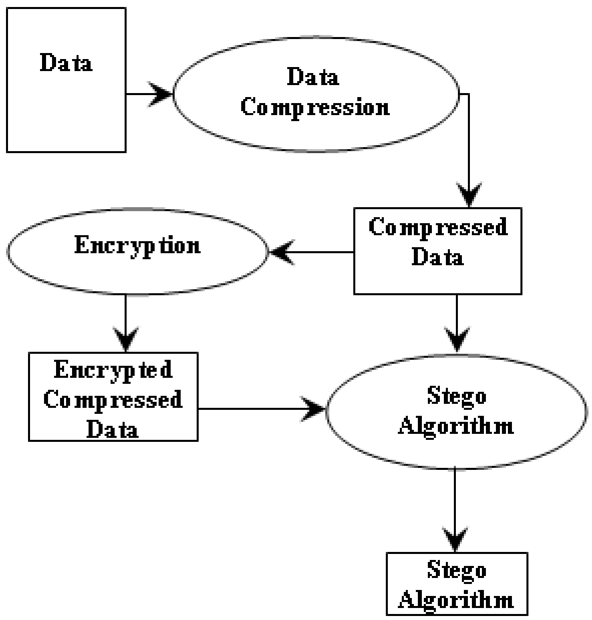

Fig. 4.1 Flowchart for data Encryption

If encryption is used, it would be done after the message to be hidden is compressed using ZIP. The reason being encrypted text is random, and so the encrypted text would not be highly compressible, defeating the purpose of the compression functionality of the system. Another reason is a ZIP file is easily recognizable, as it have identifiable headers and EOF markers. Encryption would turn this into random garbage text which would not be easy to detect.

4.1.1 Hiding Using End of File Method

In this method, the insertion technique after the EOF marker of the image would be employed. This method would be used to hide data in both GIF and JPEG images. For this method, there would be no restriction for the number of bytes that can be hidden.

JPEG images have an EOF marker of two bytes having the hex values FF D9, and GIF images have a value of 00 B3. In order to hide a message, the data that is to be hidden would be written after the EOF markers. A fake appropriate EOF marker for the image would be added at the end of the hidden message to fool any steganalyst. The steganalyst would not suspect the image ending with the usual EOF marker.

Retrieving the hidden data from the image would be done by searching for the fist original EOF marker for that image, the data after that would be copied in a different file until the fake EOF is encountered at the end of the file.

4.1.2 Hiding Using Matrix Embedding Method

Instead of overwriting bits, it decrements the coefficient's absolute values in case their LSB does not match - except coefficients with the value zero, where we can not decrement the absolute value. Hence, we do not use zero coefficients steganographically. The LSB of nonzero coefficients match the secret message after embedding, but we did not overwrite bits, because the Chi-square test can easily detect such changes. So we can hope that no steps will occur in the distribution.

Some embedded bits fall victim to shrinkage. Shrinkage accrues every time when we decrements the absolute value of 1 and $^{-}1$ producing a 0. The receiver cannot distinguish a zero coefficient that is steganographically unused, from a 0 produced by shrinkage. It skips all zero coefficients. Therefore, the sender repeatedly embeds the affected bit since he notices when he produces a zero. If we simply ignore the shrinkage, the superior number of even coefficients disappears. Unfortunately the receiver gets only fragments of the message in this case. The application of an error-correcting code like hamming code could possibly solve the problem.

In many cases, an embedded message does not require the full capacity (if it fits). Therefore, a part of the file remains unused. Figure 4.2 shows that (with continuous embedding) the changes concentrate on the start of the file, and the unused rest resides on the end.

To prevent attacks, the embedding function should use the carrier medium as regular as possible. The embedding density should be the same everywhere.

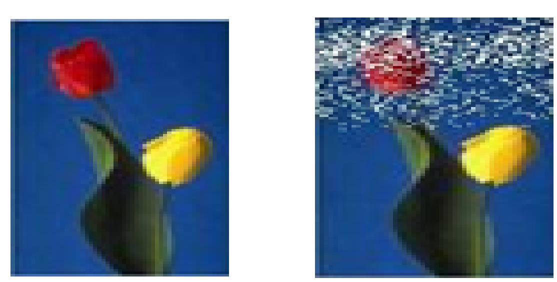

Fig. 4.2 Continues embedding concentrates changes

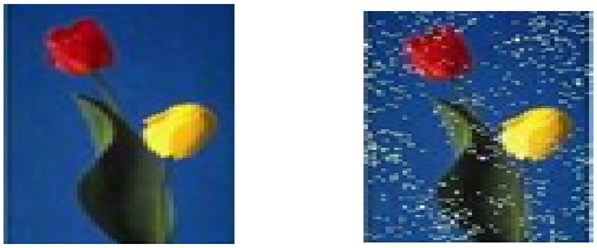

Fig. 4.3 Permutative embedding scatters the changes

4.2 Permutative Straddling

Some well-known steganographic algorithms scatter the message over the whole carrier medium. Many of them have a bad time complexity. They get slower if we try to exhaust the steganographic capacity completely. Straddling is easy, if the capacity of the carrier medium is known exactly. However, we can not predict the shrinkage, because it depends on which bit is embedded in which position. We merely can estimate the expected capacity.

The straddling mechanism used here shuffles all coefficients using a permutation first. Then, we embed into the permuted sequence. The shrinkage does not change the number of coefficients (only their values). The permutation depends on a key derived from a password. This method delivers the steganographically changed coefficients in its original sequence to the Huffman coder. With the correct key, the receiver is able to repeat the permutation. The permutation has linear time complexity O(n). Figure shows the uniformly distributed changes over the whole image.

4.3 Matrix Encoding

Ron Crandall introduced matrix encoding as a new technique to improve the embedding efficiency. If most of the capacity is unused in a steganogram, matrix encoding decreases the necessary number of changes. Let us assume that we have a uniformly distributed secret message and uniformly distributed values at the positions to be changed. One half of the message causes changes, the other half does not. Without matrix encoding, we have an embedding efficiency of 2 bits per change. Because of the shrinkage produced, the embedding efficiency is even a bit lower, e.g. 1.5 bits per change. (Shrinkage means to change without to embed sometimes.)

The following example shows what happened in detail. We want to embed two bits x1, x2 in three modifiable bit places a1, a2, a3 changing one place at most. We may encounter these four cases:

$$\boxed{\begin{array}{l} x_1 = a_1 \oplus a_3,\ x_2 = a_2 \oplus a_3 \Rightarrow \text{change nothing} \\ x_1 \neq a_1 \oplus a_3,\ x_2 = a_2 \oplus a_3 \Rightarrow \text{change } a_1 \\ x_1 = a_1 \oplus a_3,\ x_2 \neq a_2 \oplus a_3 \Rightarrow \text{change } a_2 \\ x_1 \neq a_1 \oplus a_3,\ x_2 \neq a_2 \oplus a_3 \Rightarrow \text{change } a_3. \end{array}}$$

Equation 4.1

In all four cases we do not change more than one bit. In general, we have a code word a with n modifiable bit places for k secret message bits x. Let f be a hash function that extracts k bits from a code word. Matrix encoding enables us to find a suitable modified code word a' for every a and x with x = f(a'), such that the Hamming distance.

$d(a, a') \leq dmax$ ..**Equation 4.2**

We denote this code by an ordered triple (dmax, n, k): a code word with n places will be changed in not more than dmax places to embed k bits.

Bellow Table gives the dependencies between the message bits X_i and the changed bit places a'j. We assign the dependencies with the "binary coding" of j to column a'_j. So we can determine the hash function very fast.

Table 4.1 Dependency (×) between message bits xi and code word bits a'j

$f(a')$	a'_1	a'_2	a'_3
x_1	X		X
x_2		X	X

$f(a')$	a'_1	a'_2	a'_3	a'_4	a'_5	a'_6	a'_7
x_1	X		X		X		X
x_2		X	X			X	X
x_3				X	X	X	X

So in general we find the bit place.

$$\boxed{s = x \oplus f(a)}$$

Equation 4.3 to find the bit place

That we have to change. The changed code word results in

$$a' = \begin{cases} a, & \text{if } s = 0\ (\Leftrightarrow x = f(a)) \\ (a_1, a_2, \ldots, \neg a_s, \ldots, a_n) & \text{otherwise} \end{cases}$$

Equation 4.4

We can find an optimal parameter k for every message to embed and every carrier medium providing sufficient capacity, so that the message just fits into the carrier medium.

5. CONCLUSION

We have explored the limits of steganographic theory and practice. Steganographic techniques can be used to hide data within digital images with little or no visible change in the perceived appearance of the image and can be exploited to export sensitive information. Since images are frequently compressed for storage or transmission, effective steganography must employ coding techniques to counter the errors caused by lossy compression algorithms. The Joint Photographic Expert Group (JPEG) compression algorithm, while producing only a small amount of visual distortion, introduces a relatively large number of errors in the bitmap data. It is shown that despite errors caused by compression, information can be steganographically encoded into pixel data so that it is recoverable after JPEG processing, though not with perfect accuracy.

REFERENCES

[1] P. Wayner, “Disappearing Cryptography, Information Hiding: Steganography and Watermarking (2nd edition)”, Morgan Kaufmann Publishers, 2002.

[2] E. Cole, “Hiding in Plain Sight: Steganography and the Art of Covert Communication”, Wiley Publishing, Inc., 2003.

[3] B. Schneier, “Applied Cryptography (2nd edition)”, John Wiley and Sons, Inc., 1996.

[4] D. Kahn, “The Codebreakers: The Story of Secret Writing”, Macmillan Publishing Co., 1967.

[5] B. Eckel, “Thinking in Java (3rd edition)”, Prentice Hall PTR, 2003.

[6] N. F. Johnson, S. Jajodia, “Steganography: Seeing the Unseen”, February 1998, URL: http://www.jjtc.com/pub/r2026.pdf Accessed Feb 15, 2006.

[7] “NeoByte Solutions: Invisible Secrets”, 4, 2004, URL:http://www.invisiblesecrets.com/

[8] N. Provos and P. Honeyman, “Hide and Seek: An Introduction to Steganography”, May/June 2003, URL:http://www.citi.umich.edu/u/provos/papers/practical.pdf.

[9] Sun Microsystems, Inc., “Code Conventions for the Java Programming Language”, April 1999, URL: http://java.sun.com/docs/codeconv/html/CodeConvTOC.doc.html.

[10] Ron Crandall, “Some Notes on Steganography. Posted on Steganography Mailing List”, 1998. http://os.inf.tu-dresden.de/westfeld/crandall.pdf.

[11] R. James, “Weeks and BioElectroMech”, Visited BioElectroMech at URL http://www.obrador.com.

[12] D.S. Suresh and V. Udaya Shankara, “External Hardware Security for Steganography”, Indian Journal of Computing Technology, Vol.1, No.2, Nov 2006.

Evaluation of Hepatoprotective Potential of Hepative'03

K. Poornima[1], V. Suseela [2] and V. Selvi[3]

[1]Department of Biochemistry, Karpagam University, Coimbatore - 641 021, Tamil Nadu

[2&3]Department of Biochemistry, Kongunadu Arts and Science College, Coimbatore - 641 029, Tamil Nadu

Email: poorniovya@gmail.com

(Received on 05 August 2009 and accepted on 20 June 2010)

Abstract

The study was designed to evaluate the hepatoprotective activity of Hepativ'03 in chronic experimental liver injury induced by alcohol and carbon tetra chloride. In the chronic liver damage induced by alcohol and carbon tetra chloride, Hepativ'03 significantly reduced the elevated serum levels of AST, ALT, ACP, ALP, 5'NT and LDH. In liver, the levels of AST, ALT, ACP, ALP, 5'NT and LDH decreased by alcohol and carbon tetra chloride intoxication and Hepativ'03 significantly increased the level of these enzymes. Histological examination of the liver tissues supported the hepatoprotection. It is concluded that the aqueous extract of the poly herbal formulation Hepativ'03 possesses good hepatoprotective activity.

Keywords: *Alcohol, Carbon tetra chloride,Hepatoprotection, Hepativ'03.*

1. INTRODUCTION

Our country is blessed with vast medicinal plants diversity [1]. Herbal drugs are playing an important role in health care programmes world wide and there is a resurgence of interest in herbal medicines for the treatment of various ailments including hepatopathy. Liver diseases remain one of the serious health problems. Liver injury caused by toxic chemicals and certain drugs has been recognized as a toxicological problem [2]. Alcohol is well known to potentiate the hepatotoxicity of various xenobiotics and the information about interaction between alcohol and the hepatotoxins is well documented [3]. Hence the present study involves the use of a herbal compound formulation Hepativ'03 consisting of various parts of six medicinal plants.

2. MATERIALS AND METHODS

2.1 Selection of Animal

Adult female albino rats of Sprague-Dawley strain weighing between 150-200 gm were obtained from the small Animals Breeding Station, Mannuthy.

2.2 Induction of Necrosis

Necrosis was induced by the oral administration of 40%ethanol (v/v 2.0ml/100gm body weight) for 21 days and a single dose of CCl_4 (1:1 in paraffin oil, ip at a dose of 0.2 ml/kg body weight), which is hepatotoxic to rats [4].

2.3 Preparation of Hepativ'03

Hepativ'03, a herbal formulation consisting of six different plants viz., Hemidesmus indicus Linn root,Juglans regia Linn nut, Vitis vinifera Linn fruit, Hibiscus cannabinus Linn flower, Berberis vulgaris Linn bark and Swertia chirata Ham whole plant was provided for the study by Lok Swasthya Parampura Samvardan Samithi, Ramanathapuram, Coimbatore.

The herbal powder (25%) was decoctioned with boiling water with continuous stirring. The decoction was collected by filtering through cheese cloth and was administered to the rats.

2.4 Experimental Protocol

The rats were divided into four groups of six animals each.

GroupI: Normal control group

GroupII: Toxic control group:- Rats were given 40% ethanol orally for 21 days. On 20th day the animals were injected with CCl_4 (1:1 in paraffin oil,ip at a dose of 0.2 ml/kg body weight)

GroupIII:- Simultaneous treatment group- Along with alcohol and CCl4 simultaneously the animals were treated with 5.0 ml of Hepativ'03 twice a day for 21 days.
GroupIV:- Herbal extract group- Rats were treated with herbal extract alone for 21 days.

2.5 Collection of Rat Liver and Serum

Animals were sacrificed on the 22nd day and the blood was collected and liver was excised immediately and washed with ice cold saline. 10% liver homogenate was prepared with phosphate buffer. The tissue homogenate and serum were assayed for the activities of AST, ALT, ALP, ACP 5'NT and LDH.

2.6 Assay Methods

AST and ALT were assayed by Reitman and Frankel method [5] in tissue homogenate and serum. King and Amstrong [6] method was used to estimate the ALP activity. The ACP activity was determined according to the method of King [7]. The determination of LDH activity was done using DNPH method [8]. 5' NT activity was assayed by Campbell's method[9].

2.7 Statistical Analysis

The results were expressed as mean ± S.D. Differences among means were analyzed by LSD procedure at 95 %($p<0.05$) and 99 %($p<0.01$) confidence level.

3. RESULTS AND DISCUSSION

The activities of serum marker enzymes AST, ALT, ACP, ALP, 5'NT and LDH in control and experimental rats are given in table I. From the table, it is evident that the alcohol and CCl4 intoxication significantly elevated ($p<0.01$) the enzymes namely AST, ALT, ACP, ALP, 5'NT and LDH in group II animals compared to normal control(group I) indicating liver damage. Elevated levels of transaminases are indicative of chronic state of hepatic necrosis [10]. LDH, a cytosolic enzyme is a regulator of many biochemical reactions in the body tissues and the fluids. Disturbance in cell membrane was estimated by measuring the leakage of LDH. [11]. Injury to lysosomal membrane results in leakage of ACP and ALP and hence the raised levels in serum [12].5' NT is a marker enzyme of plasma membrane of liver cells.[13]

On the other hand, the simultaneous treatment (group III) of herbal formulation with the toxicant showed a significant decline in the activity of these enzymes when compared to group II animals. Since the cell membrane defect is a terminal feature in nearly all types of liver cell necrosis, the protective action of herbal formulation might be due to stabilization or strengthening of the cellular membrane.

Table 1 Liver Marker Enzymes in Serum

Activities of Serum AST, ALT, LDH, ALP, ACP AND 5'NT in Control and Experimental Rats

Parameters	Group – I	Group – II	Group – III	Group – IV	F Ratio
	CONTROL	ALCOHOL + CCl_4	(ALCOHOL + CCl_4) + HEPATIV'03	HEPATIV'03	
AST	66.27 ± 1.57	28.95 ± 1.75 ^{a**}	43.78 ± 2.24 ^{b**}	64.51 ± 1.16 ^{c} NS	532.35 **
ALT	27.91 ± 1.49	14.09 ± 1.16 ^{a**}	19.40 ± 1.15 ^{b**}	27.50 ± 1.37 ^{c} NS	131.76 **
LDH	111.72 ± 0.58	76.69 ± 2.88 ^{a**}	93.99 ± 2.15 ^{b**}	112.00 ± 1.01 ^{c} NS	397.16 **
ALP	3.35 ± 0.27	1.66 ± 0.13 ^{a**}	2.42 ± 0.16 ^{b**}	3.39 ± 0.20 ^{c} NS	82.52 **
ACP	8.71± 0.20	4.68 ± 0.34 ^{a**}	6.62 ± 0.19 ^{b**}	8.53 ± 0.17 ^{c} NS	311.06 **
5'NT	6.89 ± 0.25	4.34 ± 0.42 ^{a**}	5.14 ± 0.17 ^{b**}	6.68 ± 0.12 ^{c} NS	104.27 **

Values are expressed as Mean ± S.D (n = 6).

Statistical Comparison

a – Group II is compared with Group I
b – Group III is compared with Group II
c – Group IV is compared with Group I
NS – Non-significant ** $P < 0.01$

Units

AST, ALT, LDH – nmoles of pyruvate liberated / min / mg protein.

ALP, ACP – nmoles of phenol liberated / min / mg protein.
5'NT – nmoles of phosphorus liberated / min / mg protein.

There was no significant difference between (group I) normal control and (group IV) herbal extract group animals. This indicates that herbal extract does not have any deleterious effect on the normal animals. As evident from the above results, the herbal formulation seems to be a better hepato protectant.

The activities of hepatic enzymes namely AST, ALT, ACP, ALP, 5'NT and LDH in control and experimental rats are given in Table 2.

Table 2 Liver Marker Enzymes In Liver

. Activities of Liver AST, ALT, LDH, ALP, ACP And 5'nt in Control and Experimental Rats

Parameters	Group – I	Group – II	Group – III	Group – IV	F Ratio
	CONTROL	ALCOHOL + CCl_4	(ALCOHOL + CCl_4) + HEPATIV'03	HEPATIV'03	
AST	66.27 ± 1.57	28.95 ± 1.75 a **	43.78 ± 2.24 b **	64.51 ± 1.16 c NS	532.35 **
ALT	27.91 ± 1.49	14.09 ± 1.16 a **	19.40 ± 1.15 b **	27.50 ± 1.37 c NS	131.76 **
LDH	111.72 ± 0.58	76.69 ± 2.88 a **	93.99 ± 2.15 b **	112.00 ± 1.01 c NS	397.16 **
ALP	3.35 ± 0.27	1.66 ± 0.13 a **	2.42 ± 0.16 b **	3.39 ± 0.20 c NS	82.52 **
ACP	8.71 ± 0.20	4.68 ± 0.34 a **	6.62 ± 0.19 b **	8.53 ± 0.17 c NS	311.06 **
5'NT	6.89 ± 0.25	4.34 ± 0.42 a **	5.14 ± 0.17 b **	6.68 ± 0.12 c NS	104.27 **

Values are expressed as Mean ± S.D (n = 6).

Statistical Comparison

a – Group II is compared with Group I
b – Group III is compared with Group II
c – Group IV is compared with Group I
NS – Non-significant ** $P < 0.01$

Units

AST, ALT, LDH – nmoles of pyruvate liberated / min / mg protein
ALP, ACP – nmoles of phenol liberated / min / mg protein.
5'NT – nmoles of phosphorus liberated / min / mg protein.

The activities of hepatic enzymes namely AST, ALT, ACP, ALP, 5'NT and LDH were decreased significantly ($p<0.01$) in group II rats induced with chronic oral administration of alcohol and a single dose of CCl_4 as compared to control (group I) rats. This might be due to the leakage of synthesized enzymes into the serum, which in turn might be due to the damage of the cellular compartments of liver necrosis conditions. The serum transaminases and ALP are considered to be sensitive indicators of liver injury[14]. Intoxication with alcohol and CCl_4 has decreased the levels of liver marker enzymes in liver and increased levels in serum. These changes results from the leakage of enzymes from the cells into surrounding media [15]. Significant decrease in hepatic lysosomal enzyme activities are reported at the later stage of the injury when necrosis is well established [16]. 5'NT the plasma membrane marker enzyme is a regulator of many biochemical reactions in the body tissues[17].Simultaneous treatment (group III) group of rats showed a significant increase in AST, ALT, ACP, ALP, 5'NT and LDH activities when compared to group II which might be an indication of recovery from liver damage. This suggests the possible membrane stabilizing property of Hepativ'03 as hepatoprotective agent. When the plant extract alone was administered to normal animals (group IV) they showed no significant effects compared to control (group I).

Histopathology

Histopathological observation of liver sections of rats of all the groups were made. It basically supported the results obtained from the hepatic marker enzyme assays in serum and liver. The results obtained in the histopathological studies were presented in plates I,II,III,IV and V.

PLATE - I Control Group: Structure of Normal Liver of Control Rats. H & E, × 100

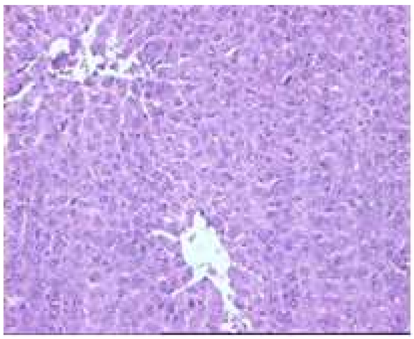

PLATE - II Toxicant Group: Alcoholic Hepatic Steatosis and Mild Necrosis in Alcohol and CCl_4 Treated Liver. H & E, × 100

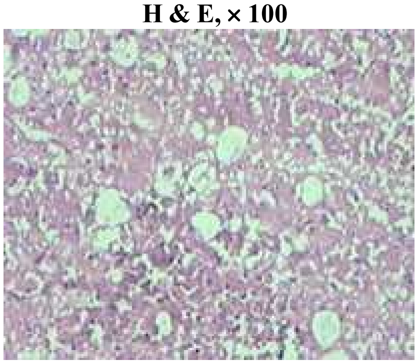

PLATE -III : Toxicant Group: Alcoholic Hepatic Steatosis and Mild Necrosis in Alcohol and CCl4 Treated Liver. H & E, × 450

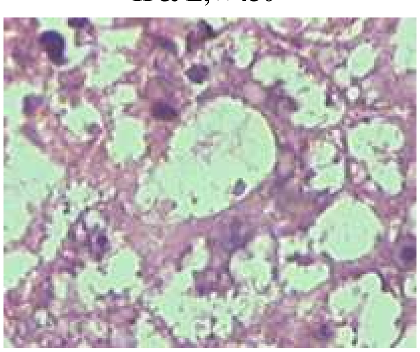

PLATE - IV :Treatment Group: Focal Mild Steatosis and Predominant Normal Hepatocytes in Rat Treated with Alcohol, CCl_4 and Medicinal Plant Extract. H & E, × 100 .

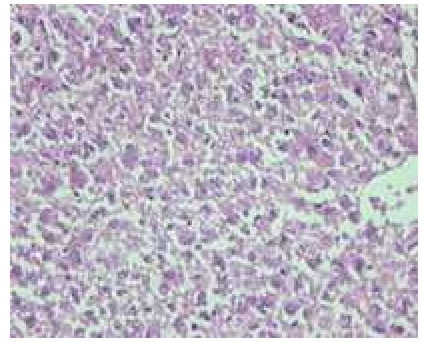

PLATE – V : Herbal Extract Group: Structure of Normal Liver in Rats Treated with Medicinal Plant Extract alone. H & E, × 100.

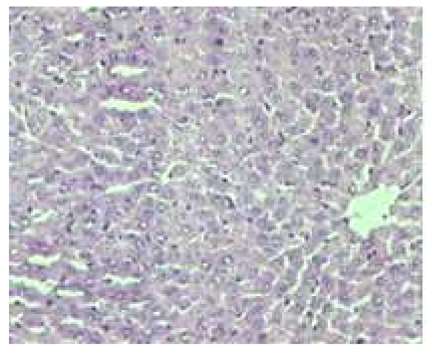

Liver section of normal control rats showed a normal structural and architectural intactness without any apparent damage or disruptions. The animals in group II showed a damage to the hepatic architecture characterized by congested central vein and sinusoids. Most of the hepatocytes showed an evidence of both microvascular and macrovascular steatosis and some appeared necrotic in zone III. The hepatic damage in group III were minimal with distinct preservation of structural and architectural frame, indicating membrane stability as compared to group II animals. The animals in group IV showed normal structure of liver. This confirms that the plant extract has no toxic effect on rats.

4. CONCLUSION

The estimation of hepatic enzymes is the most sensitive test, which is considered as an index for the assessment of liver damage. Treatment with Hepativ’03 has significantly reverted this toxin induced pathological changes indicating the effect of Hepativ’03 in resisting the damage induced by alcohol and CCl4.

Histopathological observations confirms the hepatoprotective role of Hepativ'03 against alcohol and CCl4 induced liver damage. These investigations validate the use of Hepativ'03 as a hepatoprotectant in Indian system of medicine.

REFERENCES

[1] R.P.Saini, "Medicinal Plants of Darjeeling Hills", A Study by Silvi Culture(hills)Division,Dargeeling, Indian Forester, 2000, pp.822-825.

[2] M.R.Venukumar and M.S.Latha, "Hepatoprotective Effect of the Methanolic Extract of Curculigo Orchioides in CCl_4 Treated Male Rats",Indian Journal of Pharmacology, Vol.34, 2002, pp.269-275.

[3] N.Karunakar, K.K.Pillai, S.Z.Hussain,M.Rao, D.K.Balani and M.Imran, "Further Studies on the Antihepatotoxic Activity of Jigrine", Indian Journal of Pharmacology, Vol.29, 1997, pp.222-227.

[4] M.Sharma, K.K.Pillai, S.Z.Hussain, and D.K.Giri, "Protective Role of Propolis Against Alcohol and Carbon Tetra Chloride Induced Hepatotoxicity in Rats", Indian Journal of Pharmacology, Vol.29, 1997, pp.76-81.

[5] S.Reitman and S.Frankel, "Acolorimetr Ic Method for the Determination of Serum Glutamic Oxaloacetic Glutamic Pyruvic Transaminases", Am. J. Clin. Pathol., Vol.28, 1957, pp.56-63.

[6] E.J.King, and A.R.Armstrong, Canad.Med. Ass.J., Vol.31, 1934, pp.376.

[7] J.King, "The Hydrolases–Acid and Alkalinephosphatase", In: Practical Clinical Enzymology(Ed.Van.D.)", London, Norstand Company Limited, 1965a, pp.191.

[8] J.King, "The Dehydrogenase or Oxidoreductase - Lactate Dehydrogenase", In: Practical Clinical Enzymology (Ed.Van, D.),London,Norstand company Limited, 1965b, pp.83.

[9] D.M.Campbell, "Determination of 5' Nucleotidase in Blood Serum", Biochem. J., 1962, pp.34, 84.

[10] L.P.Wolf, "Biochemical Diagnosis of Liver Disease", Indian Journal of Clinical Biochem., Vol.14, No.1, 1999, pp.59-90.

[11] M.G.Viscomi and D.R.Pasqualle, "Hepatoprotective Properties in the Rat of Mitracarpusscaber (Rubiaceae)", Indian Journal of Pharmacology, Vol.51 1999, pp.729-734.

[12] M.P.Germano, R.Sanogo, C.Costa, R.Fulco, D.V.Angelo, E.A.Torrei, H.S.Garg,S.P.S.Bhandari, S.C.Tripathi,G.K.Patnaik, A.Puri, R.Saxena and R.P.Saxena, "Antihepatotoxic and Immunostimulant Properties of Iridoid Glycosides of Scrophularia Koelzii", Phytotherapy Research, Vol.8, 1994, pp.224-228.

[13] R.Rastogi, A.K.Srivastava, M.Srivastava and A.K.Rastogi, "Hepatocurative Effect of Picroliv and Silymarin Against Aflatoxin B1 Induced Hepatotoxicity in Rats", Planta Med., Vol.66, 2000, pp.709-713.

[14] I.Davidson and J.B.Henrey, "ClinicalDiagnosis by Laboratory Methods", Saunders Co., Philadelphia, 1969, pp.690-699.

[15] H.J.Zimmermann and L.B.Seef, "In: Diagnosticenzymology,(Goodly, E.L.,ed.)", Lee and Febiger, Philadelphia, 1970, pp.1-38.

[16] A.K.Saxena, B.Singh and K.K.Anand, "Hepatoprotective Effects of Eclipta Alba on Sub Cellular Levels in Rats", Journal of Ethanopharmacology, Vol.40, 1993, pp.155-161.

[17] Y.Dwivedi, R.Rastogi, N.K.Garg and B.N.Dhawan, "Prevention of Paracetamol Induced Hepatic Damage in Rats by Picroliv", the Standardized Active Fraction from Picrorhiza Kurroa, Phytotherapy Research, Vol. 5, 1991, pp.115-119.

A Development of Technology for Porous Metal Foam

A.K. Shaik dawood[1], S.S. Mohamed Nazirudeen[2] and M. Kavita[3]
[1]Dr.N.G..P. Institute of Technology, Coimbatore - 641 048, Tamil Nadu
[2&3]Department of Metallurgy, P.S.G. College of Technology, Coimbatore - 641 004, Tamil Nadu
E-mail:
(Received on 22 January 2009 and accepted on 18 July 2010)

Abstract

The presence of porosity in the castings is considered as a defect in the material and raises the concern about the quality of the material. But, the porous metals are extremely useful in specific applications because of their peculiar combination of physical and mechanical properties such as high strength to weight ratio with good energy absorption characteristics. They have been of considerable interest both from the industrial applicability and scientific viewpoint. Since the inception of the metal foam, several processes have been developed to introduce large size pores, almost uniformly distributed, in the metallic materials. This paper deals with the special interest in formation of porosity in the cast materials especially in gray cast iron and also illustrates the experimental work done to investigate the possibility of forming porous structures with the inspection methods to confirm the pores formed in and all through the produced castings. The density and percentage porosity of the produced castings were measured and presented.

Keywords: *Density, Metal foams, Percentage porosity, Radiography*

1. INTRODUCTION

Porous metals have raised interest in the last two decades and started to find their way in many research and industrial applications. Nowadays, the manufacturing industry has been challenged to further reduce the size of their products, as consumer demands for lightweight, cost-efficient components with more reliable properties. Typically, such porous metal components are designed with particular properties and for specific applications. Thus, the various research efforts are going on in this area and the production of light weight metals, with excellent physical properties, is possible for a variety of applications. Porous materials are defined as foam materials purposely processed in such a way to contain abundant void space. The voids may range from 30% to 93% open pores and this depends on the method of manufacture and raw materials used.

A pore is the open volume within the metal matrix or network with uniform distribution and length of passages. By manipulation of the process parameters, the pore structure can assume continuous or discontinuous geometries, a range of pore sizes and pore fractions, and a controllable shape of the final product. The continuous pores are connected together and to the surfaces of the component to allow fluid flow from one side to the other.

Porous materials are usually made up of metals or ceramics. Highly porous materials on the base of high melting alloys are of increasing interest because of their structural and functional properties they have properties like high strength, superior energy absorption properties with filtering and acoustic attributes etc. This focuses on the development of a technique to produce porous metals with simple and cost effective method for achieving the porous structure that was previously not possible.

2. LITERATURE REVIEW

From the literature point of view, the first metal foam was invented in 1943, by Benjamin Sosnick of San Francisco California. He created a “sponge metal” using mercury as a foaming agent in molten aluminum. It was not until the 1990’s, however, that an intensified research effort began. This effort was successful in developing new technologies that have brought several metal foams to the marketplace. The list of metals and alloys that have been foamed is extensive. Among the most popular are aluminum, iron, and titanium. There are many ways to produce metallic porous structures. Davies, Banhart and Liu have provided a very comprehensive review on the manufacturing of porous metallic materials. Liu and

Liang 2001; Davies and Zhen 1983; Banhart 2000, 2001; which almost covered all the existing porous metal production methods. The main manufacturing routes involve either gas expansion or the assembly of hollow spheres. In the former, an internal blowing agent is used, which may be dissolved gas or hydrogen evolved from the decomposition of hydrides.

The hollow sphere method has also been applied for making titanium and stainless steel foams. Also by using the step of heating a cast iron having a flake graphite structure for 1 to 5 hours in high temperature gas atmosphere in which the iron component of the cast iron base is not subjected to oxidation and on the other hand the flake graphite is subjected to oxidation, whereby the flake graphite disappears from the cast iron to form pores therein. But in this paper a new technology was developed to produce porous gray iron castings using casting route also samples underwent the compressions tests and were examined conventionally via light microscopy. The casting of metals and alloys around a filler material has recently attracted a lot of interest, because it is potentially a very economic way to create cellular structures of a wide range of metals and porosities. The filler material can either consist of low density materials that remain in the material or it can consist of compact materials that are removed after the casting process, the method practiced here is casting metal around granules as this method produces an interconnected cellular structure metal by casting metal around granules introduced into the casting mould. These granules are soluble and heat-resistant, which is leached out to leave a porous metal. In this process the following three steps are included:

- Preparation of space-holder filler, by using either inorganic or organic granules
- Infiltration of the filler with a metal
- Removal of filler granules

3. EXPERIMENTATION

3.1 Preparation of Sand Balls

Sand balls were prepared manually with the mixture consisting of silica sand and clay as filler materials. Silica sand and clay of measured quantities were taken in a tray and sufficient quantity of water was added to the mixture such that it results in a paste like mixture, made in to round ball of sizes ranging from 5 mm to 30mm. These balls were dried and kept ready for use in molten gray cast iron.

3.2 Melting & Pouring of Gray Cast Iron

A wooden pattern 180mm X 170mm X 65mm was used to produce a mould, using green sand using green sand mould with 5% clay and 3.5% moisture. The sand balls were filled in to the mould cavity. Gray cast iron was melted in an induction furnace with the following proportions as listed in table 1 and inoculated with 0.2% Barium based inoculant added at the ladle was poured into the mould cavity at 1380 C. The poured mould was knocked off, separated from the gating system and shot blasted.

Table 1Proportion of Gray Cast Iron

Element	C	Si	Mn	S	P
Wt %	3.34	2.18	0.56	0.14	0.25

4. TESTING OF POROUS GRAY CAST IRON

4.1 Cut Section Analysis

One of the porous casting was cut into equal halves to examine, visually the distribution of porous structure as shown in figure 1 and to confirm the foam formation and interconnectivity of pores, water jet was used to clean the pores. The molten metal fills the voids in between the cores filled in the die and nucleation starts at the surface of the cores used. So, the shape and size of the pores depends directly on the size and geometry of the cores.

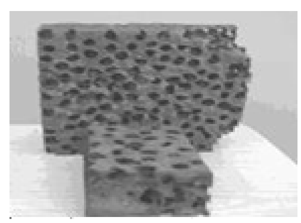

Fig 1. A view of cut section of porous gray cast iron

4.2 Density of the Developed Porous Castings

The foams are characterized in terms of their density since the mechanical properties of metallic foams depend largely on the density. The density of the specimens was determined by weighing the samples using a digital balance and their dimensions were measured. Multiplying the mean value of the measured dimensions, the volume is thus obtained. By dividing the weight of the sample on its volume, density is thus determined.
The density values are given in table 2.

Density = weight of the porous casting / volume of the casting produced sample

4.3 Development of Porosity

Percent Porosity is a rough measure of the open volume equal to 100% minus the part density. The total open volumes of interconnected and isolated porosity are normally included in this value. Here experiment was done with trial 1 as non porous model and with porous models from trial 2 to trail 7 .The strength of the foam depends mostly on the base material and the relative density of the foam, % porosity was calculated and the values from the table 2 give the maximum percentage porosity is got from trial 7 and results of final porosity images are shown in figure 2 to 7

% Porosity = (Bulk casting density – Produced casting density) x 100 / Bulk casting density

Table 2 Showing Sand balls size, Pattern size, Weight, Density and % Porosity

Model	Sand balls Size, mm	Pattern Size(l x b x w)mm	Weight, Kg	Density, 10^{-6} kgfmm^{-3}	% Porosity
Trial 1	Nil	180 X 170 X 65	14.32	7.2	Nil
Trail 2	5	180 X 170 X 65	7.2	3.62	49.79
Trial 3	10	180 X 170 X 65	7.0	3.52	51.11
Trial 4	15	180 X 170 X 65	6.8	3.42	52.50
Trial 5	18	180 X 170 X 65	6.5	3.27	54.51
Trial 6	25	180 X 170 X 65	5.5	2.77	61.52
Trial 7	30	180 X 170 X 65	5.2	2.61	63.75

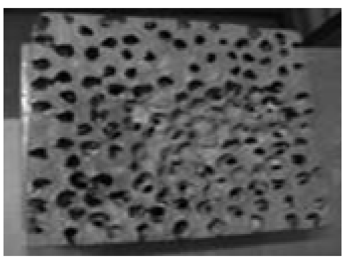

Fig 2. Trial 2 with % porosity of 49.79

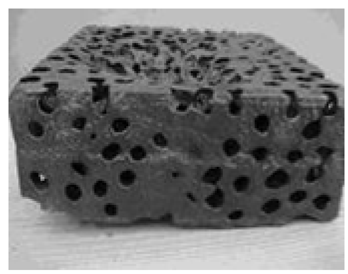

Fig 4. Trial 4 with % porosity of 52.50

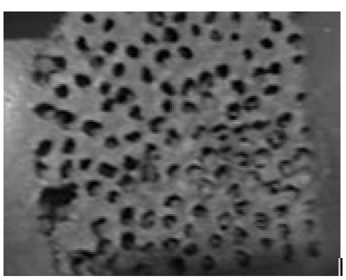

Fig 3. Trial 3 with % porosity of 51.11

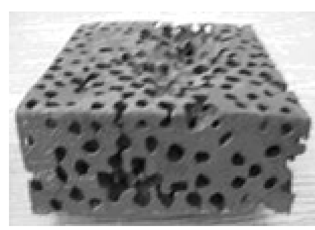

Fig 5. Trial 5 with % porosity of 54.51

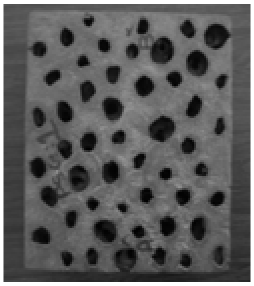

Fig. 6 Trial 6 with % porosity of 61.52

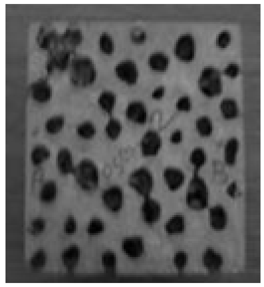

Fig. 7 Trial 7 with % porosity of 63.75

4.4 Radiography Test

The porous gray iron samples were subjected to radiographic inspection for analyzing the pores formed in the metal, the dark region of the film represents the more penetrable part of the object than the light regions which were more opaque.

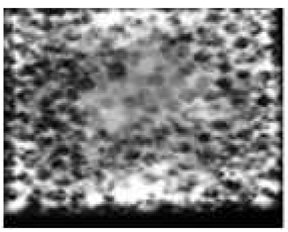

Fig.8 Radiographic image of trial 2

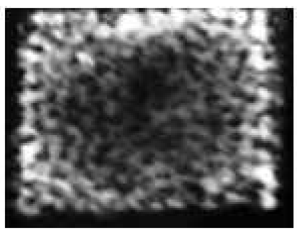

Fig. 9 Radiographic image of trial 3

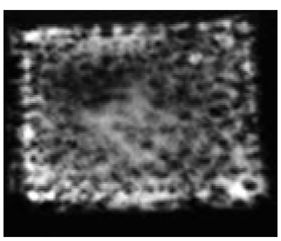

Fig. 10Radiographic image of trial 4

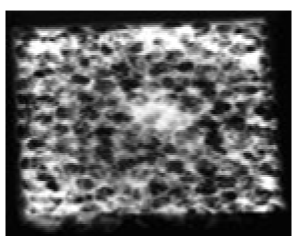

Fig. 11 Radiographic image of trial 5

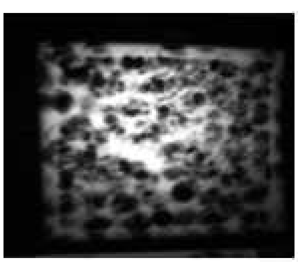

Fig. 12 Radiographic image of trial 6

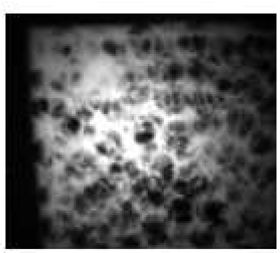

Fig. 13 Radiographic image of trial 7

It was clearly seen that the radiation has passed through the section containing the void than through the surrounding metal. A dark spot, corresponding to the projected position of the void, has appeared on the film. Thus, the final image from radiograph was a kind of shadow picture, where darker regions on the film represented the more penetrable parts of the object, and the lighter regions are more opaque in radiation, as shown in Figure 8 to 13.

4.5 Compression Test

The compression test of metallic foams is considered as one of the most applicable tests for the characterisation of their mechanical stability. It is the method for determining behavior of materials under crushing loads. Porous Sample was compressed, and deformation was recorded. Figure 14 shows the view before compression and Figure 15 shows view after compression. It was seen that during compressive loading of such material are much smoother than those of previously-available melt route material Table 3 shows the compression test, breakable- load capacity for non porous and porous samples.

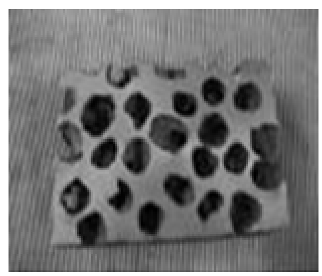

Fig. 14. A view of cut sample before compression

Fig. 15. A view after compression

Table 3 Compression Load on Non Porous & Porous Sample

Trial	Breakable Load, KN	Size(l x b x w) mm
Non-Porous Sample	1400 & above	90x85x50
Porous Sample 1	325	90x85x50
Porous Sample 2	435	90x85x50

5. METALLOGRAPHIC CHARACTERISATION

Micro structural characterisation of samples after high temperature compression was performed using a conventional light optical microscope. The compressed samples were polished using the normal polishing techniques. It is very important during experimental work, the preparation of the samples for the metallographic examination to preserve the foamed structure then the samples containing the pores was sawed carefully to avoid the damage of the cells. Afterwards they were ground and polished using the normal grinding and polishing tools. Microstructure of gray cast iron etched with 2% nitric acid in ethanol (nital) and viewed with (top photo) bright field illumination and with (bottom photo) crossed polarized light, as shown in Figure 16 with 200X nital etched and in Figure 17 & 18 with unetched condition. The study of microstructure reveals type A & D graphite with 60-70% pearlite and rest ferrite.

Fig. 16 Microstructure of polished sample (200X, natal etch)

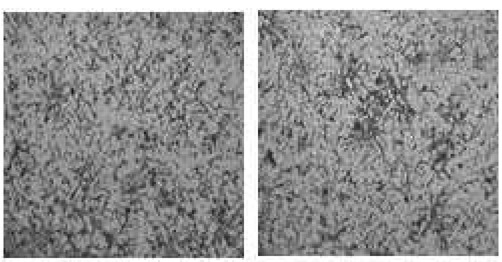

Fig. 17 & 18 Microstructure of polished sample (100X, unetched condition)

6. APPLICATIONS

- It is also well known that the porous cast irons thus obtained are excellently permeable with oil and are useful for machine parts such as bearings.
- Porous cast iron skillet, a Frey pan for faster cooking.
- Porous cast iron silencers muffle the noise while allowing free flow of the escaping gases.
- Porous foams applicable to manufacture porous electrodes which can be used for many electrochemical processes, also those electrodes can also are easily coated with a catalyst.

7. CONCLUSION

To determine the dependence of the mechanical properties on varying porosities the tests are carried out on foams of different densities. Furthermore, a metallographic examination gives an insight into the pore structure and reveals information on pore size, pore distribution and the interconnections of the open cells. It is proved that Porous casting can be developed in gray cast iron, with Percentage porosity 63.75%.

- The density of casting was calculated as 2.61 x10^{-6} kgfmm^{-3} which gave maximum percentage porosity.
- From Radiography test. It is identified that no mass segregation of the metal at any place in the casting.
- From Compression test It is identified that due to porosity, a minimum load of 325 KN was utilized to compress the porous piece whereas maximum load for non-porous model was above 1400 KN

REFERENCES

[1] M. F. Ashby, A.G. Evans, N. A. Fleck, L. J. Gibson, J. W. Hutchingson and H. N.G. Wadley, "Metal Foams, A Design Guide," Butterworth- Heinemann, Woburn, MA, Chapter1, also, 2000, pp. 181-188.

[2] "ASM Metals Handbook", Ninth Edition, Vol.15, Casting, ASM, 1988.

[3] Lu Tianjian , "Ultra Light Porous Metals: From Fundamentals to Applications", (Department of Engineering, University of Cambridge, Trumpington Street, Cambridge CB2 1PZ, UK)

[4] J. Banhart, "Manufacture, Characterization and Application Of Cellular Metals And Metal Foams", Progress in Materials Science, Vol.46, 2001, pp.559-632.

[5] A. E. Scheidegger, "The Physics of Flows through Porous Media, Thirded", University of Toronto Press, Toronto, 1974.

[6] "The Effects of Porosity on Mechanical Properties of Cast Discontinuous",Reinforced... Ahmad *et al.* Journal of Composite Materials, Vol.39, 2005, pp.451-466.

[7] V. Gergely, "Melt Route Processing for Production of Metallic Foams", (Ph.D. thesis, University of Cambridge, 2000), pp.64-77.

[8] Koji Matsumaru, Atsushi Takata and Kozo Ishizaki Nagaoka Gijutsu-Kagaku Daiga, "Porous Cast-iron Bonded Diamond Grinding Wheel", Nagaoka

University of Technology), Nagaoka, Niigata 940-2188, Japan Nano Tem Co., Ltd., 4-11-5 Hasugata Nagaoka, Niigata 940-2023, Japan.

[9] Lennart Elmquist and Attila Diószegi, "Influence of Solidification on the Primary Austenite Structure of Grey Cast Iron" Department of Mechanical Engineering/Component Technology - Castings, Jönköping University, P.O. Box 1026, SE- 551 11 Jönköping, Sweden.

[10] R. Álvarez Hernández Angel, "Combined Flow and Heat Transfer Characterization of Open Cell Aluminum Foams", University of Puerto Rico, Mayagüez Campus, 2005.

Investigation of Thermal Stress Development by Layer Manufacturing of FDM Parts

M. Saravanan[1] and A.S. Vimalakkar[2]

[1&2]Department of Mechanical Engineering, RVS College of Engineering and Technology, Dindigul - 624 005, Tamil Nadu

Email: sarandgl2k@yahoo.co.in, sarandgl2k@gmail.com

(Received on 27 April 2009 and accepted on 22 July 2010)

Abstract

Fused deposition modeling (FDM) developed by stratasys Inc. -USA is the most widely used rapid prototyping technology around the world. The temperature-controlled head extrudes thermoplastic material layer by layer. This process involves successive melting, extrusion and solidification. The nozzle extrudes the material at high temperature but the material is deposited in a chamber maintained at low temperature. This temperature difference results in shrinkage and warpage of the part. This is the major disadvantage of FDM, the most futuristic functional prototyping machine. In this project work, the deflection due to the development of thermal stress along the part was investigated and a suitable numerical model was derived to find out the temperature distribution. The verification is done using finite element analysis model. The above revels that the deflection of the part due to thermal stress can be controlled by selecting the optimum base thickness, road width and the method of removal of the support material from the part.

Keywords: *Ansys, Deflection, Fused deposition modeling, Rapid prototyping*

1. INTRODUCTION TO LAYER MANUFACTURING

1.1 Rapid Prototyping

The rapid prototyping has helped product developers to develop their products more rapidly at lower costs in the ever changing and more competitive global market. It was initially used to make physical prototypes of three-dimensional parts as visualization and communication aids in design as well as for examining the fit of various parts in assembly. It has provided substantial reduction of time-to-market, hence widely called as rapid prototyping in industry. Rapid prototyping is very useful because it produces full size three-dimensional models in a very short time. Having a model of the desired final product helps find problems much earlier in the design process.

1.2 Fused Deposition Modeling

Fused deposition modeling (FDM) is one of the most used rapid prototyping systems. FDM machine creates parts by directly deposition molten material from a delivery head with an associated material supply system. The parts are built on platform in a layer- like fashion. FDM involves the extrusion of ABS plastic just above the melting point using a computer controlled deposition head.

The nozzle is heated t melt the plastic and has a mechanism, which allows the flow of the melted plastic to be controlled. Nozzle deposits a thin bead of extruded plastic to form each layer. The plastic hardens immediately after being squirted from the nozzle and bonds to the layer below. The entire system is contained within an oven chamber, which is held at a temperature just below the melting point.

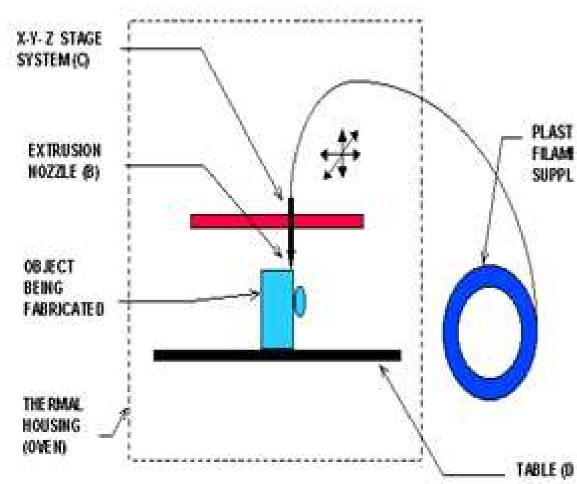

Fig.5 Fused deposition modeling

1.3 Selection of Process

Selection of the optimum process for each case is complex. Among the factors to consider are the final application, production volume, part size, accuracy and material requirements. The descriptions of the available technologies here provide a general guide for selection, as well as places to learn more. Present state of the art is that while direct RP tool generation methods may offer faster turn around, one of the transfer processes may offer lower costs and higher accuracy.

2. PROBLEM DEFINITION

Industries are very eager to use this machine but the end product has certain defects like dimensional accuracy, shrinkage, surface roughness and strength. Therefore, industries are affecting and also hesitate to use these machines.

Aim of this work is to eliminate some problems mentioned above but absolute removal was not possible at present. It can be minimized. The end product has to be used as a functional prototype. The FDM part should be capable enough to use as a pattern for vacuum casting.

The elimination of deflection from the part due to temperature gradient has to be performed. The mechanism used in the fused deposition-modeling machine was the temperature controlled extrusion process. Therefore the process involves different temperatures. This temperature difference in a single part creates the thermal stress along the part. This thermal stress then deflects or shrinks the part.

3. MODULES

The project work consists of three modules. They are:

- Deflection measured from physical part, build in the FDM machine.
- Deflection achieved from Ansys software.
- Deflection calculated from the numerical model.

The purpose of this project was

- To prove the deflection occurred in the FDM parts.
- Increasing the thickness decreasing the deflection. So that the main part can be built after certain thickness of support material to minimize deflection.
- Develop the numerical model to understand the temperature distribution and the stress distribution and the stress distribution along the part.

4. PART BUILDING

The part has to be built to prove the problem as well as solution. The part was built in FDM. The part building consists of both hardware and software. The software used to model was Pro/Engineer 2000i and the parameters entered in the Stratasys Insight Software Version 3. the hardware consists of nozzle cleaning, table cleaning, machine calibration, pressure checking foe both vacuum pump and compressor. The part was build twice.

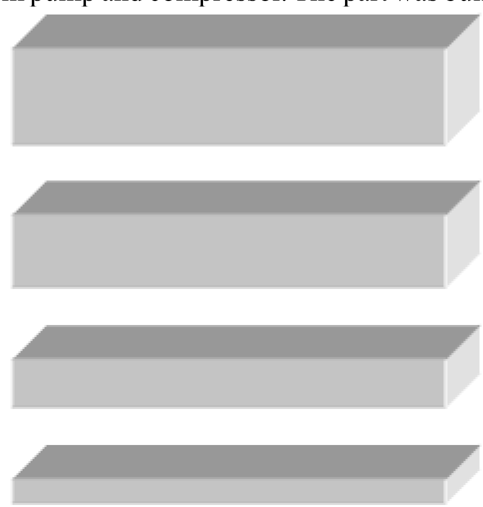

The specification of the above model was as follows:

150*10*10 mm
150*10*7.5 mm
150*10*5 mm
150*10*2.5 mm

First Phase
The default parameters are maintained in the machine for first set. Some of the default parameters as follows:

Layer thickness	=	0.254mm
Road Width	=	0.508mm

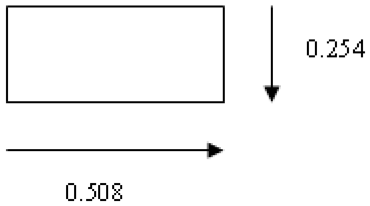

Second Phase

In second phase, the value of the road width was changed to 0.381 mm. This decision was taken after the investigation.

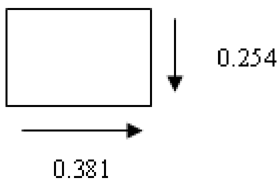

Layer thickness = 0.254mm
Road Width = 0.381mm

The part build from FDM machine had further work to remove the support material. This was done by waterworks.

Water works was a chemical solution to dissolve the support material. The deflection will be less by removing by waterworks, this conclusion was practically seen.

4.1 Measurement of deflection for Build Type I

The physical part was measured using renishaw-scanning machine. The machine was used to take the drawings from the physical part. It was advanced coordinate machine. It has two types of probes to scan the part. They are contact probe and laser probe. The output will be in the form of cloud points. The machine will give clear dimensions and the profile of the deformed object. The physical part taken to the scanning machine in order to measure the radius of curvature. The part was tilted 90 degrees and fixed horizontally. The contact probe scans the profile and it is in the form of dots or cloud points. This cloud points will then converted in to a AutoCAD file then joined as a circle and the radius of curvature value.

The dimensional accuracy and deflection due to thermal stress effects were shown to all the components individually.

Part Dimension	Length	Breadth	Thickness	Deflection
150*10*2.5mm	150.18	9.90	2.58	2.125
150*10*5.0mm	150.20	9.98	5.12	0.923
150*10*7.5mm	150.20	10	7.68	0.420
150*10*10.0mm	150.12	9.96	10.2	0.162

4.2 Parameter Optimization study

The results of build type 1 were investigated carefully and the conclusion made was to optimize the process parameter, which affects the deflection. The process parameters of fused deposition modeling machine were build orientation, layer thickness, road width, air gap and model temperature. The layer thickness and model temperature are fixed. If the orientation of the model changed then the build time, material consumption, accuracy and strength varies. The change of air gap reduces the part weight and accuracy. The only parameter that can be changed with out major disturbance was road width.

The default value of the road width was 0.508mm. The above results were shown for this value. Regarding road width, the minimum value mentioned was 0.381mm.

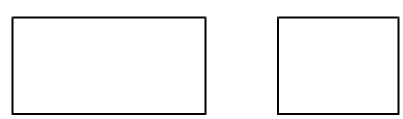

Width = 0.508mm Width = 0.381mm

4.3 Measurement of Deflection for Build Type II

The optimized parameter from the result of optimization study was substituted along with the other process parameters. The parameter chosen was road width. The minimum value was taken as an optimum value. The default value of road width was 0.508mm and the optimum value chosen was 0.381mm.

The dimensional accuracy and the deflection values were shown below.

Part Dimension	Length	Breadth	Thickness	Deflection
150*10*2.5mm	149.81	9.96	2.48	1.92
150*10*5.0mm	149.92	9.98	5.1	0.610
150*10*7.5mm	149.78	10.2	7.53	0.244
150*10*10.0mm	149.93	10	9.89	0.076

5. DEFLECTION ANALYSIS IN ANSYS

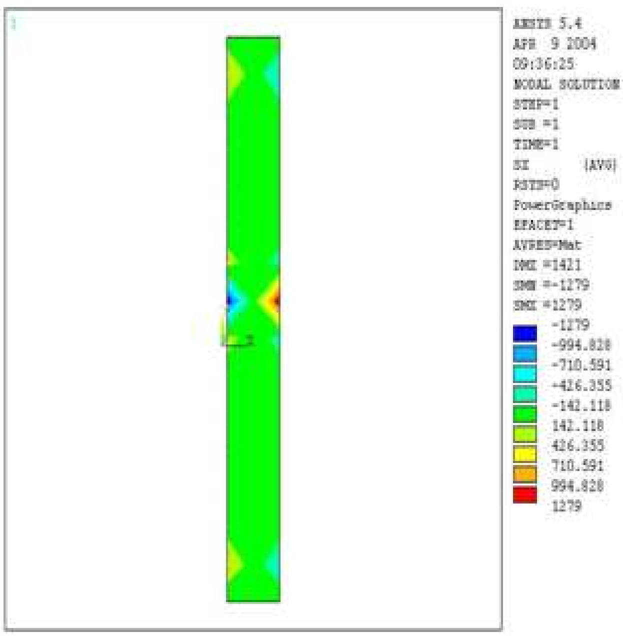

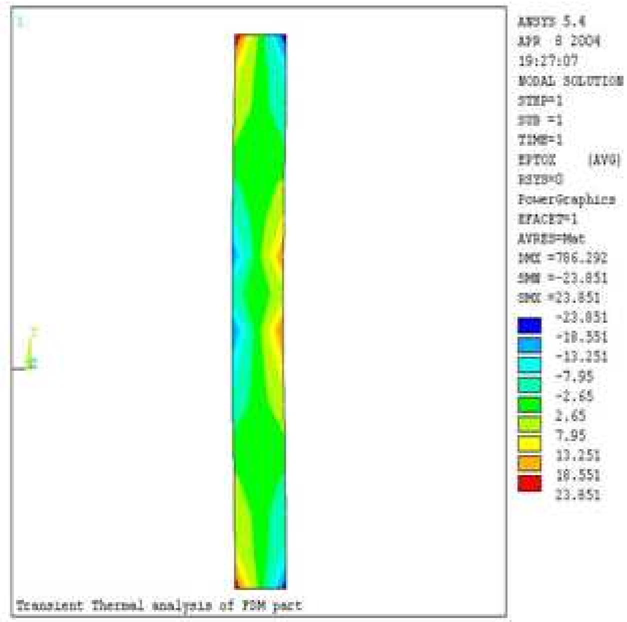

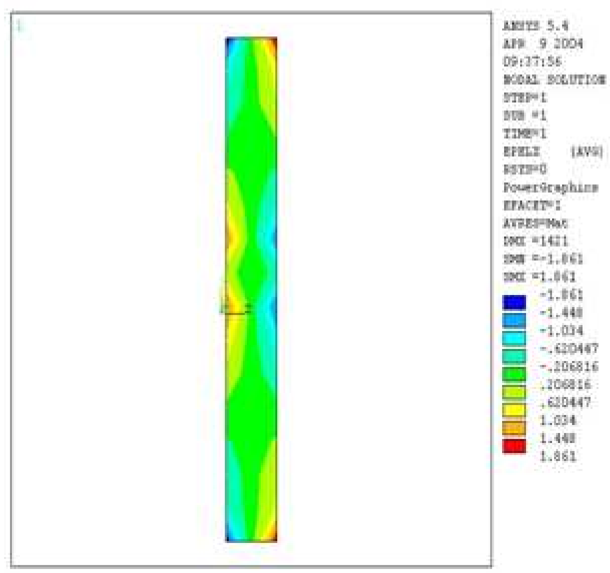

The deflection values obtained in the graph clearly showing that the deflection of default parameter was more than the optimized parameter. The above parts were built as one layer. The values are shown below:

Part Built Condition	Deflection (mm)
With default parameter	0.35
With optimized parameter	0.0409

6. NUMERICAL MODEL

If the body expands or contact freely, the change in length is, $\delta l = \alpha . l \, \Delta T$

Strain induced in the body, $\varepsilon = \delta l / l = \alpha \Delta T$

Thermal stress, $\sigma = E \alpha \Delta T$

6.1 Governing Equation

The temperature in a material is a function of x coordinate and time.

T=T (x, t)

According to the principle of conservation of energy, it can be stated as follows,

Rate of heat conduction in to of control volume + Rate of heat generation inside control volume

Rate of heat conduction out of control volume + Rate of energy storage inside control volume

By Fourier's law,

$$-KA \left.\frac{\partial T}{\partial x}\right]_x + q_G A \Delta X = -kA \left.\frac{\partial T}{\partial x}\right]_{x+\Delta x} + \rho A \Delta X C \frac{\partial T(x + \Delta x / 2, t)}{\partial t}$$

From the above equation, it is derived for tree dimension,

$$\partial^2 T/\partial x^2 + \partial^2 T/\partial y^2 + \partial^2 T/\partial z^2 = 1/\alpha \; \partial T/\partial \tau$$

Where $\alpha = K/\rho C$

The Finite Difference Method of the above equation for two dimensions is derived as follows

$$\frac{T^n_{i+1,j} - 2T^n_{ij} + T^n_{i-1,j}}{\Delta x^2} + \frac{T^n_{i+1j} - 2T^n_{i,j} + T^n_{i-1j}}{\Delta y^2} = \frac{1}{\alpha} \; \frac{T^{n+1}_{i,j} + T^n_{i,j}}{\Delta t}$$

The above equation was derived for different conditions by assuming $\Delta x = \Delta y$

Known Values

$\Delta x = \Delta y = 0.25$

Convective heat transfer coefficient [h] =10 W/m K

Thermal Conductivity [k] =0.27 W/m K

Thermal Diffusivity [α] = 1.7* 10_7m2/s

Ambient Temperature [$T\infty$] = 80 degree Celsius

Initial Temperature [T] =280 degree Celsius

Coefficient of Thermal expansion = $9.5 * 10^{-5}$/k

Fourier Number [Fo] = $\dfrac{\alpha \Delta T}{\Delta x^2}$

Biot Number [Bi] = $\dfrac{h \Delta x}{K}$

We can get temperature for all node points,

X =

T1 = 279.0006
T2 = 279.6989
T3 = 279.9079
T4 = 279.7664
T5 = 280.1242
T6 = 280.0559
T7 = 280.0084
T8 = 279.9825

Radius of curvature (R) = $\dfrac{EY}{\sigma}$

$$\frac{L}{2\Pi R} = \frac{\theta}{360}$$

Angle (θ) = $\dfrac{360 * L}{2 \, \Pi \, R}$

$a = R \sin(\theta/2)$

$\delta = a \tan(\theta/2)$

By using the above equations and the results arrived were,

There are two layers in the model. The deflection was calculated for both the layers individually. The deflection obtained was as follows:

Deflection	Values (mm)
Layer 1	3.42
Layer 2	0.942

From the above values, it was clearly visible that the deflection of layer 2 was less than the deflection of layer 1.

7. CONCLUSION

Fused deposition modeling was one of the successful and most widely used prototype manufacturing machine. The prototypes made from this machine used for the visualization purpose before, but now the market trend were changed people were expecting more accuracy, finish and it should be capable of testing. The material used in this machine was ABS plastic so mostly functional testing was limited. However, it can be used as the pattern or die in casings. The machine accuracy given by the manufacturer was 127 microns, but the problem here is shrinkage due to the temperature gradient effects. The results from the project work shows that the deflection was approximately 900 microns. The main aim of the work is to study the temperature distribution and to minimize the deflection.

The conclusion made from this work was as follows:

- Minimum Road width should be used.
- The part should be built upon certain height i.e. Base thickness should be raised to a certain level where the deflection is minimum.
- From the deposition style, it should not deposit long layers instead of that, raster type should be followed.
- Removal of support material should be undertaken through the waterworks. The FDM support material was produced in such a manner it will dissolve in the chemical solution.
- The part should undergo a slow cooling process before taking the components out of the chamber, which was maintained at 80 degree Celsius.

The above conclusion was made after analyzing the results through the analyzing software 'Ansys' and through numerical model.

REFERENCES

[1] A.H.Nickel, D.M. Barnett, F.B.Printz, "Thermal Stresses and Deposition Patterns in Layer Manufacturing", Materials Science and Engineering-March 1999.

[2] Raymond Ong, Jack L. Beuth, Lee Weiss, "Residual Stress Control Issues for Thermal Deposition of Polymers in SFF Processes" Carnegie Mellon University-Pittsburgh.

[3] Sung-Hoon Ahn, Michael Montero, Dan Odell, Shad Roundy and Paul K. Wright, "Anisotropic Material Properties of Fused Deposition Modeling ABS " USA.

[4] Michael Montero1, Shad Roundy1, Dan Odell1, Sung-Hoon Ahn2and Paul K. Wright, "Material Characterization of Fused Deposition Modeling (FDM) ABS Designed Experiments", Korea Institute of Technology.

[5] J.P.Holman, "Heat Transfer" McGraw Hill Inc., Eighth Edition, 1997.

[6] John D.Anderson, JR, "Computational Fluid Dynamics" McGraw Hill Inc., 1995.

Indian Journal of Engineering, Science, and Technology (IJEST)

(ISSN: 0973-6255)

(A half-yearly refereed research journal)

Information for Authors

1. All papers should be addressed to The Editor-in-Chief, Indian Journal of Engineering, Science, and Technology (IJEST), Bannari Amman Institute of Technology, Sathyamangalam - 638 401, Erode District, Tamil Nadu, India.
2. Two copies of manuscript along with soft copy are to be sent.
3. A CD-ROM containing the text, figures and tables should separately be sent along with the hard copies.
4. Submission of a manuscript implies that : (i) The work described has not been published before; (ii) It is not under consideration for publication elsewhere.
5. Manuscript will be reviewed by experts in the corresponding research area, and their recommendations will be communicated to the authors.

Guidelines for submission

Manuscript Formats

The manuscript should be about 8 pages in length, typed in double space with Times New Roman font, size 12, Double column on A4 size paper with one inch margin on all sides and should include 75-200 words abstract, 5-10 relevant key words, and a short (50-100 words) biography statement. The pages should be consecutively numbered, starting with the title page and through the text, references, tables, figure and legends. The title should be brief, specific and amenable to indexing. The article should include an abstract, introduction, body of paper containing headings, sub-headings, illustrations and conclusions.

References

A numbered list of references must be provided at the end of the paper. The list should be arranged in the order of citation in text, not in alphabetical order. List only one reference per reference number. Each reference number should be enclosed by square brackets.

In text, citations of references may be given simply as "[1]". Similarly, it is not necessary to mention the authors of a reference unless the mention is relevant to the text.

Example

[1] M.Demic, "Optimization of Characteristics of the Elasto-Damping Elements of Cars from the Aspect of Comfort and Handling", International Journal of Vehicle Design, Vol.13, No.1, 1992, pp. 29-46.

[2] S.A.Austin, "The Vibration Damping Effect of an Electro-Rheological Fluid", ASME Journal of Vibration and Acoustics, Vol.115, No.1, 1993, pp. 136-140.

SUBSCRIPTION

The annual subscription for IJEST is Rs.600/- which includes postal charges. To subscribe for IJEST a Demand Draft may be sent in favour of IJEST, payable at Sathyamangalam and addressed to IJEST. Subscription order form can be downloaded from the following link http:// www.bitsathy.ac.in./ ijest.html.

For subscription / further details please contact:

IJEST

Bannari Amman Institute of Technology

Sathyamangalam - 638 401, Erode District, Tamil Nadu Ph: 04295 - 221289

Fax: 04295 - 223775 E-mail: ijest@bitsathy.ac.in Web:www.bitsathy.ac.in/ijest.html

Indian Journal of Engineering, Science, and Technology

Volume 4, Number 2, July - December 2010

CONTENTS

Published by

BANNARI AMMAN INSTITUTE OF TECHNOLOGY

BANNARI AMMAN INSTITUTE OF TECHNOLOGY
Stay Ahead

(Autonomous Institution Affiliated to Anna University of Technology, Coimbatore - Approved by AICTE - Accredited by NBA and NAAC with "A" Grade)

Sathyamangalam - 638 401 Erode District Tamil Nadu India

Ph: 04295-221289 Fax: 04295-223775

TUV NORD ISO 9001